Iann Cunha

Platforms based on semiconductors for application in quantum computing

Brazil

2023

Iann Cunha

Platforms based on semiconductors for application in quantum computing

Thesis presented to the Pos-Graduate Program of the Department of Physics at the Federal University of São Carlos, as a partial requirement for obtaining the title of Doctor of Physics.

Federal University of São Carlos – UFSCar

Physics Department

Post-Graduate Program

Supervisor: Prof. Dr. Leonardo Kleber Castelano

Brazil

2023

Acknowledgements

I would like to express my heartfelt gratitude to my supervisor, Leonardo Castelano, for his exceptional patience in guiding me through various aspects of this project and providing invaluable support in its development and documentation.

To my friends Jeremias and Santiago, whose presence and shared passion for the field of science have allowed for numerous enlightening discussions. These exchanges have greatly enriched my understanding of physics, even in the face of my limited knowledge.

To my housemates Cassius, Felipe, Luis, Matheus, and Vitinho. Sharing a home together for the past couple of years has created a unique bond and unforgettable memories.

To distant friends Arthur and Luiza. Although they have embarked on a new chapter of their lives in Germany, our friendship has remained steadfast and their history inspiring.

To my graduation friends Emilene, Guiga, Hindi, Léo, PH, Sofia whose unwavering support and encouragement have played a pivotal role in my academic journey.

To one of my youngest friends Gustavo. Throughout our journey together, I had the privilege of assisting him with physics and math classes, while also sharing the joy of playing Magic.

To Ciça and Raphael. What initially began as a friend of a friend has blossomed into a treasured bond and now we enjoy sharing moments of relaxation and camaraderie over a few beers.

To my friend Bruno. Our friendship predates my university years, and it has been a constant source of support and companionship throughout my life.

To my childhood friends, Guga and Tulio. Our friendship has spanned from the early days of our youth to the present, witnessing the transformation of our lives into adulthood and the joys. Thank you both for being incredible friends and role models, as

we navigate the beautiful journey of life.

I would also like to express my deep appreciation to the dear and hospitable Carol, Henrik, and Thea, who have provided me with warmth and support throughout this endeavor.

I am indebted to CAPES for their financial support, which has made it possible for me to pursue this work.

Lastly, I would like to acknowledge my family, who may not fully grasp the intricacies of exact sciences but have shown unwavering dedication in supporting my studies. Their unwavering presence in my life is cherished and always resides in my heart.

Abstract

This thesis is composed of three parts. In the first part, a study of transport in semiconductor nanowires is carried out, in which the multichannel scattering occurs in a certain finite region, providing a reentrance in the conductance. This reentrance is analyzed in zero magnetic field configuration for cases where there is a strong spin-orbit coupling and for a structural deformation in the nanowire, where it suffers a localized expansion. Furthermore, both cases are also investigated in the presence of a magnetic field, where the reentrance also appears in higher energy channels. In the second part of this thesis, machine learning is applied to successfully determine physical parameters of two qubits in coupled semiconductor quantum dots, with the aim of locally measuring the qubits and reducing the necessary measurements performed in the laboratory. In the third part of the thesis, the study focuses on the interaction of distant qubits formed by quantum dots. These qubits are modeled by a spin chain with nearest neighbor interactions and the goal is to implement SWAP and CNOT quantum logic gates in this spin network. Finally, by using SWAP gates, it is possible to propagate quantum information along the spin chain. When noise effects are taken into account, there is a relevant difference in the order of application of the logic gates, which leads to an increase or decrease in the effectiveness of the application of quantum gates.

Resumo

Esta tese é composta de três partes. Na primeira parte, é realizado um estudo de transporte em nanofios semicondutores, no qual o espalhamento multicanal ocorre em uma determinada região finita, proporcionando uma reentrância na condutância. Essa reentrância é analisada em configuração de campo magnético nulo para casos onde há um forte acoplamento spin-órbita e para uma deformação estrutural no nanofio, onde ele sofre uma expansão localizada. Além disso, ambos os casos também são investigados na presença de um campo magnético, agora apresentando reentrâncias em canais de maior energia. Na segunda parte desta tese, o aprendizado de máquina é aplicado para determinar com sucesso parâmetros físicos de dois qubits em pontos quânticos semicondutores acoplados, com o objetivo de medir localmente os qubits e reduzir as medições necessárias realizadas em laboratório. Na terceira parte da tese, o estudo foca na interação de qubits distantes formados por pontos quânticos. Esses qubits são modelados por uma cadeia de spin com interações de vizinhos mais próximos e o objetivo é implementar portas lógicas quânticas SWAP e CNOT nessa rede de spin. Finalmente, usando portas SWAP, é possível propagar a informação quântica ao longo da cadeia de spin. Quando os efeitos do ruído são levados em consideração, há uma diferença relevante na ordem de aplicação das portas lógicas, o que leva ao aumento ou diminuição da efetividade da aplicação das portas quânticas.

List of Figures

Contents

1 Introduction

1.1 Quantum computation

The concept of quantum computing began to be developed and studied in the early 1970s by works such as of Alexander Holevo (2) in quantum information and of R.P. Poplavskiĭ (3) showing the computational inefficiency of simulating quantum systems on classical computers. Later, in early 1980s, it was consolidated by the physicist Richard Feynman (4), who proposed that quantum computers could be used to simulate quantum systems that are difficult to model with classical computers. The first practical demonstrations of quantum algorithms were conducted by researchers such as Peter Shor and Lov Grover (5, 6) in the 1990s.

Today, there are many companies and research institutions working on building practical quantum computers, including Google, IBM, Xanadu, and Microsoft. These efforts have led to significant milestones in quantum computation, such as Jiuzhang computer from University of Science and Technology of China with the demonstration of quantum supremacy in 2021 (7), which illustrated how a quantum computer could solve a problem faster than the world's most powerful classical supercomputer. Despite these advances, quantum computing is still in the early stages of development, and there are many technical challenges that need to be addressed to advance further.

Briefly speaking, quantum computation is a type of computation that uses quantum mechanical phenomena, such as superposition and entanglement, to perform operations on quantum bits (qubits) instead of classical bits. It is different from classical computation because it exploits the principles of quantum mechanics to perform certain calculations faster and more efficiently than classical computers. In quantum computation, qubits can exist in a superposition of states, meaning they can represent multiple states simultaneously. For example, a qubit can represent both a bit 0 and a bit 1 at the same time, whereas a classical bit can only represent one of those bits at a time. This allows for the processing of

much larger amounts of information in parallel, resulting in faster computation for certain types of problems. These qubits can be constructed in several ways, such as topological qubits (8), superconducting qubits (9, 10), trapped atoms (11), photons (12), and quantum dots (13).

1.2 Semiconductor based platforms

Semiconductor-based platforms offer a promising avenue towards building scalable quantum computers (14, 15, 16, 17). One approach is through the use of topological insulators (18), which are materials with a unique electronic structure where conducting states are topologically protected against backscattering (19, 20, 21). The topological nature of these states makes them robust to perturbations, which is crucial for quantum information processing. Quantum dots, which are small islands of semiconducting materials that can trap a small number of electrons, provide another route towards quantum computing. Quantum dots allow for precise control of the quantum states of electrons, making them a promising platform for qubits (22). By exploiting the quantum properties of these platforms, researchers aim at developing robust and scalable quantum computing technologies for a wide range of applications, such as cryptography, optimization problems, and simulation of quantum systems.

Topological insulators are a class of materials that have been of significant interest in the field of condensed matter physics due to their potential applications in electronic and spintronic devices, in particular semiconductor nanowires (NWs) (23, 24). These are one-dimensional structures that have a diameter of only a few nanometers and a length of several micrometers. They have unique electronic properties due to their small size, which can lead to quantum confinement effects. This confinement can cause the energy levels of electrons to be quantized, resulting in a discrete set of energy levels (25). In addition, semiconductor NWs can be grown with a variety of material systems, including III-V compounds (26), silicon, and germanium (27), making them a versatile platform for the development of electronic and quantum devices.

One of the key properties of topological insulators is their ability to exhibit a bulk band gap while having a gapless surface state (28). The surface states of topological insulators are protected by time-reversal symmetry (19, 20), which means that they cannot be destroyed by small perturbations. This property makes them particularly useful for quantum computing, as the surface states can be used to create qubits that are protected from environmental noise.

In semiconductor NWs, the surface states of topological insulators can be engineered by the application of an external magnetic field. When a magnetic field is applied perpendicular to the axis of the nanowire, the surface states of the topological insulator are split into two energy levels that are separated by the Zeeman energy (25). The Zeeman energy is proportional to the strength of the magnetic field and the magnetic moment of the electron. This splitting of the surface states can be used to create a qubit with two states, which can be manipulated using microwave pulses. However, these types of qubits are still susceptible to environmental noise and decoherence, which can limit their usefulness in practical quantum computing applications. To address this problem, researchers have turned to Majorana fermions (29).

A Majorana fermion is a special type of quasiparticle proposed in 1937 by Ettore Majorana, which is a particle that is its own antiparticle (30). In condensed matter systems, these Majorana fermions can also manifest as Majorana bound states (MBSs)(31). These MBSs emerge at point-like defects in a class of superconducting systems called topological superconductors (28, 32, 33). They possess intriguing properties: are their own antiparticles (34), have zero spin and zero charge, and exist at exactly zero energy with a gap separating them from other quasiparticle excitations, Consequently, they are referred to as Majorana zero modes. Most notably, MBSs in a 2D material are a type of non-Abelian anyons (35, 36), meaning that exchanging two MBSs results within a degenerate subspace. Formally, this is equivalent to multiplying a vector constructed out of such degenerate ground states by a matrix. Since matrix multiplication is generally noncommutative, the order in which such anyons are exchanged now matter (37). These properties make MBSs promising candidates for topological quantum computers, with

logical gates implemented through anyon exchange.

MBSs were predicted to occur in superconductors with rare spin-triplet pairing symmetry (38, 39, 36). However, it was later realized that an effective spin-triplet pairing can be engineered by combining a conventional spin-singlet s-wave superconductor with a material exhibiting helical bands (40, 41). These so called helical bands refer to unique property in the electronic bands: the electron's spin is intrinsically coupled to its momentum. Specifically, the spin direction of an electron becomes locked or correlated with its momentum direction. Moreover, the collective behavior of electrons within helical bands defines the helical states. And when a material exhibits helical states, it means that there are regions or regimes in the material where electrons propagate in a counterpropagating manner along a specific direction. With this discovery MBSs now appears within experimental reach and have been proposed to emerge in various systems (40, 42, 43, 44, 45). One promising approach to realizing topologically quantum computation is by employing MBSs in NWs with strong spin-orbit coupling (SOC) (46, 47, 48). Semiconductor NWs based on InAs and InSb have a strong SOC and the experimental realization and characterization of such NWs have been recently explored to check the existence of helical states (1, 49, 50, 51). The characterization of helical states can be performed by checking the existence of the re-entrant behavior, which appears as a dip in the conductance probed in NWs with strong SOC and under a perpendicular magnetic field.

Quantum dots (DQs), on the other hand, are nanoscale structures made of semiconducting materials that can trap a small number of electrons in a confined space, forming an artificial atom (52). The confined electrons in QDs exhibit quantum behavior, which makes them a promising platform for quantum computing (53, 13).

In a quantum dot-based qubit, the two states of the qubit are associated with the spin of a single electron confined within the quantum dot. The spin of the electron can be manipulated by applying a magnetic field, which can be used to perform quantum operations. One of the key advantages of QDs is their scalability. They can be fabricated in large arrays using standard semiconductor fabrication techniques (54), allowing for the construction of large-scale quantum devices. In addition, they can be integrated with

classical electronics, which enables the readout and control of the qubits.

One of the main challenges of QDs is achieving high-fidelity control of the qubits. In particular, there are several sources of decoherence that can degrade the performance of the qubits, such as fluctuations in the magnetic field, phonon-mediated interactions, and charge noise. To mitigate these effects, researchers are developing various techniques such as dynamical decoupling (55, 56), error correction codes (57), and spin echo techniques (58, 59).

Another challenge is the limited range of interactions between the qubits in a quantum dot array. The interactions between the qubits are mediated by the exchange of electrons, which can be limited by the size of the quantum dot and the distance between them. To overcome this challenge, researchers are exploring the use of long-range interactions, such as dipole-dipole interactions (60, 61) or photon-mediated interactions (62).

Despite these challenges, QDs offer a promising platform for quantum computing. They have already been employed to demonstrate the ability to perform basic quantum operations, such as single-qubit gates and two-qubit gates, and hold promise for the development of large-scale quantum devices. In addition to quantum computing, QDs are being explored for other applications such as quantum sensing (63), quantum metrology (64), and quantum cryptography (65).

1.3 Structure of the thesis

Recently in 2017 Heedt et al., experimentally study the transport properties of semiconductor NWs with strong SOC, focusing on the behavior of electron interactions in quantum point contacts (Figure 1a). They treated a NW covered by a dielectric layer, controlling the number of channels based on an applied voltage, in the presence of an electric field with a magnetic field variation. The authors observe an unusual conductance feature that they attribute to the emergence of a helical gap (Figure 1b). Unlike previous theoretical predictions, the authors confirm the presence of helical states through measurements of

the re-entrance behavior in the conductance in the absence of an external magnetic field.

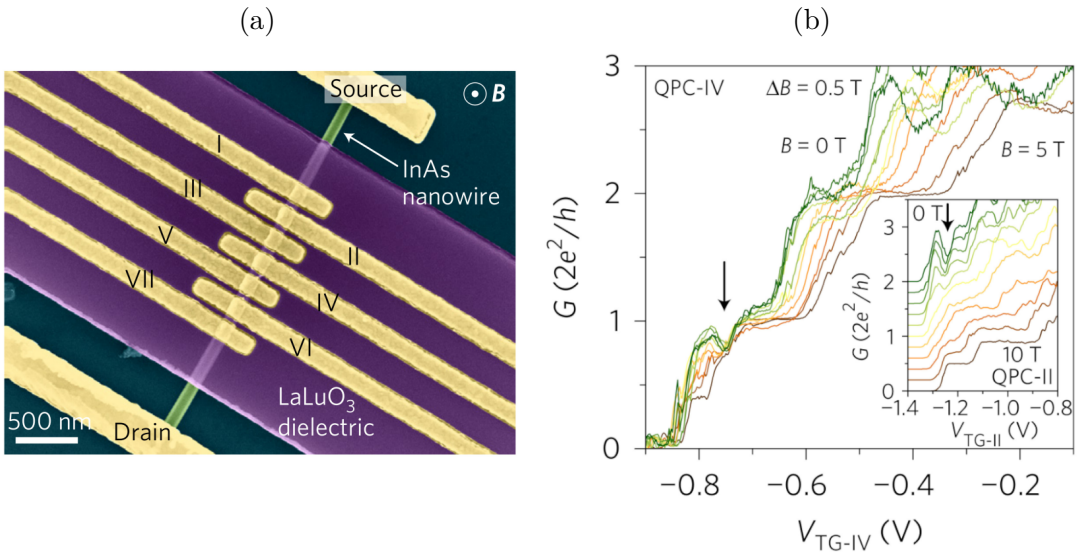

Figure 1 – Conductance and pseudogap feature from reference (1). (a) Top-view image of the InAs nanowire covered with a layer of a dielectric. Numbered from I to VII are the top-gate electrodes used to deplete the channel and control the number of 1D subbands. (b) Re-entrant conductance behavior on the first plateau, with the re-entrant conduction feature location indicated by the black arrows.

In chapter 2, we theoretically demonstrate that the observation of the conductance dip can be explained through a multi-channel scattering mechanism, which causes a reduction of the transmission when an effective attractive potential and coupling between different channels are present. Both ingredients are provided by the SOC in the transport properties of NWs. The relative effect of the sharpness of interfaces and external fields has also been assessed. The reduction of symmetry constraints of the NW is analyzed and proven to be important in the tuning of re-entrant characteristic. Furthermore, we investigate the effects of deformations in the electronic transport in NWs considering the coupling between different transverse modes. Within this approach, it is shown that the dip in the conductance of an NW is affected by the presence of a local constriction. Moreover, we show that the reentrant feature in the conductance can appear in NWs with a local expansion of its radius, even in the absence of SOC and magnetic field.

In quantum mechanics, we can only have access to information about the quantum system through the so-called observables, which are mathematically described by

Hermitian matrices or operators. In an experiment, we can only observe the eigenvalues of these observables. Moreover, the outcomes of each possible measurement on a system are described by the state vector, which provides a probabilistic distribution for these eigenvalues. Observables, such as the density matrix of the system, are obtained through several experimental measurements and by using the state tomography (66). However, this task is often time-consuming due to the required large number of measurements and manipulations. In the chapter 3, we construct a protocol using machine learning tools to determine physical parameters of interest. Particularly, we focus on the determination of parameters of the Hamiltonian describing a double quantum dot system. By training a neural network to predict the parameters of the Hamiltonian using theoretical values calculated from measurements of observables at different time values, we study models that can be used to predict the interqubit coupling.

In the chapter 4, our study focuses on the problem of noise effects that can degrade the performance of interacting distant quantum dot qubits. In this study, we model QDs spin qubits as a spin chain with nearest-neighbor interaction. Using this model, we can perform the interaction of distant qubits by the action of consecutive SWAP gates. The SWAP gate exchanges the information of two different qubits and it is obtained by a time-dependent interaction of nearest-neighbor qubits that is switched on and off as the quantum information propagates through the system. By using this scheme, we can also implement the CNOT gate, which is a fundamental gate to obtain universal quantum computation. These gates are demonstrated in a system that is free from decoherence, allowing for a very efficient connection between distant qubits. Lastly, we analyze the effects of dissipation on the system. We consider dephasing and amplitude-damping errors in each site of the spin chain and found that the application order of the SWAP and CNOT gates is important and depends on the type of error present.

2 Transport in semiconductor nanowires

2.1 Introduction

As already mentioned in the Introduction of this thesis, a signature to verify helical states is the so-called reentrant behavior (67), which appears as a measurable dip in the conductance when an external magnetic field is different from zero. In Ref. (1), however, an unexpected result was observed: the appearance of the reentrant characteristic in the absence of the external magnetic field. This feature was attributed to spin-flipping two-particle backscattering (1, 68, 69). Nonetheless, the dip at zero magnetic field may also appear in the presence of scattering by impurities (70, 71). Consequently, a clear explanation for the reentrant feature is still lacking, as stated in Ref. (51), and we also subscribe to that assertion.

In this chapter, we want to shed light on the problem of the observation of the reentrant behavior when the magnetic field is absent by adding an essential ingredient that has clearly been previously overlooked. In our approach we reinterpret the dip in the conductance as a resonant reflection and use the Rashba Hamiltoninan for the SOC. To comprehend this effect, one needs to understand that the Rashba Hamiltonian limited to a finite region behaves as an attractive potential, as shown in Ref. (72). Furthermore, it has been demonstrated that a resonant reflection (dip in the conductance) might occur if two conditions are satisfied: the scattering by an attractive potential and the coupling between different transport channels (73), even in the absence of a magnetic field. Precisely, these two ingredients are present in quasi-one-dimensional systems, such as NWs, where the SOC takes place in a finite region.

Furthermore, we show that these fundamental ingredients can also be found in NWs having only a local structural deformation. The appearance of the dip in the conductance can be observed even when the Rashba SOC is lacking, but the NW must have a limited region of space where its radius suffers an expansion. On the other hand,

a local radius compression does not trigger the dips in the conductance because the fundamental ingredient of having an attractive potential is lacking in this case. Lastly, we provide a scheme to numerically solve the transport of charges considering the coupling among several scattering channels and the spatial dependence of the localized potential, which made the realization of the study of structural deformations in NW possible. This method is very useful and can be employed to investigate other systems, *e*.g. to study the transport of holes with different effective masses coupled between each other in a heterostructure using the Luttinger Hamiltonian (74). The presented results below were published in Refs. (75, 76).

2.2 Theoretical model

Our model for studying electronic transport in a NW starts by analyzing a system with only the lateral confinement, described by the following Hamiltonian

$$\left[\frac{-\hbar^2}{2m^*}\nabla^2 + V_c(x,y)\right]\Psi(x,y,z) = E\Psi(x,y,z), \tag{2.1}$$

where m^* is the effective mass and $V_c(x,y)$ is the lateral confining potential defined as the harmonic oscillator potential

$$V_c(x,y) = \frac{m^*\omega_0^2}{2}(x^2+y^2), \tag{2.2}$$

where $\omega_0 = \hbar/(m^* r_0^2)$, and r_0 is the NW radius. To solve Equation 2.1, we use the transverse modes $\Phi_{n,m}(x,y)$, which are solutions of the following simplified equation

$$\left[\frac{-\hbar^2\nabla_\perp^2}{2m^*} + \frac{m^*\omega_0^2}{2}(x^2+y^2) - E_{n,m}\right]\Phi_{n,m}(x,y) = 0. \tag{2.3}$$

By using creation and annihilation operators,

$$a_q = \sqrt{\frac{m^*\omega_0}{2\hbar}}q + \frac{i}{\sqrt{2m^*\hbar\omega_0}}p_q, \tag{2.4a}$$

$$a_q^\dagger = \sqrt{\frac{m^*\omega_0}{2\hbar}}q - \frac{i}{\sqrt{2m^*\hbar\omega_0}}p_q, \tag{2.4b}$$

which $q = x, y$ and $p_q = -i\hbar\frac{\partial}{\partial q}$, we can rewrite Equation 2.3 as

$$\hbar\omega_0\left[a_x^\dagger a_x + a_y^\dagger a_y + 1\right]|\Phi_{n,m}\rangle = E_{n,m}|\Phi_{n,m}\rangle, \tag{2.5}$$

whose eigenvalues are

$$E_{n,m} = \hbar\omega_0(n + m + 1), \tag{2.6}$$

for $n = m = 0, 1, 2, \ldots$, where n (m) are associated to the number operator $N_x = a_x^\dagger a_x$ $(N_y = a_y^\dagger a_y)$.

2.2.1 Rashba SOC

To explore the role when the Rashba SOC is also taken into account, we must add the Rashba term to Equation 2.1. Particularly, in the experiment described in Ref (1), a perpendicular electric field is applied in a finite region along the longitudinal direction of the NW. Once an electric field is applied, the structural inversion asymmetry SOC emerges (77). Moreover, as depicted in Figure 2, the bias voltage applied between source

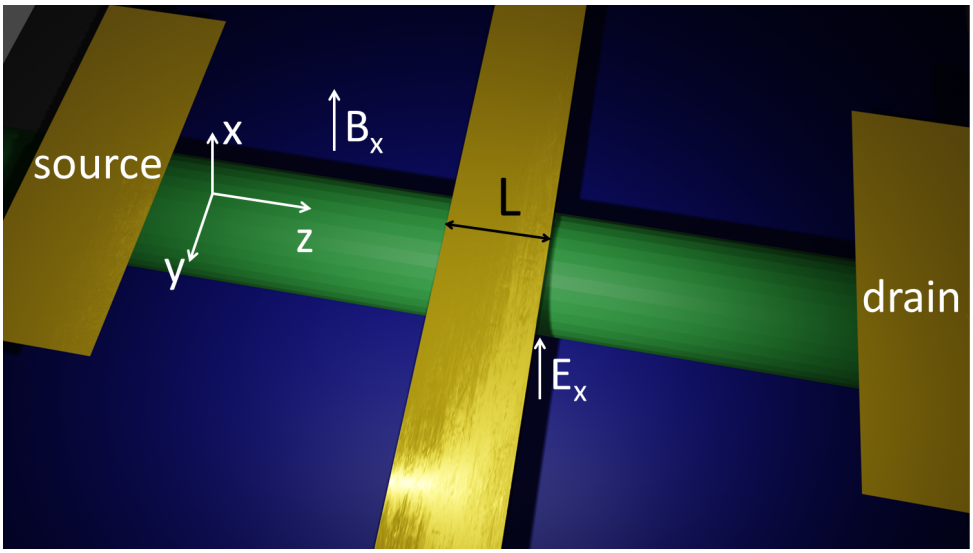

Figure 2 – Schematic picture showing the NW whose longitudinal direction coincides with the z axis. The source and the drain are presented along with the region with length L where the perpendicular electric field E_x between top and bottom gates is applied. The magnetic field, B_x, is applied in the x direction.

and drain triggers a SOC, however, the electric field E_x, applied between top and bottom gates is much higher, thereby causing a strong SOC. With the experimetal description of a SOC in a finite region, we also assume that the Rashba interaction, caused by the electric field E_x, acts only in the region of length L along the z direction, thus given by the following equation

$$H^{SO} = \alpha(z)(k_y\sigma_z - k_z\sigma_y), \tag{2.7}$$

where σ_y (σ_z) and k_y (k_z) are respectively the Pauli spin matrix and the wave vector, defined as $k_q = p_q/\hbar$, in the y-direction (z-direction), and

$$\alpha(z) = \alpha\left[\Theta(z+L) - \Theta(z-L)\right] \tag{2.8}$$

where $\Theta(z)$ is the Heaviside function and α is the Rashba coupling strength. The wave-function can be expanded in the complete basis formed by the transverse modes (channels) such as

$$\Psi^s(x,y,z) = \sum_{n,m} \chi^s_{n,m}(z)\Phi_{n,m}(x,y), \tag{2.9}$$

where $\chi^s_{n,m}(z)$ is the scattering wave-function along the z-direction for each transport channel $j = (n,m,s)$, with spin index $s = \pm$. Therefore, we can calculate the matrix elements for the Hamiltonian

$$H_{j,j'} = \left[\frac{-\hbar^2}{2m^*}\frac{\partial^2}{\partial z^2} + E_j\right]\delta_{j,j'} + H^{SO}_{j,j'} \tag{2.10}$$

where δ is the Kronecker delta and the Rashba elements, with the spin degree of freedom (s) explicitly added, are given by

$$\begin{aligned} H^{SO}_{j,j'}(z) &= \langle \Phi_{n,m}|\alpha(z)k_y\sigma_z - \{\alpha(z),k_z\}\sigma_y|\Phi_{n',m'}\rangle \\ &= -is\left[\alpha(z)b^m_{m'}\delta_{n,n'}\delta_{s,s'} + \{\alpha(z),k_z\}\delta_{n,n'}\delta_{m,m'}\delta_{s,-s'}\right], \end{aligned} \tag{2.11}$$

with the intersubband term

$$b^m_{m'} = \frac{1}{\sqrt{2}r_0}\left[\sqrt{m'}\delta_{m,m'-1} - \sqrt{m'+1}\delta_{m,m'+1}\right] \tag{2.12}$$

and intrasubband term

$$\{\alpha(z),k_z\} = \frac{1}{2}(\alpha(z)k_z + k_z\alpha(z)). \tag{2.13}$$

From which we observe that the intersubband term only couples states with different quantum number m, same quantum number n, and same spin; while the intrasubband term couples states with different spin, and same quantum numbers n and m.

Ideally, we should consider infinite transport channels (subbands) to completely solve the transport along the z direction, but the influence of high energy channels would exponentially decay if incoherent transport effects were considered, in the same way that occurs for the Shubnikov-de Haas oscillations (78). Thus, to extract the basic physics of

the dip in the conductance, we consider the coupling between the lowest energy states. Within this subspace, given by the quantum numbers $j = (0,0,+)$, $(0,0,-)$, $(0,1,+)$, and $(0,1,-)$, we get the following Hamiltonian:

$$H = \begin{pmatrix} \frac{\hbar^2}{2m}\frac{\partial^2}{\partial z^2} + \epsilon & i\{\alpha(z), k_z\} & -i\frac{\alpha(z)}{\sqrt{2}r_0} & 0 \\ -i\{\alpha(z), k_z\} & \frac{\hbar^2}{2m}\frac{\partial^2}{\partial z^2} + \epsilon & 0 & i\frac{\alpha(z)}{\sqrt{2}r_0} \\ i\frac{\alpha(z)}{\sqrt{2}r_0} & 0 & \frac{\hbar^2}{2m}\frac{\partial^2}{\partial z^2} + \lambda & i\{\alpha(z),\ k_z\} \\ 0 & -i\frac{\alpha(z)}{\sqrt{2}r_0} & -i\{\alpha(z),\ k_z\} & \frac{\hbar^2}{2m}\frac{\partial^2}{\partial z^2} + \lambda \end{pmatrix}. \tag{2.14}$$

For these states, we have that $\epsilon = E_{0,0} = \hbar\omega_0$, $\lambda = E_{0,1} = 2\hbar\omega_0$, and the transport wave function can be written as

$$X = \left(\chi^+_{0,0}(z)\ \chi^-_{0,0}(z)\ \chi^+_{0,1}(z)\ \chi^-_{0,1}(z)\right)^{\mathsf{T}}. \tag{2.15}$$

Also, for better visualization, if we use the following linear combination between transport channels with same energy

$$\varphi^{\pm}_{n,m}(z) = (\chi^+_{n,m}(z) \pm i\chi^-_{n,m}(z))\frac{e^{\mp i\theta(z)}}{\sqrt{2}}, \tag{2.16}$$

where $\theta(z) = \int_0^z k_\alpha(z\prime)dz\prime$ and $k_\alpha(z) = m\alpha(z)/\hbar^2$, and we rewrite the transport wave function in this new basis

$$\Phi = \left(\varphi^+_{0,0}(z)\ \varphi^-_{0,0}(z)\ \varphi^+_{0,1}(z)\ \varphi^-_{0,1}(z)\right)^{\mathsf{T}}, \tag{2.17}$$

we arrive at the transformed Hamiltonian

$$H = \begin{pmatrix} \frac{-\hbar^2}{2m}\frac{\partial^2}{\partial z^2} + \epsilon + V_\alpha(z) & 0 & 0 & -i\frac{\alpha(z)}{\sqrt{2}r_0}e^{-2i\theta(z)} \\ 0 & \frac{-\hbar^2}{2m}\frac{\partial^2}{\partial z^2} + \epsilon + V_\alpha(z) & -i\frac{\alpha(z)}{\sqrt{2}r_0}e^{-2i\theta(z)} & 0 \\ 0 & +i\frac{\alpha(z)}{\sqrt{2}r_0}e^{2i\theta(z)} & \frac{-\hbar^2}{2m}\frac{\partial^2}{\partial z^2} + \lambda + V_\alpha(z) & 0 \\ +i\frac{\alpha(z)}{\sqrt{2}r_0}e^{2i\theta(z)} & 0 & 0 & \frac{-\hbar^2}{2m}\frac{\partial^2}{\partial z^2} + \lambda + V_\alpha(z) \end{pmatrix} \tag{2.18}$$

with the intrasubband term of the SOC contribution,

$$V_\alpha(z) = -\frac{m\alpha(z)^2}{2\hbar^2}, \tag{2.19}$$

clearly appears as an effective attractive (negative value) quantum well potential, as also shown in Ref. (72). Its width is determined by L and the depth by the Rashba coupling

strength (proportional to the perpendicular electric field E_x). Equation 2.18 leads to equations coupled in pairs, given by

$$\frac{-\hbar^2}{2m}\frac{d^2\varphi^{\pm}_{0,0}(z)}{dz^2} + [\epsilon - E - V_\alpha(z)]\varphi^{\pm}_{0,0}(z) - i\frac{\alpha(z)}{\sqrt{2}r_0}e^{-2i\theta(z)}\varphi^{\mp}_{0,1}(z) = 0, \tag{2.20a}$$

$$\frac{-\hbar^2}{2m}\frac{d^2\varphi^{\pm}_{0,1}(z)}{dz^2} + [\lambda - E - V_\alpha(z)]\varphi^{\pm}_{0,1}(z) + i\frac{\alpha(z)}{\sqrt{2}r_0}e^{+2i\theta(z)}\varphi^{\mp}_{0,0}(z) = 0. \tag{2.20b}$$

Equation 2.20a and Equation 2.20b were deduced in the simplest scenario to demonstrate that, by considering the coupling between only four states and the mere presence of the Rashba SOC within a finite region, the necessary conditions to observe the resonant reflection (73) are satisfied; they are

(i) the existence of an attractive potential $V_\alpha(z)$

(ii) the coupling between different channels ruled by the term $\pm i\frac{\alpha(z)}{\sqrt{2}r_0}e^{\pm 2i\theta(z)}$

both more easily identifiable from the change of basis.

2.2.2 Structural deformation

In a second approach, we will study the electronic transport in a NW with structural deformation, initially without the Rashba SOC, to reach the dip in the conductance. For this modeling, we will add the potential $V(x, y, z)$ describing the structural deformation in the Equation 2.1. As illustrated in Figure 3, we separate NW into three regions: region I corresponding to $z \leq -L/2$, region II corresponding to $|z| \leq L/2$, and region III corresponding to $z \geq L/2$. Moreover, we assume that $V(x, y, z)$ is different from zero only in the finite region II and model the z-dependence of the radius by the function

$$r(z) = r_0 + \Delta r(z), \tag{2.21}$$

with r_0 the NW radius, as previously defined, and $\Delta r(z)$ is the variation of the radius in the region II. We choose two different forms for the radius variation,

$$\Delta r_1(z) = \Delta r_0(1 - \frac{2|z|}{L}), \quad \text{for} \quad |z| \leq L/2, \tag{2.22}$$

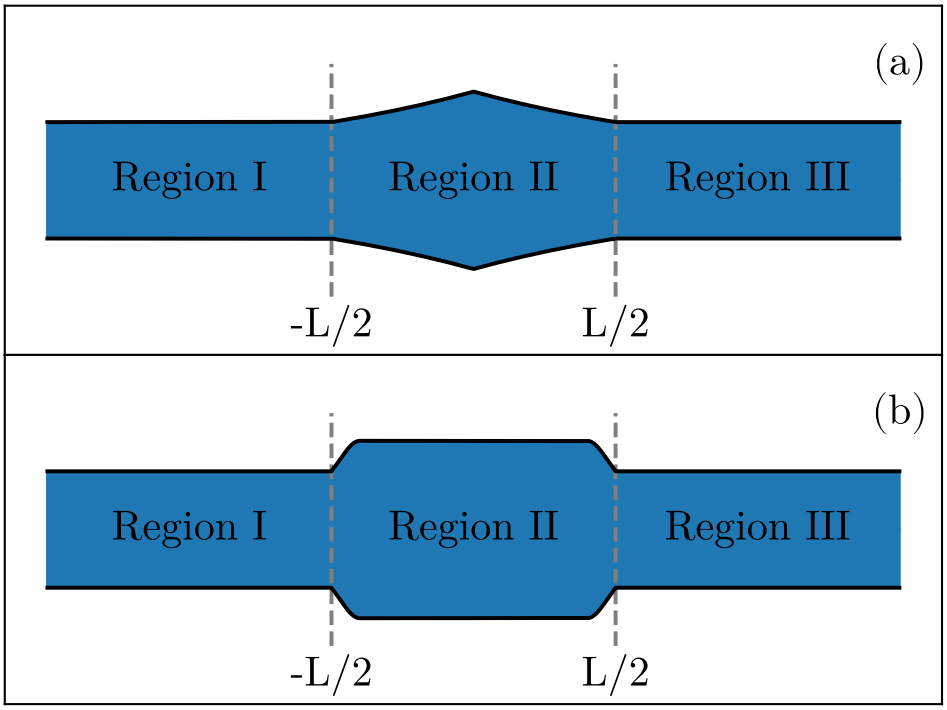

Figure 3 – Schematic picture showing the longitudinal cut of the NW containing an expansion of the radius in the region II with length L. Panel (a) shows the cone-shape deformation $\Delta r_1(z)$, while panel (b) shows the square-shape deformation $\Delta r_2(z)$.

and

$$\Delta r_2(z) = \Delta r_0 = \begin{cases} \sin\left(\frac{\pi(z+L/2)}{2L_0}\right), & \text{for} \quad -\frac{L}{2} \leq z < -\frac{L}{2} + L_0 \\ 1, & \text{for} \quad -\frac{L}{2} + L_0 \leq z \leq \frac{L}{2} - L_0 \\ \sin\left(\frac{\pi(L/2-z)}{2L_0}\right), & \text{for} \quad \frac{L}{2} - L_0 < z \leq \frac{L}{2} \end{cases} \tag{2.23}$$

where Δr_0 is the maximum variation of the radius at $z = 0$ and L_0 defines the the width of the ramp between zero and Δr_0. The first form $\Delta r_1(z)$ describes a NW with a cone-shape deformation (panel (a) of Figure 3), while the second form $\Delta r_2(z)$ produces a square-shape deformation (panel (b) of Figure 3). We choose these two forms to probe the effects of different shapes of deformations in the electronic transport properties. The main difference between both shapes is that the square-shape deformation has a bigger area than the cone-shape deformation. Furthermore, it is good to make it explicit that for $\Delta r_0 < 0$ there is a contraction and for $\Delta r_0 > 0$ there is a expansion of the NW. Furthermore, in

the region II, we have a change in the radius that causes a change in the confinement, which can be described by $\omega(z) = \hbar/(m^* r(z)^2)$. Therefore, the scattering potential can be modeled as

$$V(x, y, z) = \frac{m^*[\omega(z)^2 - \omega_0^2]}{2}(x^2 + y^2), \tag{2.24}$$

whose matrix elements are given by

$$\begin{aligned} V^{n,m}_{n',m'}(z) &= v(z)\langle\Phi_{n,m}|(a_x + a_x^\dagger)^2 + (a_y + a_y^\dagger)^2|\Phi_{n',m'}\rangle \\ &= v(z)\left[d^n_m\delta_{n,n'}\delta_{m,m'} + c^n_{n'}\delta_{m,m'} + c^m_{m'}\delta_{n,n'}\right], \end{aligned} \tag{2.25}$$

where

$$v(z) = \frac{\hbar[\omega(z)^2 - \omega_0^2]}{4\omega_0}, \tag{2.26}$$

and

$$d^n_m = (2n + 2m + 1) \tag{2.27a}$$

$$c^n_{n'} = \left(\sqrt{n'(n'-1)}\delta_{n,n'-2} + \sqrt{(n'+1)(n'+2)}\delta_{n,n'+2}\right). \tag{2.27b}$$

In Equation 2.25, there are the diagonal terms proportional to $V^d_{n,m}(z) = d^n_m v(z)$ and the off-diagonal terms that couples channels that obey the selection rules $n = n' \pm 2$ with $m = m'$ or $m = m' \pm 2$ with $n = n'$. The diagonal terms can be rewritten as a function of the radius variation

$$V^d_{n,m}(z) = d^n_m \hbar\omega_0 \frac{[r_0^4 - r(z)^4]}{4r(z)^4}; \tag{2.28}$$

thereby, showing that it is an attractive potential if the radius within the region II increases ($r(z) \geq r_0$). For a narrowed NW in the region II, we have that $r(z) \leq r_0$ and the diagonal term becomes a repulsive potential.

2.2.3 Numerical solution

To be able to solve the transport in the NW with Rashba SOC or with structural deformation potential, we will observe that for both cases the expansion of the wave-function was performed in the basis of the transverse modes. Therefore, the equation we need to solve depends only on the scattering-wave functions $\chi^s_{n,m}(z)$,

$$\left[\frac{-\hbar^2}{2m^*}\frac{\partial^2}{\partial z^2} + (E_j - E)\right]\chi_j(z) - \sum_{j'} H_{j,j'}(z)\chi_{j'}(z) = 0 \tag{2.29}$$

for each transport channel $j = (n, m, s)$, with spin index $s = \pm$, and the z-dependent Hamiltoninan $H(z)$ including $V(z)$ and/or $H^{SO}(z)$.

Usually, wave-functions are written in a vectorial form, but here we must use the matrix form to be able to implement the numerical scheme. This matrix form also has the advantage of considering the injection of electrons in different channels and solving these different channels at once. We assume that there are three distinct regions where we must compute the wave function. In the region I, the matrix elements of the wave-function χ^{I} are defined by

$$\chi^{\mathrm{I}} = \begin{pmatrix} e^{izk_1} + r_{1,1}e^{-izk_1} & r_{1,2}e^{-izk_1} & \dots & r_{1,N}e^{-izk_1} \\ r_{2,1}e^{-izk_2} & e^{izk_2} + r_{2,2}e^{-izk_2} & \dots & r_{2,N}e^{-izk_2} \\ r_{3,1}e^{-izk_2} & r_{3,2}e^{-izk_3} & \dots & r_{3,N}e^{-izk_3} \\ \vdots & \vdots & \ddots & \vdots \\ r_{N,1}e^{-izk_N} & r_{N,2}e^{-izK_N} & \dots & e^{izk_N} + r_{N,N}e^{-izk_N} \end{pmatrix} \tag{2.30}$$

In regions II and III, the matrix form for the wave-function respectively are

$$\chi^{\mathrm{II}} = \begin{pmatrix} \phi_{1,1}(z) & \phi_{1,2}(z) & \dots & \phi_{1,N}(z) \\ \phi_{2,1}(z) & \phi_{2,2}(z) & \dots & \phi_{2,N}(z) \\ \phi_{3,1}(z) & \phi_{3,2}(z) & \dots & \phi_{3,N}(z) \\ \vdots & \vdots & \ddots & \vdots \\ \phi_{N,1}(z) & \phi_{N,2}(z) & \dots & \phi_{N,N}(z) \end{pmatrix}, \tag{2.31}$$

$$\chi^{\mathrm{III}} = \begin{pmatrix} t_{1,1}e^{izk_1} & t_{1,2}e^{izk_1} & \dots & t_{1,N}e^{izk_1} \\ t_{2,1}e^{izk_2} & t_{2,2}e^{izk_2} & \dots & t_{2,N}e^{izk_2} \\ t_{3,1}e^{izk_3} & t_{3,2}e^{izk_3} & \dots & t_{3,N}e^{izk_3} \\ \vdots & \vdots & \ddots & \vdots \\ t_{N,1}e^{izk_N} & t_{N,2}e^{izk_N} & \dots & t_{N,N}e^{izk_N} \end{pmatrix}. \tag{2.32}$$

such that, the wave-function χ^R is the solution of Equation 2.29 in each region $R =$ I, II and III. We also assume that electrons are injected from the left ($z = -\infty$) in the channel index i. Particularly, if the Hamiltonian Equation 2.29 does not depend on spin the transport equations can be solved to each spin separately. Although there are an

infinite number of transverse modes, we truncate the problem to a certain size N. The coefficients $r_{i,j}$ and $t_{i,j}$ represent the reflection and transmission coefficients of an electron injected in j-th channel and scattered in i-th channel, that are independent of z. The $\phi_{i,j}(z)$ are the wave-functions in the scattering region and depend on the potential and Rashba SCO form.

To numerically solve the transport problem, we must be able to find $r_{i,j}$, $t_{i,j}$, and $\phi_{i,j}(z)$. By means of the numerical integration of the coupled second-order ordinary differential equations, one needs to know the wave-functions and its derivatives in a certain point of space to be able to propagate the solution in the whole space. The wave-functions described in Equation 2.30, Equation 2.31, and Equation 2.32 cannot be univocally determined in a certain point of space because they depend on the $r_{i,j}$, $t_{i,j}$, and $\phi_{i,j}(z)$. Thus, we need to rewrite Equation 2.32 in the following way

$$\chi^{\mathrm{III}} = \begin{pmatrix} e^{izk_1} & 0 & \dots & 0 \\ 0 & e^{izk_2} & \dots & 0 \\ \vdots & \vdots & \ddots & \vdots \\ 0 & 0 & \dots & e^{izk_N} \end{pmatrix} \mathbf{t}, \tag{2.33}$$

where

$$\mathbf{t} = \begin{pmatrix} t_{1,1} & t_{1,2} & \dots & t_{1,N} \\ t_{2,1} & t_{2,2} & \dots & t_{2,N} \\ \vdots & \vdots & \ddots & \vdots \\ t_{N,1} & t_{N,2} & \dots & t_{N,N} \end{pmatrix}, \tag{2.34}$$

and redefine the wave-functions such as: $\xi^R = \chi^R \mathbf{t}^{-1}$, where $R =$ (I, II, or III) and $\mathbf{t}^{-1}$ is the inverse of the transmission matrix given in Equation 2.34. With this redefinition, the wave-function in region III does not depend on the transmission coefficients and it is univocally determined. For $z = L/2$, the wave function and its derivative are given by

$$\xi^{\mathrm{III}}(L/2) = \begin{pmatrix} e^{ik_1 L/2} & 0 & \dots 0 & \\ 0 & e^{ik_2 L/2} & \dots 0 & \\ \vdots & \vdots & \ddots & \vdots \\ 0 & 0 & \dots & e^{ik_N L/2} \end{pmatrix}, \tag{2.35}$$

$$\frac{d\xi^{\mathrm{III}}}{dz}(L/2) = \begin{pmatrix} ik_1 e^{ik_1 L/2} & 0 & \dots 0 & \\ 0 & ik_2 e^{ik_2 L/2} & \dots 0 & \\ \vdots & \vdots & \ddots & \vdots \\ 0 & 0 & \dots & ik_N e^{ik_N L/2} \end{pmatrix}, \tag{2.36}$$

thereby, enabling us to match the wave-function and its derivative at the interface,

$$\xi^{\mathrm{III}}(L/2) = \xi^{\mathrm{II}}(L/2), \tag{2.37a}$$

$$\frac{d\xi^{\mathrm{III}}}{dz}(L/2) = \frac{d\xi^{\mathrm{II}}}{dz}(L/2). \tag{2.37b}$$

Through the matching conditions above, we are able to numerically propagate the solution from $z = L/2$ to $z = -L/2$. Such a propagation can be performed, for example, by means of the 4th order Runge-Kutta method applied to Equation 2.29.

$$\xi^{\mathrm{II}}(L/2) \xrightarrow{\text{propagate}} \xi^{\mathrm{II}}(-L/2), \tag{2.38a}$$

$$\frac{d\xi^{\mathrm{II}}}{dz}(L/2) \xrightarrow{\text{propagate}} \frac{d\xi^{\mathrm{II}}}{dz}(-L/2). \tag{2.38b}$$

At $z = -L/2$, we also have to impose the boundary conditions for the first interface,

$$\xi^{\mathrm{II}}(-L/2) = \xi^{\mathrm{I}}(-L/2), \tag{2.39a}$$

$$\frac{d\xi^{\mathrm{II}}}{dz}(-L/2) = \frac{d\xi^{\mathrm{I}}}{dz}(-L/2). \tag{2.39b}$$

By using the numerically evaluated wave-function above, we can find the original wave-functions

$$\chi^{\mathrm{I}}(-L/2) = \xi^{\mathrm{I}}(-L/2)\mathbf{t}, \tag{2.40a}$$

$$\frac{d\chi^{\mathrm{I}}}{dz}(-L/2) = \frac{d\xi^{\mathrm{I}}}{dz}(-L/2)\mathbf{t}. \tag{2.40b}$$

These two last equations form a system of linear equations with $2(N \times N)$ equations and variables, which can be solved numerically. If the wave-functions were written in a vectorial form from the beginning, the matching conditions at $z = -L/2$ would lead to a system of linear equations with different number of equations and variables, which is inconsistent. The reflection $r_{i,j}$ and transmission $t_{i,j}$ coefficients are extracted from the

solutions to the system of linear equations. The conductance can be evaluated through the Landauer-Buttiker formula

$$G = G_0 \mathrm{Tr}[tt^\dagger], \tag{2.41}$$

where $G_0 = e^2/\hbar$ and t is the transmission matrix, whose matrix elements are $t_{i,j}$.

Finally, it is important to note that when Rashba is taken into account, the boundary conditions for the derivative of wave-functions must be reformulated as (79):

$$\frac{d\chi^{\mathrm{III}}}{dz}(L/2) = \frac{d\chi^{\mathrm{II}}}{dz}(L/2) + \frac{i\mathbf{M}}{2}\chi_{II}(L/2) \tag{2.42a}$$

$$\frac{d\chi^{\mathrm{II}}}{dz}(-L/2) = \frac{d\chi^{\mathrm{I}}}{dz}(L/2) - \frac{i\mathbf{M}}{2}\chi_{II}(L/2), \tag{2.42b}$$

where $\mathbf{M}$ is a matrix, whose elements are given by $\mathbf{M}_{i,j} = -2\alpha(z)\delta_{n,n'}\delta_{m,m'}\delta_{s,s'}$ (see Appendix A).

2.3 Results

2.3.1 Rashba SOC

In Figure 4, we plot the numerical solution for the normalized conductance as a function of the total energy, varying the number of states (channels) and considering $\alpha = \alpha_0$ and $L = 8.0r_0$, where $\varepsilon_0 = \hbar\omega_0$, $r_0 = \sqrt{\hbar/(m^*\omega_0)}$, and $\alpha_0 = \varepsilon_0 r_0$, which are the chosen energy, length, and Rashba constant scales. The total energy, E, represents the applied bias, which in turn is equivalent to the variation of the gate-voltage applied along to the NW (80). In Figure 4, the conductance is almost constant for $E > \varepsilon_0$ and no dip is observed if only two channels with quantum numbers $(0, 0, \pm)$ are taken into account (similarly to a strict 1D transport model). However, once four channels $\{(0, 0, \pm),\ (0, 1, \pm)\}$ are considered, a strong reflection occurs, leading to a dip in the conductance, as can be observed in the plot for normalized conductance show in Figure 4 for $E \approx 2\varepsilon_0$. The four-channels case correspond to the numerical solution of Equation 2.20a and Equation 2.20b, which has the intrasubband Rashba SOC term equivalent to an attractive potential in the Region $|z| \leq L/2$. Such a negative potential can support a quasibound state within this region and this state interacts with the continuum states causing the strong reflection due

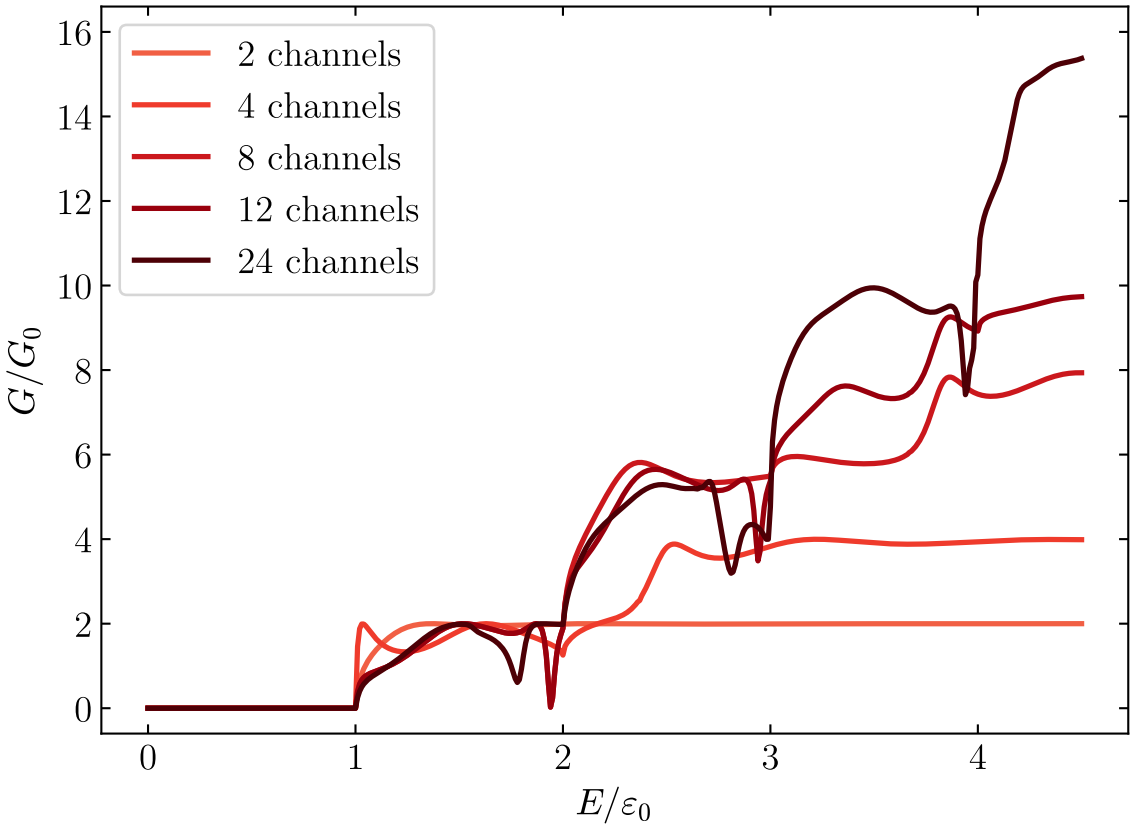

Figure 4 – Normalized conductance as a function of the normalized Fermi energy for 2, 4, 8, 12, and 24 channels, considering $L/r_0 = 8.0$, $\alpha/\alpha_0 = 1.0$, and null magnetic field.

to interference effects. It is interesting to mention that, for $E < 2\varepsilon_0$, only the states $(0, 0, \pm)$ admit scattering modes, whereas the other quantum channels correspond to evanescent modes. Therefore, the influence of evanescent modes in the transport properties is very important, as can be seen when comparing the conductance evaluated using two and four channels in Figure 4. Note that the states $(0, 1, \pm)$ and $(1, 0, \pm)$ are degenerated in energy, but only the state $(0, 1, \pm)$ couples to state $(0, 0, \pm)$; therefore, the conductance including the state $(1, 0, \pm)$ can be easily obtained by adding the constant value G_0 for $E > 2\varepsilon_0$ in the four-channels results of the conductance.

When eight channels are considered, $\{(0, i, \pm),\ (1, 0, \pm)\}$, with $i = 0, \ldots, 2$, the first dip moves to lower energies in the first plateau and no dip is observed for $E > 2\varepsilon_0$. The dip shifts because of the coupling between states $(0, 1, \pm)$ and $(0, 2, \pm)$, which affects the scattering mode $(0, 0, \pm)$. Again, degenerated states $(2, 0, \pm)$ and $(1, 1, \pm)$ do not couple

to the scattering modes and only contribute with a constant value to the conductance evaluated with eight channels for $E > 3\varepsilon_0$. To facilitate the numerical calculations, degenerated states are not taken into account when they dip not couple to the scattering modes within the total energy region considered, and their effect is only adding a constant value G_0 to the conductance when its channel is open.

Considering twelve channels, $\{(0, i, \pm),\ (0, j, \pm)$, with $i = 0, \ldots, 2$ and $j = 0, \ldots, 2$, the first dip does not change because the coupling with the scattering mode with quantum numbers $(0, 0, \pm)$ has not been modified. On the other hand, a dip in the second plateau appears for $E \approx 3\varepsilon_0$ due to the coupling between the scattering mode $(1, 0, \pm)$ and the evanescent modes $(1, 1, \pm)$ and $(1, 2, \pm)$. For 24 channels, $\{(0, i\pm),\ (1, j, \pm),\ (2, k, \pm)\}$, with $i = 0, \ldots, 4$, $j = 0, \ldots, 3$, and $k = 0, \ldots, 2$, the first dip suffers a redshift due to extra coupling between states $(0, 3, \pm)$ and $(0, 4, \pm)$. Two dips in the second plateau appears because of the inclusion of states $(0, 3\pm)$, $(0, 4, \pm)$, and $(1, 3, \pm)$. Furthermore, a reentrance in the third plateau appears for $E \approx 4\varepsilon_0$ due to the coupling between states $(0, 2, \pm)$, $(0, 3, \pm)$, and $(0, 4, \pm)$. We can thus learn from the analysis of the results show in Figure 4 that for $E < E_{n,m}$ the scattering mode designated by quantum numbers (n, m, s) couples to the evanescent mode $(n, m + 1, s)$ through the intersubband term, which causes the dip in the conductance. On the other hand, evanescent modes $(n, m + 1, s)$ and $(n, m + 2, s)$ are coupled to each other, which modifies the conductance by a type of domino effect. Of course, the domino effect keeps influencing the conductance up to a certain value of quantum numbers, where incoherent effects take place. Hereafter, the number of channels will be chosen depending on the range of energy studied, but the minimum number of channels is fixed to 24.

According to Rainis and Loss (80), the smoothness of the electrostatic potential profile between the contacts and the wire plays an important role in the observation of the reentrant behavior for a finite magnetic field. They have shown that the electrostatic potential profile should not be either too smooth or too abrupt to optimize the observation of the dip in the conductance. Based on these discussions, we have also explored the effect of sharpness of the interfaces of the SOC region by adopting a spatial dependence of the

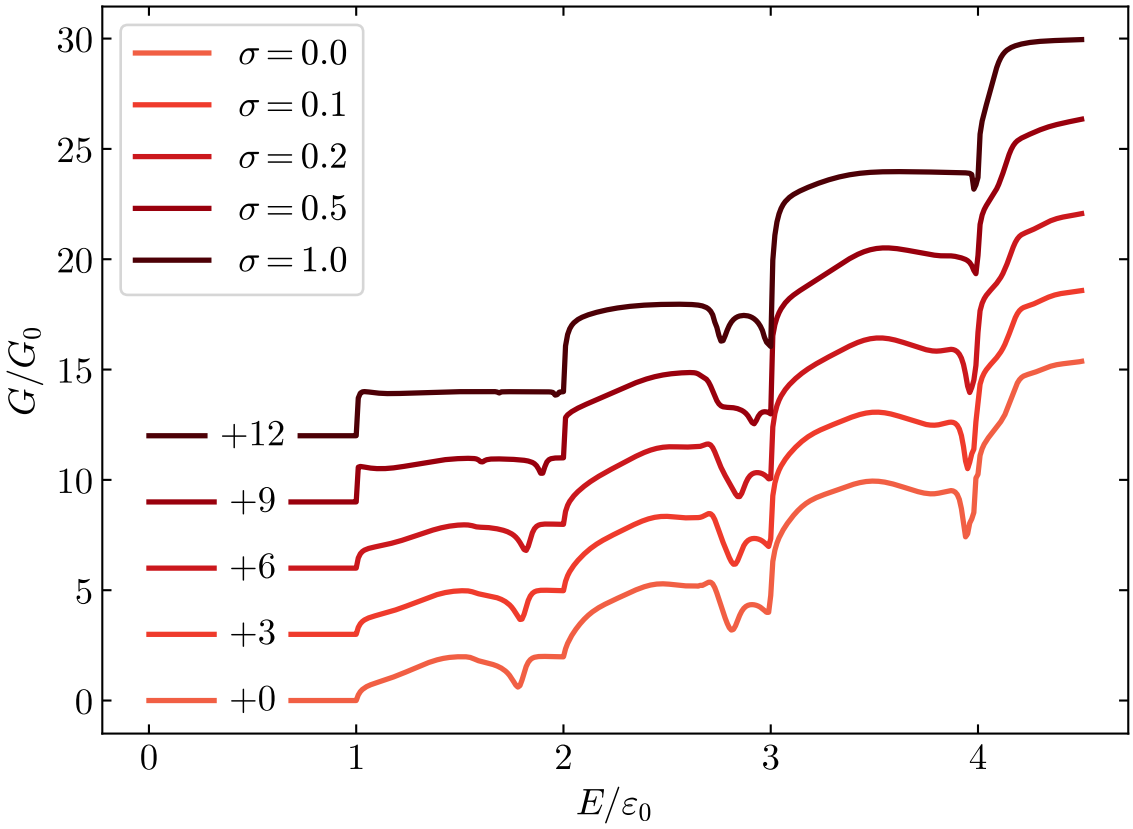

Figure 5 – (a) Normalized conductance as a function of the normalized Fermi energy for 24 channels, $L/r_0 = 8.0$, $\alpha/\alpha_0 = 1.0$, null magnetic field, by changing the degree of smoothness of the SOC region, characterized by $\sigma = 0, 0.1, 0.2, 0.5$, and 1.0. The curves are offset for clarity according to the indicated values.

Rashba coupling constant by

$$\alpha(z) = \alpha \left\{ \frac{1}{1 + e^{(z-L/2)/\sigma}} - \frac{1}{1 + e^{(z+L/2)/\sigma}} \right\}, \tag{2.43}$$

where σ is the degree of smoothness. As can be observed in Figure 5, the conductance obtained in the abrupt case $\sigma = 0$ is not very different from the cases where $\sigma = 0.1$ and 0.2. Only for $\sigma = 0.5$ and 1.0 does the conductance become quantitatively different from the abrupt case, and the dip in the first plateau completely disappears when $\sigma = 1.0$. Therefore, we can conclude that the smoothness of the SOC region affects the dip of the conductance only when it is too smooth. Since the results of the sharp interfaces show a good agreement with the relatively smooth spatial dependence of the SOC region, we will hereafter employ the abrupt model in the numerical calculations.

The normalized conductance for different lengths of the SOC region is show in

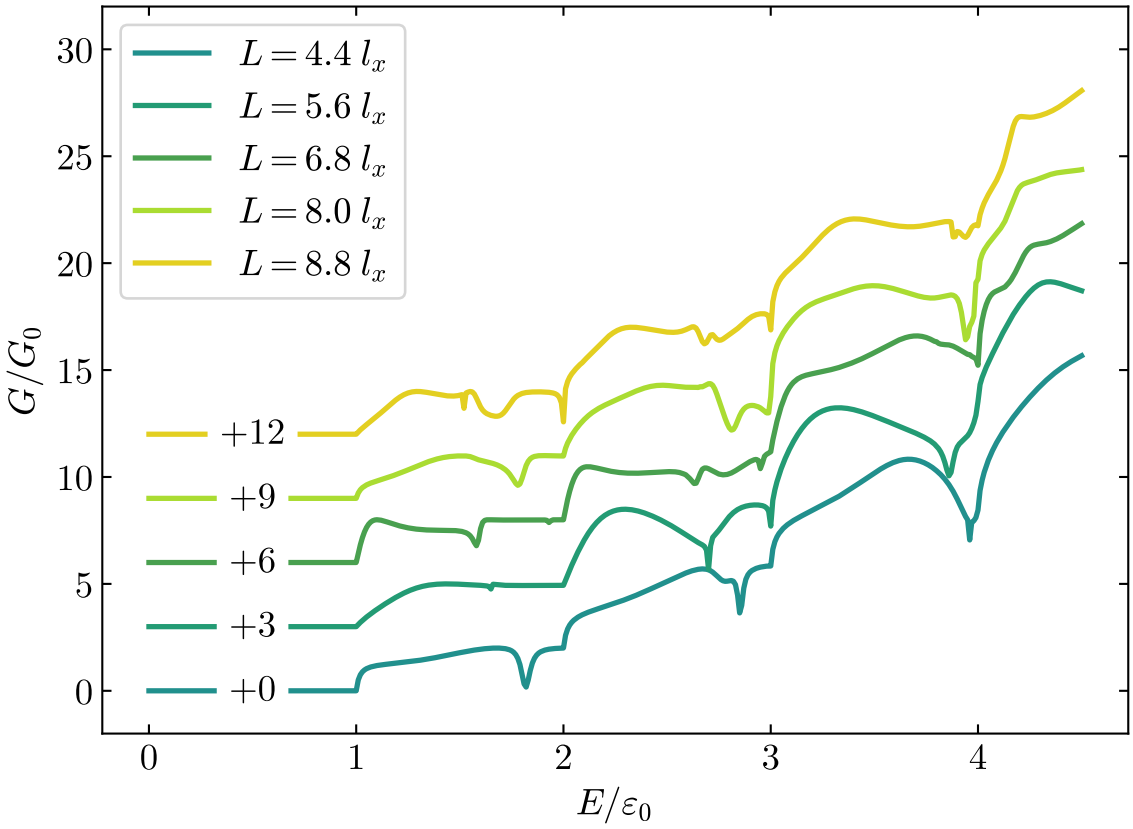

Figure 6 – Normalized conductance as a function of the normalized Fermi energy for 24 channels, considering $L/r_0 = 4.4, 5.6, 6.8, 8.0$, and 8.8, null magnetic field, and $\alpha/\alpha_0 = 1.0$. The curves are offset for clarity according to the indicated values.

Figure 6, considering the following parameters: $L/r_0 = 4.4, 5.6, 6.8, 8.0$ and 8.8, null magnetic field, and $\alpha/\alpha_0 = 1.0$. Showing that the dips can be tuned by modifying the length L. For example, the first dip in $L/r_0 = 4.4$ disappears for $L/r_0 = 5.6$, while it reappears for $L/r_0 = 6.8, 8.0$, and 8.8. In the second plateau, one can find two dips ($L/r_0 = 5.6, 6.8, 8.0$, and 8.8) or just one dip ($L = 4.4r_0$). In Figure 7, we plot the normalized conductance for 24 channels using the same parameters of Figure 4, except for the Rashba constant, which is varied from $\alpha/\alpha_0 = 0.2$ to 1.2 in 0.2 steps. For $\alpha/\alpha_0 = 0.2$ no dips are observed in Figure 7, but for $\alpha/\alpha_0 = 0.4$ the dips already appears. For $\alpha/\alpha_0 = 0.6$, the first dip disappears and the third dip gets wider. When $\alpha/\alpha_0 = 0.8$, two dips appear in the first plateau and the subsequent dips get wider. On the other hand, two dips appear in the second plateau and only one appears in the first plateau when $\alpha/\alpha_0 = 1.0$. For $\alpha/\alpha_0 = 1.2$, the dips in the two plateaus suffer a redshift and the third dip almost

disappears. In (1) the authors report two different values for the Rashba constant coupling $\alpha = 0.8$ eVÅ and $\alpha = 1.2$ eVÅ, which correspond to $\alpha/\alpha_0 = 0.57$ and $\alpha/\alpha_0 = 0.85$ in our simulations. These values are estimated from different experimental techniques and according to the results shown in Figure 7, dips would appear for both experimental values. In summary, both parameters α or L induce the interference between scattering and evanescent modes, which can tune and lead to the appearance of the dips in the conductance.

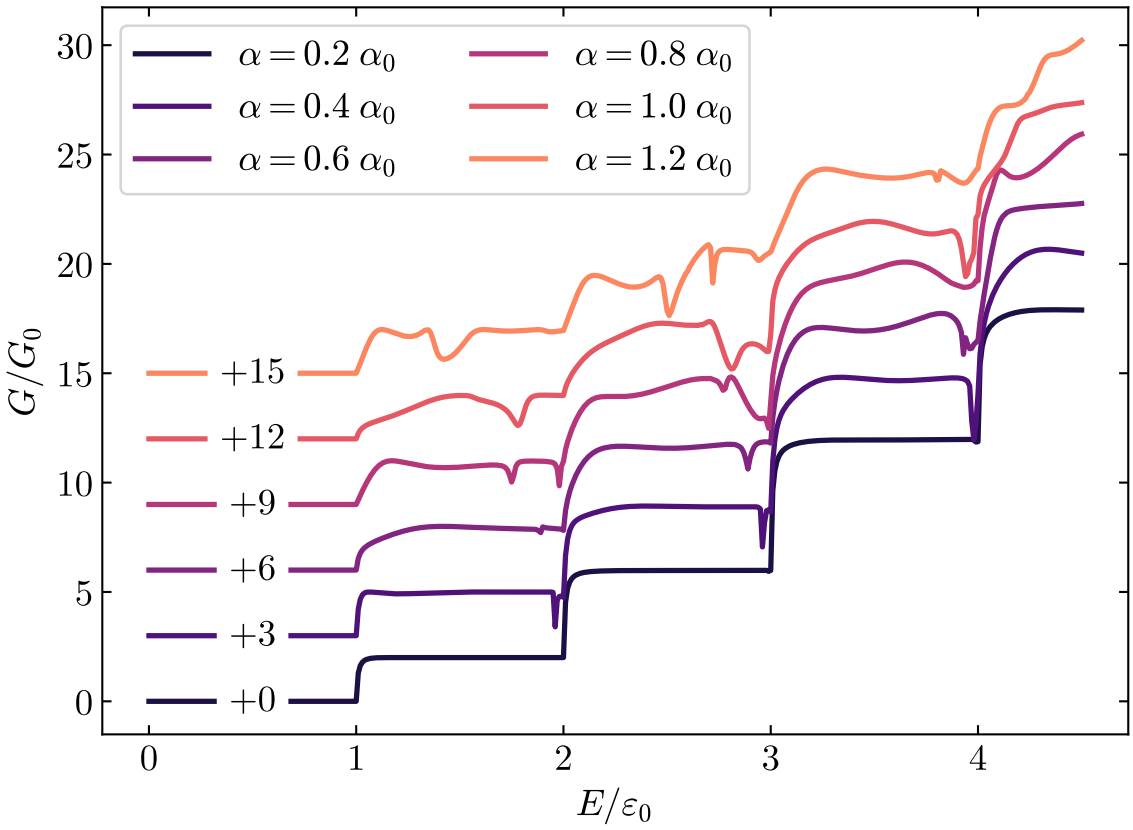

Figure 7 – Normalized conductance as a function of the normalized Fermi energy for 24 channels, considering $L = 8.0r_0$, null magnetic field, and $\alpha = 0.2\alpha_0$, $0.4\alpha_0$, $0.6\alpha_0$, $0.8\alpha_0$, $1.0\alpha_0$, and $1.2\alpha_0$. The curves are offset for clarity according to the indicated values.

In the experiment of Ref. (1), a conductance plateau around $G = 4G_0$ is observed, whereas in Figure 4 to Figure 7 the second plateau correspond to $G = 6G_0$. This is caused by the symmetry of the lateral confinement that provides two scattering modes, $(0, 1, \pm)$ and $(1, 0, \pm)$, degenerated in energy. To obtain $G = 4G_0$, an asymmetry in the confinement

of the NW that breaks this degeneracy must be considered. Thus, the cylindrical NW can be replaced by an eccentric one, changing the lateral confinement potential as

$$V_c(x,y) = \frac{m^*}{2}(\omega_x^2 x^2 + \omega_y^2 y^2) \tag{2.44}$$

where the parameter $\gamma_{xy} = \omega_y/\omega_x = r_x^2/r_y^2$ represents the ratio between the square of the semiaxes of an ellipse in the x and y directions. In this case, the eigenstates are $E_{n,m} = \hbar\omega_x(n + 1/2) + \hbar\omega_y(m + 1/2)$.

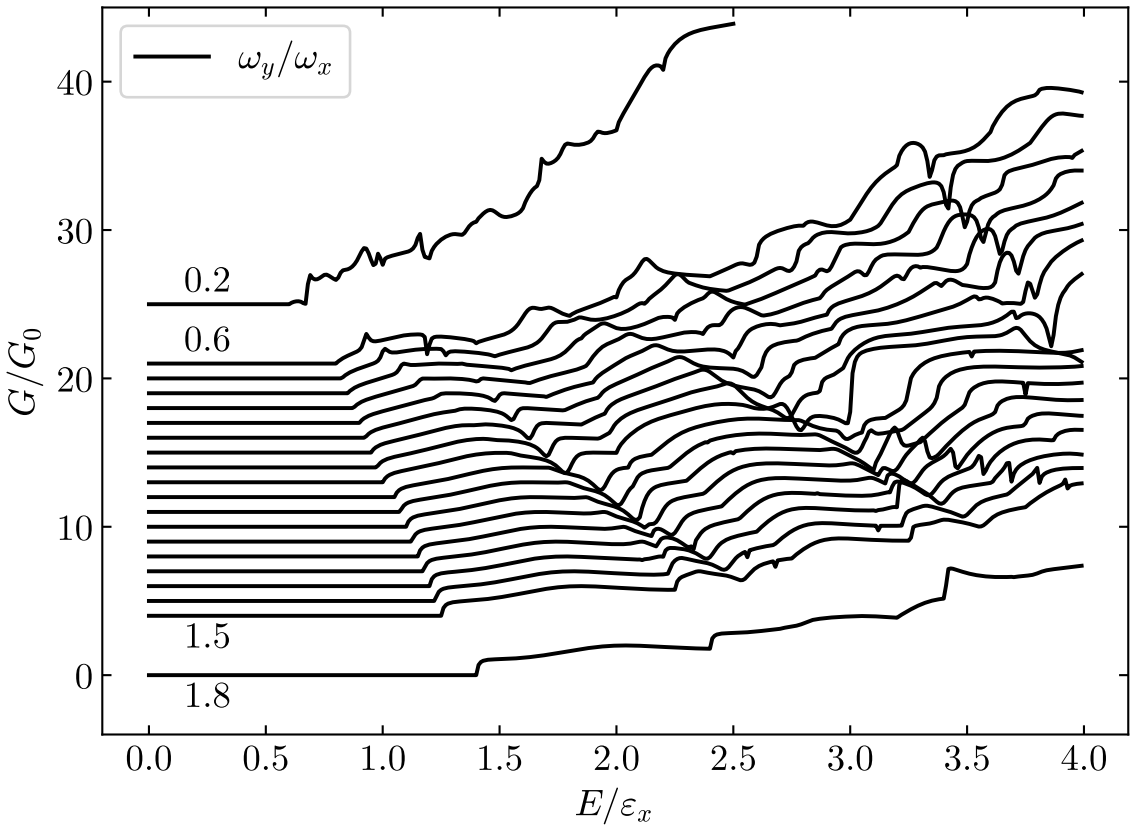

Figure 8 – Normalized conductance as a function of the normalized Fermi energy for 24 channels, considering $L = 8.0r_0$, $\alpha = \alpha_0$, null magnetic field, and different values for $\gamma_{xy} = 0.2$, 0.6 to 1.5 (with step 0.05), and 1.8. The curves are offset for clarity.

In Figure 8, we plot the conductance considering different values of γ_{xy}. In Figure 9, we plot the first dip position (blue dot points) as function of γ_{xy}. Moreover, the blue solid curve id the linear extrapolation of the dip position. When $\gamma_{xy} = 0.2$, the first dip is absent (se Figure 8), and the reason for that can be understood by looking at the crossing (label I in Figure 9) between the extrapolated dip position and the orange curve, which indicates

the minimum energy required for nonzero conductance as function of γ_{xy}. For $\gamma_{xy} \leq 0.2$, the dip does not occur because its position would be a non allowed energy. This effect can also be explained due to the decreasing of the intrasubband term, which is proportional to $\alpha/\sqrt{r_y^2} = \sqrt{\gamma_{xy}}\hbar\omega_x\alpha/\alpha_0$. When $\gamma_{xy} \leq 1$, the intrasubband term becomes very small and the dips are suppressed. In other words, if the NW is very compressed in the x direction (same direction of E_x), the dips might completely vanish.

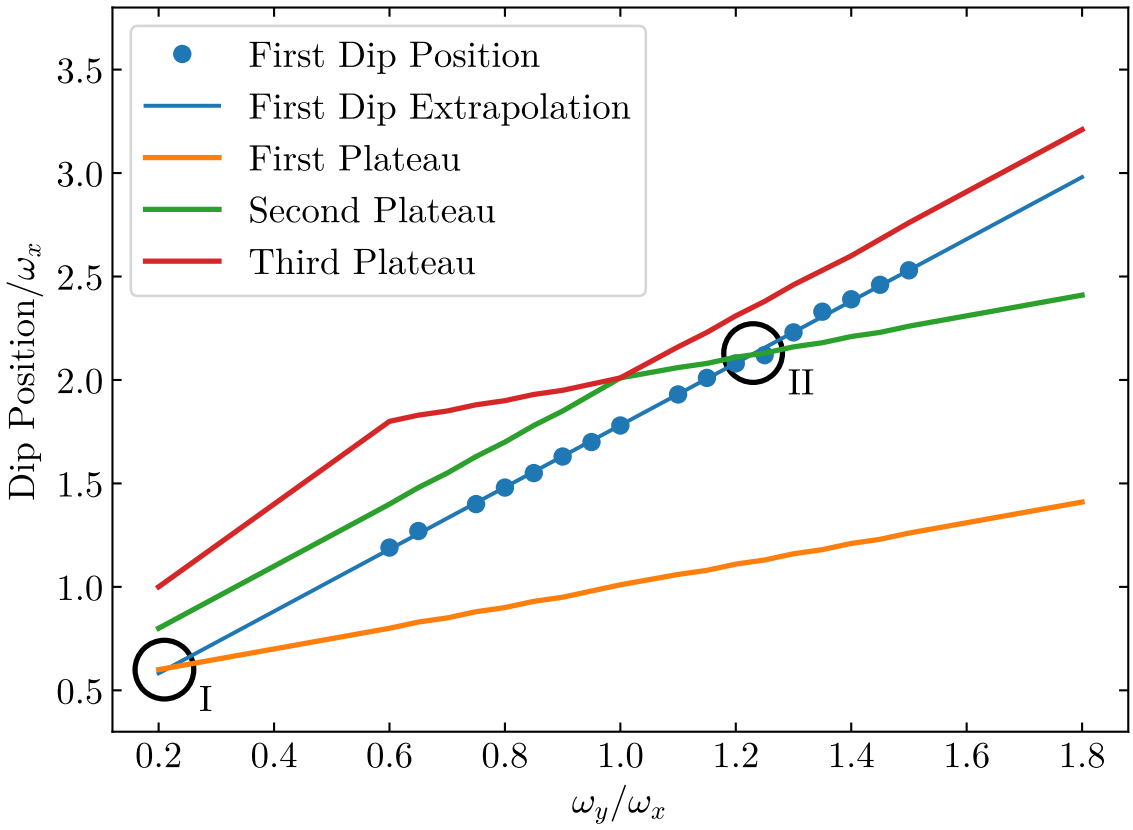

Figure 9 – Dip position in the normalized Fermi energy, E/ω_x, as a function of the ratio ω_y/ω_x, considering $L = 8.0r_0$, $\alpha = \alpha_0$, and null magnetic field.

In Figure 9, the green (red dashed) curve shows the transition between the first (second) and second (third) plateau regions. When $\gamma_{xy} < 1.2$ the dip occurs within the first plateau region, which is delimited by the orange curve and the green curve in Figure 9. When $1.2 \leq \gamma_{xy} \leq 2.2$ the dip occurs within the second plateau region, which is delimited by the green curve and the red curve in Figure 9. Qualitatively, the first dip position is pushed towards higher energies as a function of γ_{xy} and eventually the dip undergo transitions into higher plateaus. Of course, there are other subtleties occurring as γ_{xy} is

varied; for example, when $\gamma_{xy} = 0.7$ there is no dip in the first plateau. On the other hand, by increasing the value from $\gamma_{xy} = 0.75$ to $\gamma_{xy} = 1.5$ both the intensity and width of the first dip increase. Also, for $\gamma_{xy} = 0.6$ and $\gamma_{xy} = 0.65$ the first dip appears as well. All these subtleties occur due to interference phenomena. For $\gamma_{xy} = 1.8$, the dips in the first four plateaus are completely absent and this effect is related to the shift of the dip position to higher energies. Other dips position occurring in plateaus different than the first one shown in Figure 8 also have a linear dependence on γ_{xy} , which is related to the subband energies that linearly vary as a function of γ_{xy}, thereby affecting the energy where the resonant reflection occurs.

2.3.2 Structural deformation

We use the following channels in all numerical calculations using a variation in the quantum number m: $\{(0,0,\pm),(0,1,\pm),(0,2,\pm),(0,3,\pm)\}$, which is a good approximation for Fermi energy $E \leq 4\varepsilon_0$, where $\varepsilon_0 = \hbar\omega_0$. The channels with variation in the quantum number n, such as $\{(0,0,\pm),(1,0,\pm),(2,0,\pm),(3,0,\pm)\}$, are decoupled from the channels where the variation occurs only in m; therefore, the conductance considering the change of both quantum numbers (n,m) is simply obtained by multiplying the results from the variation in the quantum number m by two. We start our analysis by exploring the effect of a narrowed NW ($\Delta r_0 < 0$).

In Figure 10, we plot the normalized conductance G/G_0 as a function of the normalized Fermi energy E/ε_0 for different values of the Δr_0 and for a fixed size of the region II ($L = 8r_0$), considering both shapes of deformation. By increasing the value of $|\Delta r_0|$, one can notice that (i) the Fermi energy where the conductance becomes different from zero shifts towards higher energies as the compression is increased and (ii) the conductance does not exhibit dips and it is smoothed for the cone-shape deformation. Both results are expected because the appearance of the repulsive potential in the diagonal terms of Equation 2.25 for a narrowed NW, which becomes stronger for higher values of $|\Delta r_0|$. The conductance for square-shape deformation (solid lines in Figure 11) resembles the results for a square barrier potential, as would be expected.

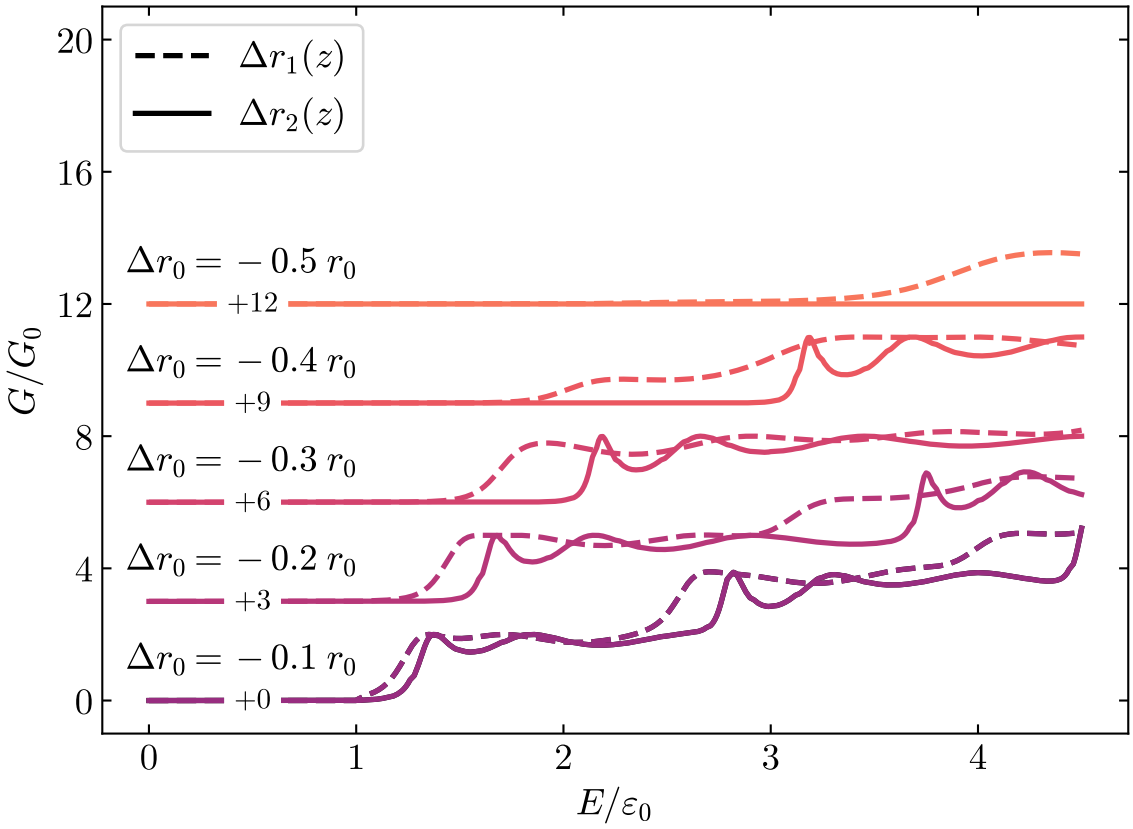

Figure 10 – Normalized conductance as a function of the normalized Fermi energy for different radius contraction $\Delta r_0/r_0 = -0.1, -0.2, -0.3, -0.4$, and -0.5, considering the length $L/r_0 = 8.0$. Solid (dashed) lines describe the results for the square (cone)-shape deformation model. The curves are offset for clarity according to the indicated values.

On the other hand, dips can be observed when an expansion occurs in the radius of the NW in region II. In Figure 11, the normalized conductance is plotted as a function of the normalized Fermi energy considering $\Delta r_0 > 0$ for $L = 8r_0$. The conductance is almost constant within the first plateau ($\varepsilon_0 < E < 2\varepsilon_0$) and the dip is only observed for $\Delta r_0 \geq 0.3r_0$ for the cone-shape deformation (dashed curves in Figure 11). However, many dips are present for an expanded NW for $E > 2\varepsilon_0$, which indicates strong reflection of electrons, manifesting the reentrance behavior within the second and third plateaus. As the value of Δr_0 increases the position of the reentrance changes in the normalized energy axis as can be observed in Figure 11. The square-shape deformation presents more dips in the conductance than the cone-shape deformation because the dips can be related to quasi-bound states localized in region II (81) that interfere to the scattering wave-functions;

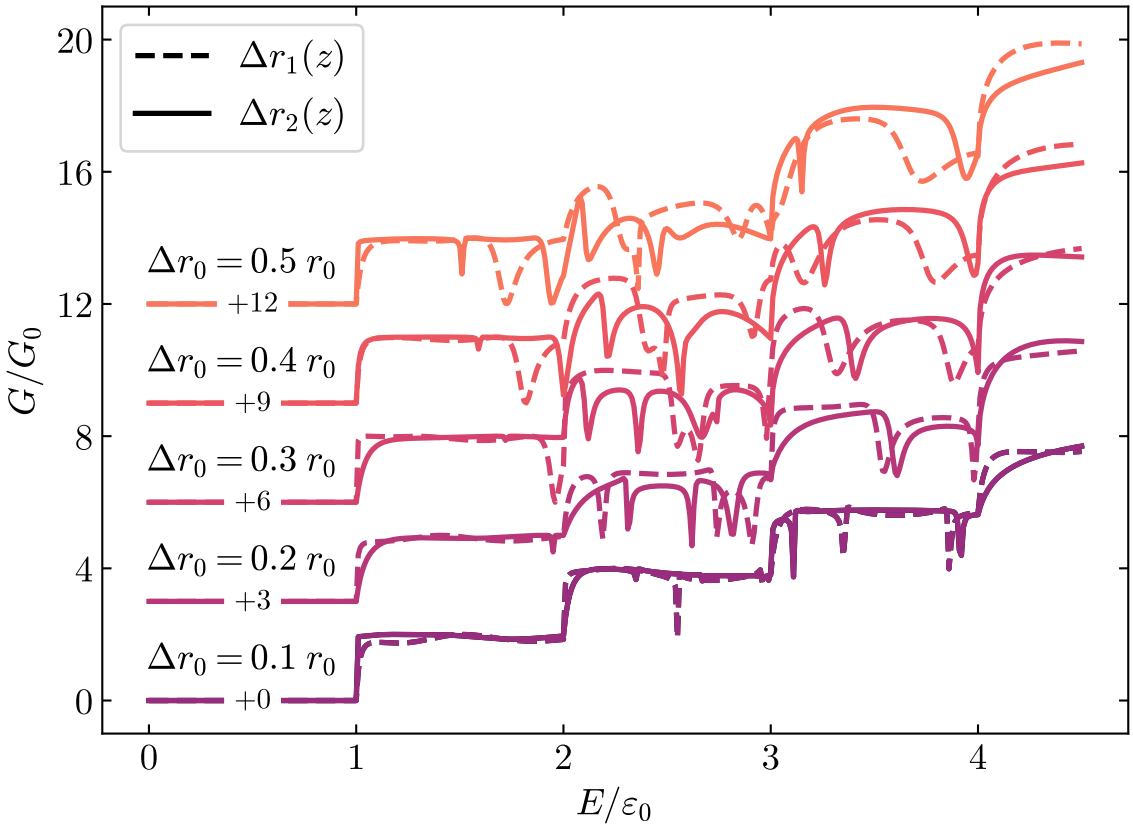

Figure 11 – Normalized conductance as a function of the normalized Fermi energy for different radius expansion $\Delta r_0/r_0 = 0.1, 0.2, 0.3, 0.4$, and 0.5, considering the length $L/r_0 = 8.0$. Solid (dashed) lines describe the results for the square (cone)-shape deformation model. The curves are offset for clarity according to the indicated values.

thus, the wider the potential, the higher the number of quasi-bound states.

To understand the role of the size of the region II, we fix $\Delta r_0 = 0.3 r_0$ and we vary the length $L/r_0 = 4.4, 5.6, 6.8, 8.0$, and, 9.2. Such results are shown in Figure 12. For $L/r_0 = 4.4$ and 5.6, the dip in the first plateau is absent while two dips are present within the second plateau, for the cone-shape deformation (dashed curves in Figure 11). On the other hand, the dip in the first plateau appears for $L/r_0 = 4.4$ and 5.6 when the square-shape deformation is considered (solid curves in Figure 12). For $L/r_0 = 6.8, 8.0$, and, 9.2, a dip in the first plateau is present for $\Delta r_1(z)$ (dashed curves in Figure 12). On the contrary, the dip in the first plateau becomes very narrow for $L/r_0 = 6.8, 8.0$, and, 9.2 when $\Delta r_2(z)$ is employed (solid curves in Figure 12). It can be noted that the number of dips within second and third plateaus are really influenced by the length L due to

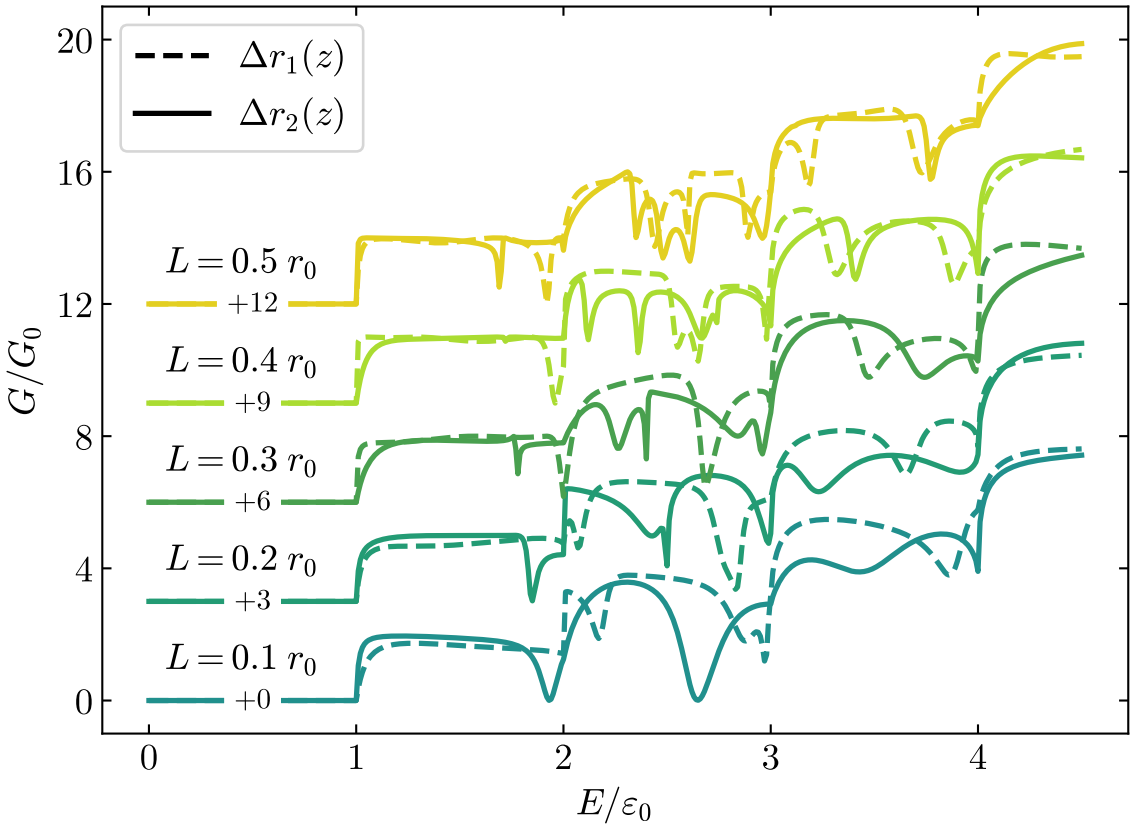

Figure 12 – Normalized conductance as a function of the normalized Fermi energy for different length $L/r_0 = 4.4, 5.6, 6.8, 8.0$, and 9.2, and fixed radius deformation $\Delta r_0/r_0 = 0.3$. Solid (dashed) lines describe the results for the square (cone)-shape deformation model. The curves are offset for clarity according to the indicated values.

interference phenomena occurring between quasi-bound and scattering sates (81). The results of this section demonstrate that the reentrance feature can indeed be observed even in the absence of the SOC and the role of deformations in the transport properties in NWs.

For figures Figure 13, Figure 14, and Figure 15, we include the Rashba SOC with the structural deformation. In Figure 13, we plot the normalized conductance as a function of the Fermi energy considering $\alpha = 0.4\alpha_0$ ($\alpha_0 = \varepsilon_0 r_0$) and for different values for the radius compression, $\Delta r_0/r_0 = 0.0, -0.02, -0.04, \ldots, -0.1$. When $\Delta r_0 = 0.0$, there are two dips in the first plateau at $E \approx 1.8\varepsilon_0$ and $E \approx 2.0\varepsilon_0$ and one dip in the second plateau at $E \approx 3.0\varepsilon_0$ only due to the Rashba SOC. For $\Delta r_0 = -0.02 r_0$, all dips in the conductance are reduced. By further compressing the radius of the NW, one can notice in Figure 13

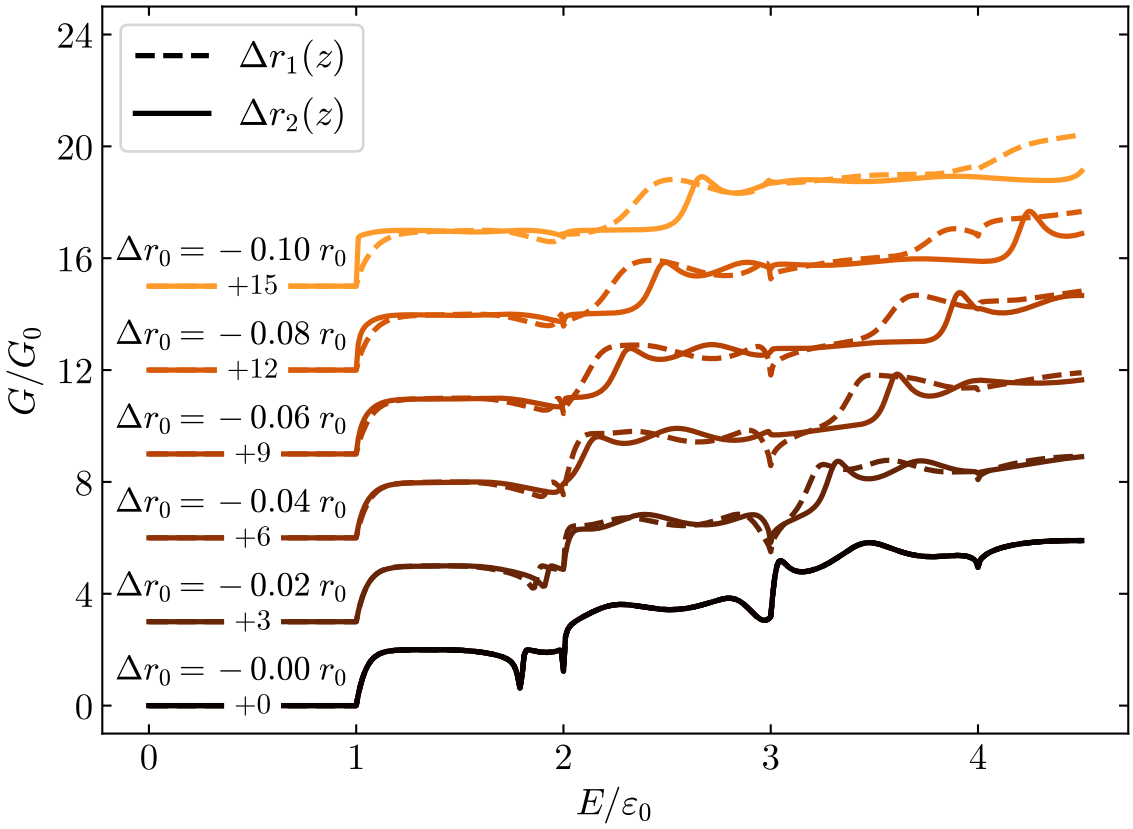

Figure 13 – Normalized conductance as a function of the normalized Fermi energy for different radius contraction $\Delta r_0/r_0 = 0, -0.02, -0.04, -0.06, -0.08$, and -0.1, considering the length $L/r_0 = 8.0$ and the Rashba constant $\alpha/\alpha_0 = 0.4$. Solid (dashed) lines describe the results for the square (cone)-shape deformation model. The curves are offset for clarity according to the indicated values.

that the dips completely disappear for $\Delta r_0 \geq -0.04 r_0$ when the square-shape model is considered (solid curves in Figure 13). These results are expected because the local radius compression works as a repulsive potential, which can cancel the attractive potential given by the SOC (82). When the radius of the NW suffers a local expansion in the same region where the SOC takes place, we have the appearance of more dips and a shift towards smaller energies as the expansion increases, as can be seen in Figure 14.

In Figure 15, we plot the normalized conductance as a function of the Fermi energy considering $\Delta r_0 = 0.04 r_0$ and different values for the Rashba constant ($\alpha/\alpha_0 = 0.0 - 1.0$ with step 0.2). For these parameters, there is no dip in the first plateau for $\alpha = 0.0$, but dips appear for $\alpha \geq 0.2\alpha_0$. One can also notice that both deformation models present different results, even considering a small deformation $\Delta r_0 = 0.04 r_0$. All results presented

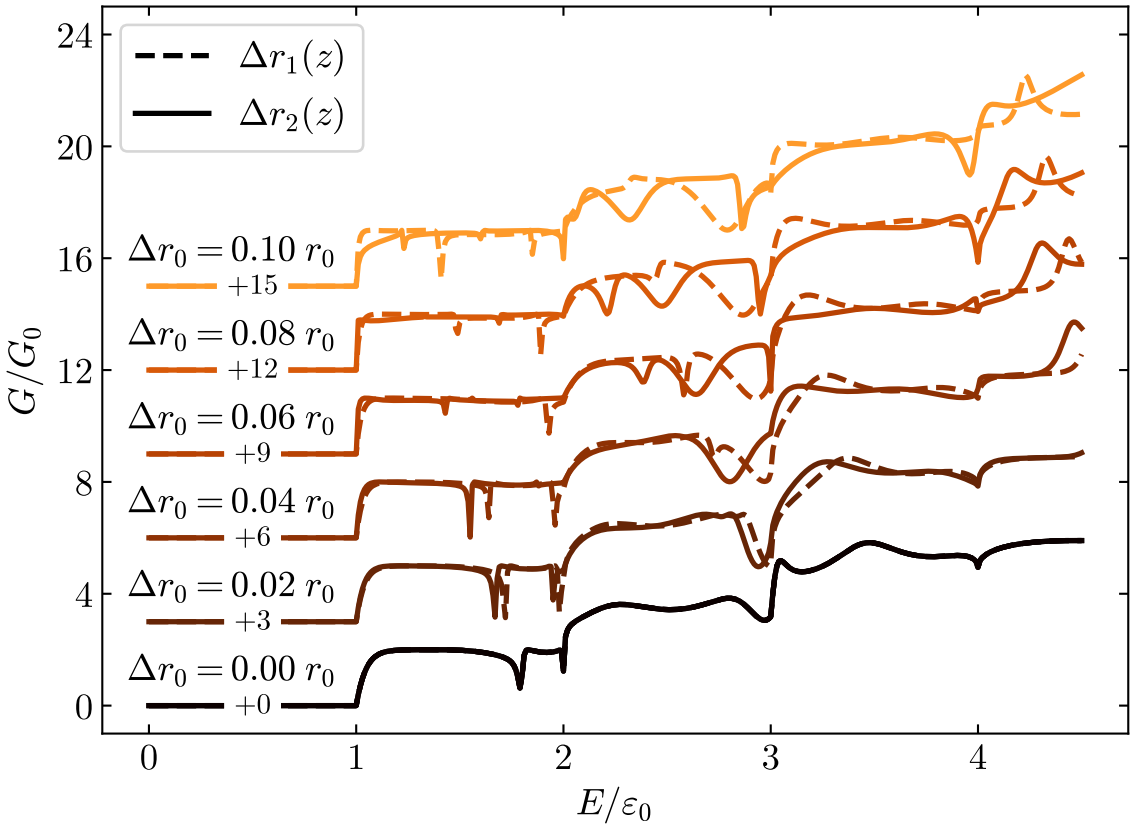

Figure 14 – Normalized conductance as a function of the normalized Fermi energy for different radius expansion $\Delta r_0/r_0 = 0, 0.02, 0.04, 0.06, 0.08$ and 0.1, considering the length $L/r_0 = 8.0$ and the Rashba constant $\alpha/\alpha_0 = 0.4$. Solid (dashed) lines describe the results for the square (cone)-shape deformation model. The curves are offset for clarity according to the indicated values.

in Figure 13, Figure 14, and 15) demonstrate that there is a competition between Rashba SOC and structural deformations, which can cause a misinterpretation of experimental data when related to the reentrant feature.

2.3.3 Magnetic Field

Ideal helical states occur when an external magnetic field is applied to the NW. In the experiment described in (1), it was also observed that the dip in the conductance appears for zero and for moderate values of the magnetic field, but disappears for high field values. In addition to the effects above, we add a uniform magnetic field applied in the x-direction to the previous NW configuration, by adding the Zeeman Hamiltonian

$$H^Z = E_Z \sigma_x, \tag{2.45}$$

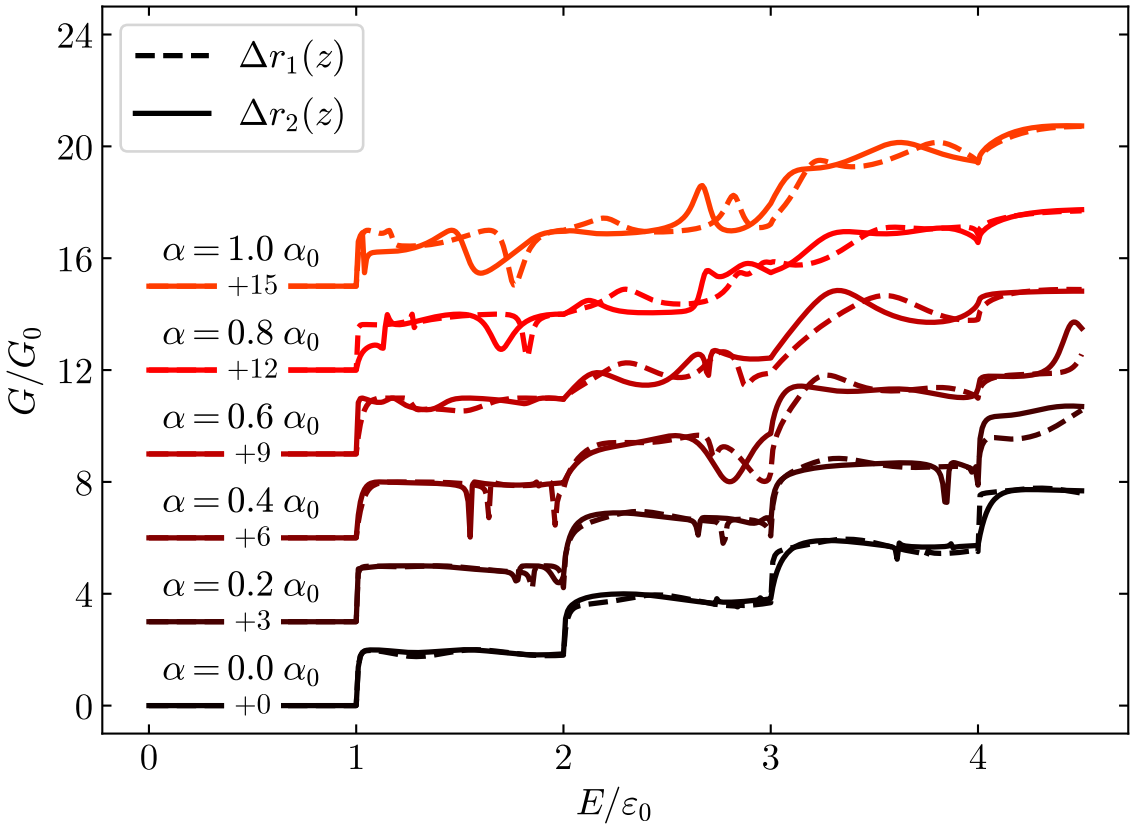

Figure 15 – Normalized conductance as a function of the normalized Fermi energy for a fixed value of the radius expansion $\Delta r_0/r_0 = 0.04$ and length $L/r_0 = 8.0$, considering the variation of the Rashba constant $\alpha/\alpha_0 = 0.0, 0.2, 0.4, 0.6, 0.8,$ and 1.0. The curves are offset for clarity according to the indicated values. Solid (dashed) lines describe the results for the square (cone)-shape deformation model.

where E_Z is the Zeeman energy. The matrix elements for this Hamiltonian are given by

$$H^Z_{j,j'} = E_Z \delta_{n,n'} \delta_{m,m'} \delta_{s,-s'} \tag{2.46}$$

Unlike the Rashba SOC, the magnetic field is present throughout the whole NW. When the magnetic field is included, the subband energy is shifted as $E^{\pm}_{n,m} = E_{n,m} \pm E_Z$. This would move the total energy where the first step in the conductance occurs. Yet, the electron source will be affected by the uniform magnetic field in the same way, thereby canceling out this energy shift. Thus, we have compensated for this difference and considered that the total energy where the first channel opens does not change with the variation of the magnetic field.

In Figure 16, we plot the normalized conductance for different values of the Zeeman

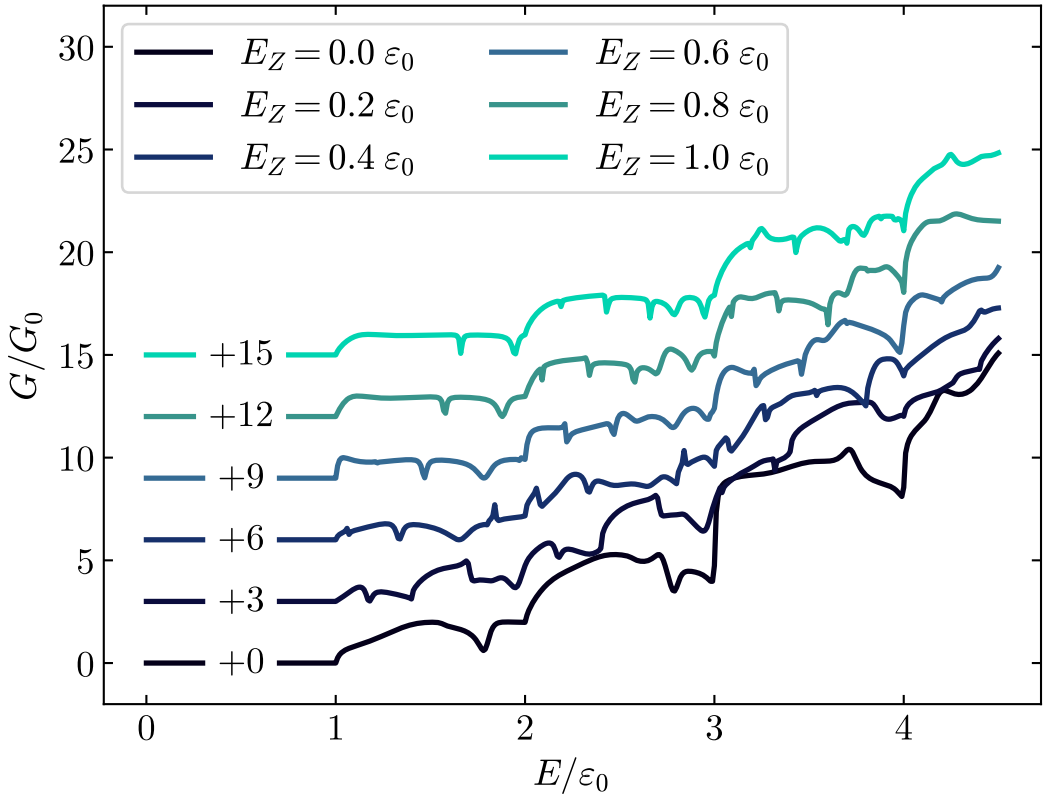

Figure 16 – Normalized conductance as a function of the normalized Fermi energy for 24 channels, considering $L = 8.0r_0$, $\alpha = \alpha_0$, and Zeeman energy in range $E_Z = 0.0\varepsilon_0$ to $2.0\varepsilon_0$

energy, E_Z, as a function of the total energy without any structural deformation. For $E_Z > 0$ and carry on with $\varepsilon_0 = \hbar\omega_0$, the injection of only one electron occurs between $\varepsilon_0 \leq E \leq \varepsilon_0 + 2E_Z$, the injection of two electrons occurs after $E > \varepsilon_0 + 2E_Z$, and so on. The range of energy between $E = 1.8\varepsilon_0$ and $E = 2.2\varepsilon_0$,where the reduction of the conductance happens for $E_Z = 0$, still manifests in a similar way up to $E = 0.8\varepsilon_0$. By using the experimental values for the g factor (1), we can estimate that $E = 0.3\varepsilon_0$ would correspond to a magnetic field of $5T$. Furthermore, the increase of the magnetic field causes a narrowing of dips (see Figure 16). We can thus ascribe the vanishing of the reentrant behavior for high magnetic fields observed in (1) to the combination of the dips' narrowing produced by increasing the magnetic field plus incoherent transport processes. The incoherent transport smears out the reentrant behavior (80) and for high values of the magnetic field it would not allow the appearance of very narrow regions of reflection.

In Figure 17, we plot the normalized conductance for a fixed Zeeman energy, $E_Z = 0.2\varepsilon_0$, as a function of the total energy considering $\alpha = 0.4\alpha_0$, $L = 8r_0$ and different radius contraction $\Delta r_0/r_0 = 0.0, -0.02, -0.04, -0.06, -0.08$, and -0.1. In this case, many dips appear when $\Delta r_0 = 0.0$, but they fade out even for a small compression $\Delta r_0 = -0.04r_0$. By further compressing the NW, we clearly observe the disappearance of the dips for $\Delta r_0 = -0.08r_0$ using the square-model (solid curves in Figure 17). On the other hand, more dips appear for a expanded NW due to interference phenomenon between scattering and quasi-bound states (81), as can be observed in Figure 18. Such results demonstrate how a small structural deformation can play an important role in the observation of the reentrant feature in NWs when a magnetic field and Rashba SOC coexist.

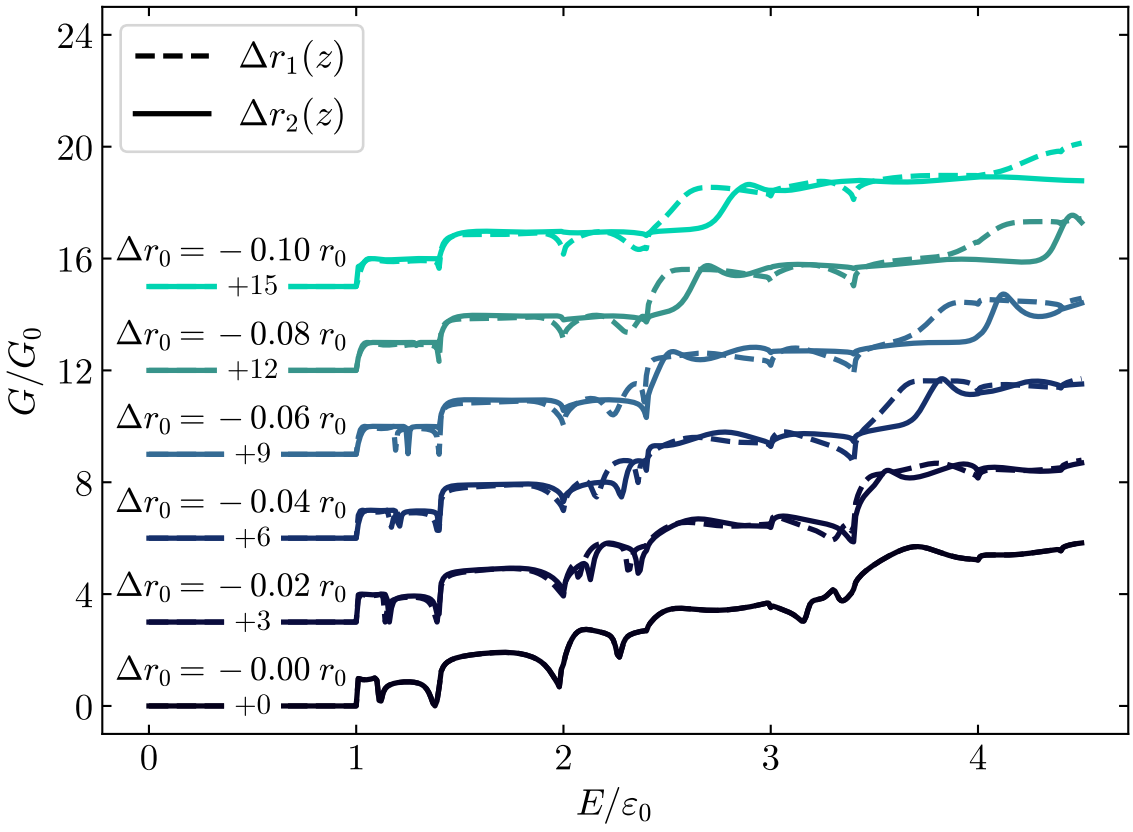

Figure 17 – Normalized conductance as a function of the normalized Fermi energy for different radius contraction $\Delta r_0/r_0 = 0.0, -0.02, -0.04, -0.06, -0.08$, and -0.1, considering the length $L/r_0 = 8.0$, the Rashba constant $\alpha/\alpha_0 = 0.4$, and Zeeman energy $E_Z/\varepsilon_0 = 0.2$. The curves are offset for clarity according to the indicated values. Solid (dashed) lines describe the results for the square (cone)-shape deformation model.

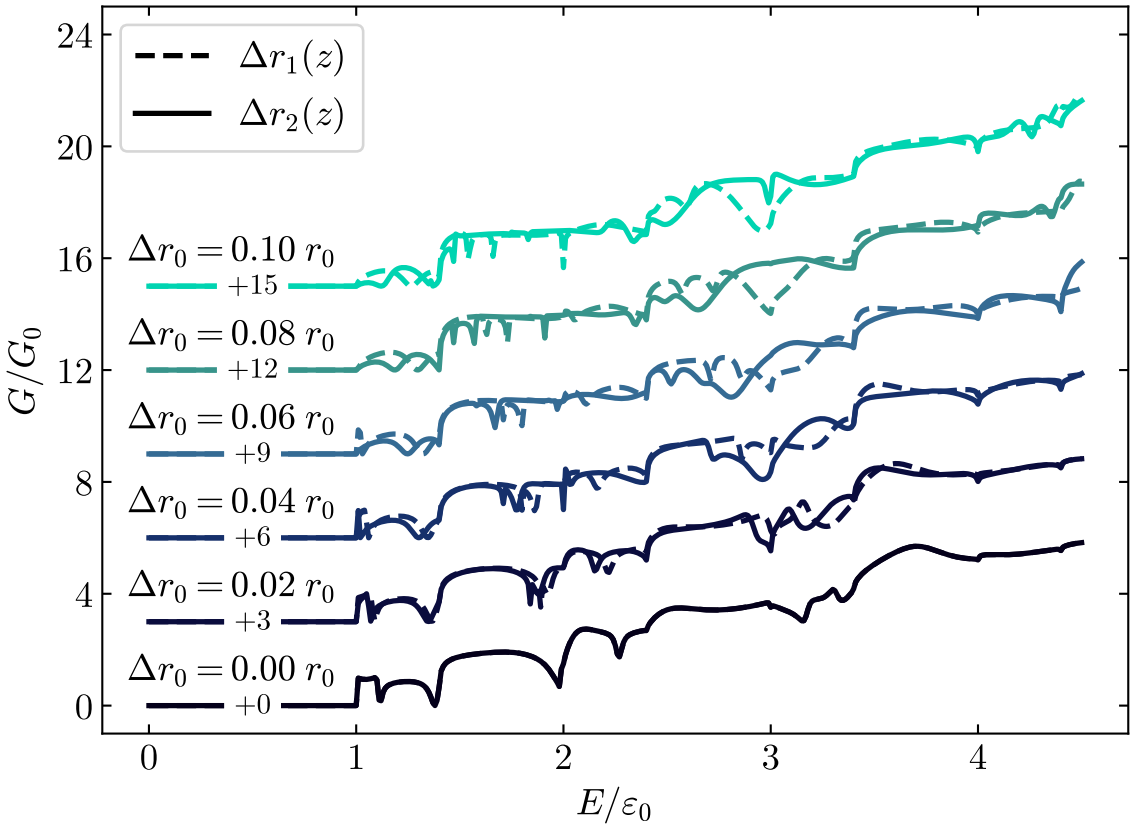

Figure 18 – Normalized conductance as a function of the normalized Fermi energy for different radius expansion $\Delta r_0/r_0 = 0.0, 0.02, 0.04, 0.06, 0.08$, and 0.1, considering the length $L/r_0 = 8.0$, the Rashba constant $\alpha/\alpha_0 = 0.4$, and Zeeman energy $E_Z/\varepsilon_0 = 0.2$. The curves are offset for clarity according to the indicated values. Solid (dashed) lines describe the results for the square (cone)-shape deformation model.

2.4 Conclusion

In conclusion, we presented a theoretical model capable of explaining the reentrant behavior of the conductance in the absence of the external magnetic field and that can be sustained also for finite field values. The dip in the conductance appears because of the resonant reflection which is predicted to occur in quasi-one-dimensional systems if two necessary conditions are met: the existence of an attractive potential and the coupling between different scattering channels, even though the coupling occurs between a scattering and an evanescent mode. Both conditions coexist when the NW experiences the Rashba SOC in a limited region of length L.

Furthermore, we were able to calculate the conductance for an NW containing

structural deformations. We also showed the appearance of reentrant behavior without the Rashba SOC and magnetic field. Moreover, we investigated the effects of structural deformations taking into account an external magnetic field. We found that these deformations affect the observation of the reentrant feature. Particularly, the compression of the NW radius can destroy the dip in the conductance. Here, we focused on structural deformation of the NW, but similar effects would occur in NWs under the presence of a localized potential. We believe the deformations can be experimentally achieved by employing nonuniform top-bottom gates in experiments such as those reported in Refs. (1, 83). Lastly, this work provides an alternative explanation to appearance of the reentrant characteristic for null magnetic field, which is simpler and more direct.

3 Quantum Dot Hamiltonian tomography

3.1 Introduction

In quantum dots, the Hamiltonian describes the energy of electrons confined within the dots and the interactions between them. In this sense, tomographing the Hamiltonian of quantum dots is important because it provides a way to experimentally determine important physical parameters. The reconstruction of the Hamiltonian, for example, gives important knowledge about the electronic and optical properties of quantum dots, which can be used to optimize their performance in real applications.

Quantum dot Hamiltonian tomography typically involves a series of measurements and manipulations of the system, which are used to reconstruct the Hamiltonian using various mathematical techniques. This, in general, requires a very large number of measurements and manipulations, which makes it an extremely time-consuming task for experimentalists.

In this chapter, we use double quantum dots, where the logical qubits are mapped into singlet-triplet states of two electrons. The interqubit interaction is implemented through a capacitive coupling that can generate entanglement, according to the setup of the experimental framework (66). Our goal is to use machine learning tools to determine the parameters of the Hamiltonian that describes the system and to provide some advantage to the time consuming experiments. The basic idea is to use theoretical values calculated from measurements of the spin in each direction at different time values, which can be obtained through the temporal evolution of the system, to train a neural network to predict the parameters of the Hamiltonian. Once the model is trained, it can be used to predict the interqubit coupling using experimental measures of the observables in pratical realizations.

3.2 Theoretical Model

For this study, we use the Heisenberg Hamiltonian to describe the two quantum dots spin qubits as follows

$$\begin{aligned} H = \frac{1}{2} \left[J_1 \left(\sigma_z \otimes \mathbf{I} \right) + J_2 \left(\mathbf{I} \otimes \sigma_z \right) \right. \\ + \frac{J_{12}}{2} \left(\sigma_z \otimes \sigma_z \right) \\ \left. + B_1 \left(\sigma_x \otimes \mathbf{I} \right) + B_2 \left(\mathbf{I} \otimes \sigma_x \right) \right], \end{aligned} \tag{3.1}$$

where, σ_k, for $k = x, y, z$, are the Pauli matrices, $\mathbf{I}$ the identity matrix, J_1 and J_2 the exchange splittings for the first and second qubit, respectively. B_1 and B_2 refer to the external magnetic field gradients on the first and second qubit, respectively. J_{12} in Equation 3.1 is the interqubit interaction coupling. Here, we use the observables $\sigma_k^{(1,2)}$ that locally act on each qubit. Their expected values are calculated by the following expression

$$\langle \sigma_k^{(1,2)}(t) \rangle = \langle \psi(t) | \sigma_k^{(1,2)} | \psi(t) \rangle, \tag{3.2}$$

where the index in parentheses represents the measured qubit, that is $\sigma_k^{(1)} = (\sigma_k \otimes \mathbf{I})$ and $\sigma_k^{(2)} = (\mathbf{I} \otimes \sigma_k)$, and $\psi(t)$ is the evolved vector state at time t. Moreover, in the the Schrödinger picture, the dynamics of the system is given by

$$H|\psi(t)\rangle = i\hbar \frac{\partial}{\partial t} |\psi(t)\rangle. \tag{3.3}$$

For a time independent Hamiltonian, we can use the time-evolution operator as $U(t, t_0) = e^{-iH(t-t_0)}$ to calculate the evolved state $|\psi(t)\rangle = U(t, t_0)|\psi(t_0)\rangle$ given an initial state $|\psi(t_0)\rangle$ and therefore, Equation 3.2 becomes

$$\langle \sigma_k^{(1,2)}(t) \rangle = \langle \psi(t_0) | U^\dagger(t, t_0) \sigma_k^{(1,2)} U(t, t_0) | \psi(t_0) \rangle. \tag{3.4}$$

In particular, when the external magnetic field is null, $B_1 = B_2 = 0$, the problem has analytical solution, and it is possible to find a solution for each of the expected values as a function of each of the splittings (J_1 and J_2) and coupling (J_{12}) parameters of the

Hamiltonian. Using as the initial state $|\psi(t_0)\rangle = |{+}{+}\rangle$, we obtain

$$\langle\sigma_x^{(1,2)}(t)\rangle = \cos\left[J_{(1,2)}(t-t_0)\right]\cos\left[\frac{J_{12}}{2}(t-t_0)\right], \tag{3.5a}$$

$$\langle\sigma_y^{(1,2)}(t)\rangle = \sin\left[J_{(1,2)}(t-t_0)\right]\cos\left[\frac{J_{12}}{2}(t-t_0)\right], \tag{3.5b}$$

$$\langle\sigma_z^{(1,2)}(t)\rangle = 0, \tag{3.5c}$$

for each qubit index $(1,2)$ and initial time t_0. These results show that the values of the observables are sinusoidal functions that depend on the product $J_{(1,2)}t$. This product must be taken into account when choosing time values depending on the values of $J_{(1,2)}$. Furthermore, using B different of 0, when the two qubit interaction coupling is null (or at least $J_{12} \to 0$) each qubit becomes independent, and the Hamiltonian can be written as

$$H^{(1,2)} = \frac{1}{2}\left(J_{(1,2)}\sigma_z^{(1,2)} + B_{(1,2)}\sigma_x^{(1,2)}\right). \tag{3.6}$$

The analytical solution for the observables in this particular configuration using the same initial state $|{+}{+}\rangle$ is,

$$\langle\sigma_x^{(1,2)}(t)\rangle = 1 - \frac{2J_{(1,2)}^2}{B_{(1,2)}^2 + J_{(1,2)}^2}\sin^2\left[\frac{1}{2}\sqrt{B_{(1,2)}^2 + J_{(1,2)}^2}(t-t_0)\right], \tag{3.7a}$$

$$\langle\sigma_y^{(1,2)}(t)\rangle = \frac{J_{(1,2)}}{\sqrt{B_{(1,2)}^2 + J_{(1,2)}^2}}\sin\left[\sqrt{B_{(1,2)}^2 + J_{(1,2)}^2}(t-t_0)\right], \tag{3.7b}$$

$$\langle\sigma_z^{(1,2)}(t)\rangle = \frac{2B_{(1,2)}J_{(1,2)}}{B_{(1,2)}^2 + J_{(1,2)}^2}\sin^2\left[\frac{1}{2}\sqrt{B_{(1,2)}^2 + J_{(1,2)}^2}(t-t_0)\right]. \tag{3.7c}$$

3.3 Machine Learning

Recent developments on machine learning can be largely traced back to a series of breakthroughs in the development of powerful neural network models, where data is processed through the sequential combination of multiple nonlinear layers. Such models solve fundamental problems in real world tasks, namely the problem of automatically extracting knowledge from raw noisy data, rather than relying on hard-coded knowledge directly inscribed in the algorithms by a human. For practical purposes, the machine learning algorithms can be divided into the categories of supervised, unsupervised, and reinforcement learning, all of which have found applications to quantum systems. While

there is no formal difference between some of the algorithms in these categories, such a division is often used as a way to specify the details of the algorithms, the training setup, and the structure of the data sets involved.

We chose to use the supervised learning algorithm, were it tasks aim at predicting a target output vector $\mathbf{y}$ associated with the input vector $\mathbf{x}$, both of which can be discrete or continuous. The training data is thus a list of pairs of input and output tuple $\{\mathbf{x}, \mathbf{y}\}$, where target output conveys that such a vector corresponds to the ideal output given the input vector. Within the scope of the measure, the method includes classification, where the objective is to assign each input vector to one of a set of discrete categories, and regression, where the output is a vector with continuous entries.

In our approach, the input and output vectors, called from hereafter as input features and output parameters, are the measures of the observables, given by Equation 3.2, and the parameters of the Hamiltonian in Equation 3.1, respectively. Therefore, for the numerical simulation, we are going to use randomly generated parameter values, named input parameters (J_1, J_2, B_1, B_2, and J_{12}), to calculate the input features ($\langle\sigma_x^{(1,2)}(t)\rangle$, $\langle\sigma_y^{(1,2)}(t)\rangle$, $\langle\sigma_z^{(1,2)}(t)\rangle$), then the trained machine will predict the output parameters (Pred(J_1), ..., Pred(J_{12})), and we will compare them with the initially generated input parameters to calculate the associated error. For the machine learning training, a set of predefined parameter values will be used, and therefore a defined set of features. Both the input and training parameters will be set in the same interval of values. Thus, from now on, the interval notation $[min,\ max,\ step]$ will be used to indicate the values used in each parameter for construction of training table. As for the test tables, we will use random values within the same range $[min,\ max]$. Finally, we should note that the number of measurements is associated with the number of steps in time. Therefore, a fixed amount of N measures will be defined and will be used for each of the observables $(\langle\sigma_{(1,2)}^{(k)}(t_1)\rangle, \langle\sigma_{(1,2)}^{(k)}(t_2)\rangle, ..., \langle\sigma_{(1,2)}^{(k)}(t_N)\rangle)$.

3.4 Results

In this section, the training results will be presented through three major categories: (i) general values of J_1, J_2 and J_{12} at the same range, with $B_1 = B_2 = 0$, (ii) positive values of J_1, J_2 and J_{12} with $B_1 = B_2 = 0$ and $J_{12} \ll J_1$, J_2, (iii) all positive values of J_1, J_2 and J_{12} with $B_1 = B_2 \neq 0$. For all of them, we present the mean absolute percentage error (MAPE) of each variable prediction as a function of the number of observables N used to make the prediction. Therefore, each measurement is directly associated with a time step. Moreover, we adopt a time scale τ_0 where all variables can be written in terms of $\omega_0 = 1/\tau_0$ and/or $\hbar$.

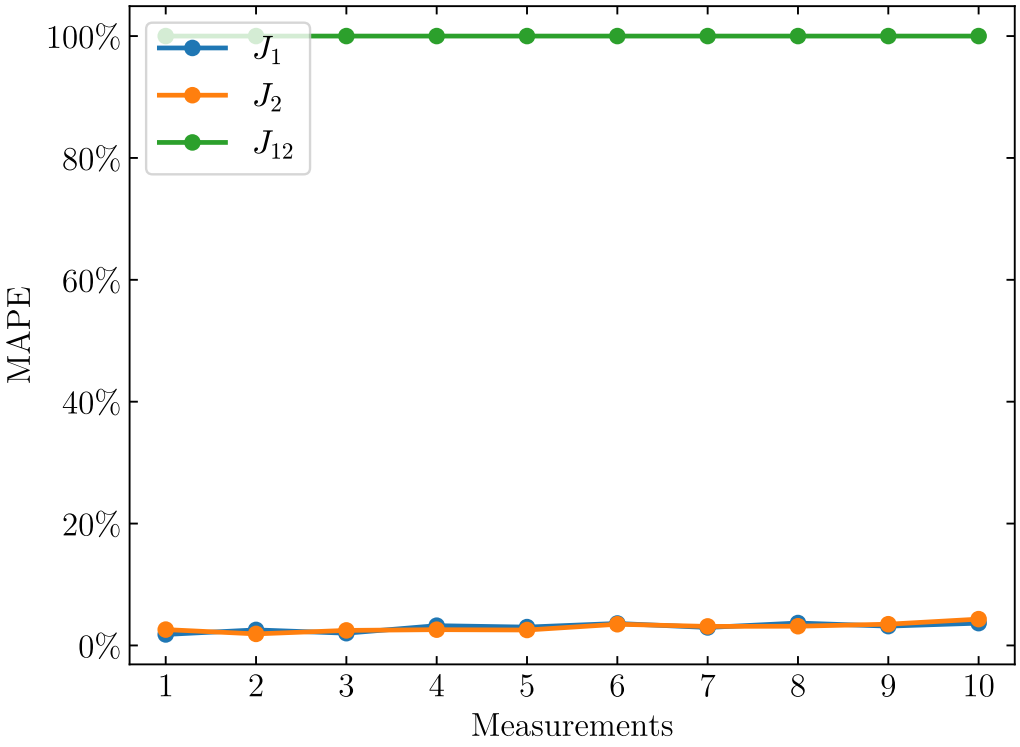

Figure 19 – MAPE for the prediction output parameters as function of the number of measurements considering random values of $J_1, J_2, J_{12} \in [-1, 1]$ and $B_1 = B_2 = 0$ for the input parameters to generate the test table, $J_1, J_2, J_{12} \in [-1, 1, 0.1]$ and $B_1 = B_2 = 0$ for the parameters to generate the training table, and with time intervals $t \in [0.2, 2, 0.2]$.

In Figure 19, we plot the MAPE as a function of the number of measures N for the predictions of the input parameters J_1, J_2, and J_{12}. We consider the time intervals for the measurements as $t \in [0.2, 2, 0.2]$ and use values of input parameters as J_1, J_2, $J_{12} \in [-1, 1]$,

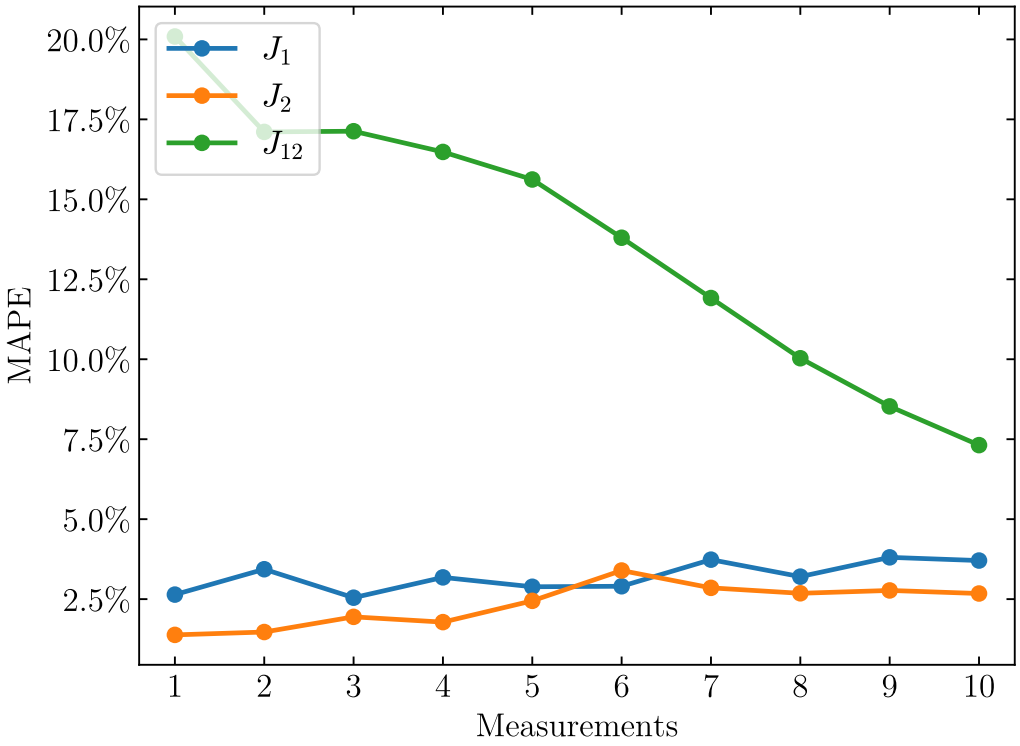

Figure 20 – MAPE for the prediction output parameters as function of the number of measurements considering random values of $J_1, J_2 \in [-1, 1]$, $J_{12} \in [0.1, 1]$, and $B_1 = B_2 = 0$ for the input parameters to generate the test table, $J_1, J_2 \in [-1, 1, 0.1]$, $J_{12} \in [0.1, 1, 0.1]$, and $B_1 = B_2 = 0$ for the parameters to generate the training table, and with time intervals as $t \in [0.2, 2, 0.2]$.

and $B_1 = B_2 = 0$ to generate 1000 elements in the test table. In this case, it was possible to predict values of J_1 and J_2 with error below 7% for all N. However, predicted values of J_{12} obtained an error of around 100%. This highly imprecise result is due to the fact that the functions of the observables $\langle \sigma_x^{(1,2)}(t) \rangle$ and $\langle \sigma_y^{(1,2)}(t) \rangle$ depend on the cosine values of J_{12}, as show in Equation 3.5. Therefore, it is impossible to determine the sign value of the parameter J_{12}, leading to calculated errors of 100%. On other hand, in Figure 20 we plot the MAPE using strictly positive values of J_{12}. We consider the same time intervals for the measurements, $t \in [0.2, 2, 0.2]$, and use values of input parameters as J_1, $J_2 \in [-1, 1]$, $J_{12} \in [0.1, 1]$, and $B_1 = B_2 = 0$ to generate 1000 elements in the test table. This time, the predicted values of J_1 and J_2 decrease the error to 5% for every number of measurements N and the MAPE for the prediction of J_{12} behaves like a decreasing curve as a function of the number of measurements. For $N = 1$ the error associated with J_{12} is around 20%, a value already considerably smaller than the previous case, while for $N = 10$ the MAPE of

the predicted values of J_{12} is now below 7%, closer to the previous values.

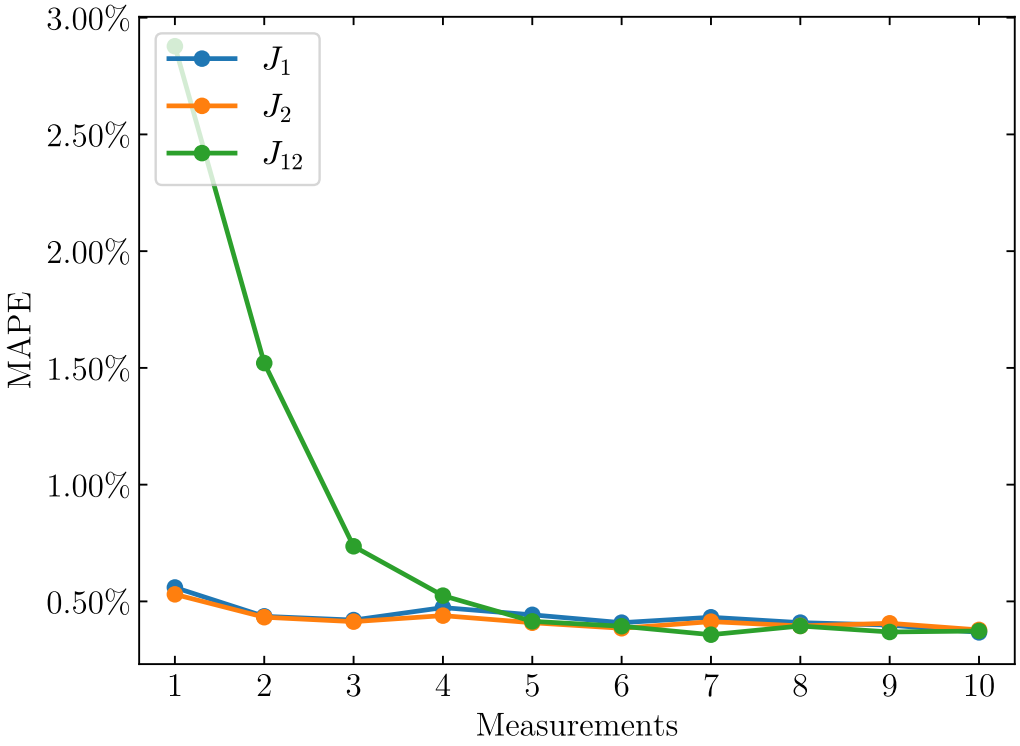

Figure 21 – MAPE for the prediction output parameters as function of the number of measurements considering random values of $J_1, J_2, J_{12} \in [1, 3]$ and $B_1 = B_2 = 0$ for the input parameters to generate the test table, $J_1, J_2, J_{12} \in [1, 3, 0.1]$ and $B_1 = B_2 = 0$ for the parameters to generate the training table, and with time intervals as $t \in [0.2, 2, 0.2]$.

It is important to note that the values of each parameter must be different from zero when using the MAPE measure because it is sensitive to values close to zero. When a parameter is equal to zero, it can cause the MAPE to become undefined or infinite, which can make it difficult to assess the accuracy of a model. Additionally, when the values of parameters are close to zero, even if not exactly equal to zero, small changes in the data can result in large changes in the MAPE. Therefore, having non-zero values for each parameter can help ensure that the MAPE is a stable and meaningful measure of error for the model. In this way, we will only use strictly positive values for each parameter and remove values close to zero. In Figure 21, we plot the MAPE of the input parameters as function of measurements considering the time intervals for the measurements as $t \in [0.2, 2, 0.2]$ and use values of input parameters $J_1, J_2, J_{12} \in [1, 3]$ and $B_1 = B_2 = 0$. As expected

according to the previous considered cases, using strictly positive values, the predictions of parameters J_1 and J_2 become more accurate, with MAPE around 0.5% for both parameters and all N. Moreover, the MAPE of J_{12} behaves like a decreasing curve as a function of the number of measurements with more accurate values as well. For $N = 1$ the associate error starts close to 3%, reaching an error closer of 0.5% at $N = 4$, and remains relatively constant with value of MAPE closer to 0.5% up to $N = 10$.

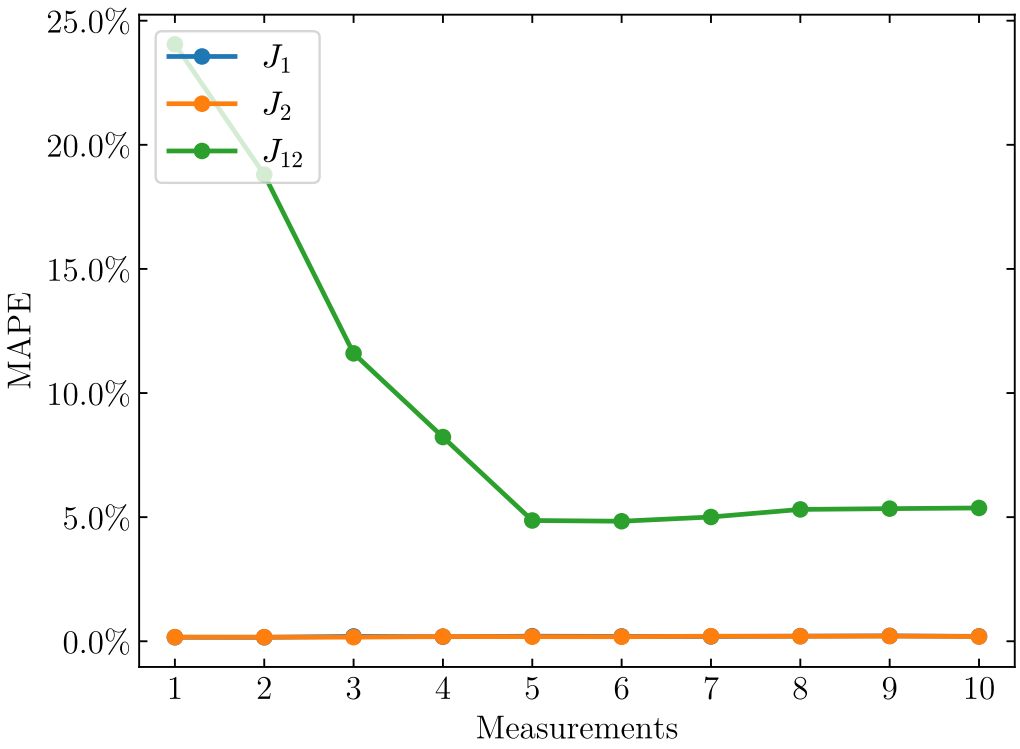

Figure 22 – MAPE for the prediction output parameters as function of the number of measurements considering random values of $J_1, J_2 \in [1, 3]$, $J_{12} \in [0.01, 0.03]$, and $B_1 = B_2 = 0$ for the input parameters to generate the test table, $J_1, J_2 \in [1, 3, 0.1]$, $J_{12} \in [0.01, 0.03, 0.001]$, and $B_1 = B_2 = 0$ for the parameters to generate the training table, and with short time intervals $t = [0.2, 2, 0.2]$, and long time intervals $T \in [20, 200, 20]$.

In the experiment carried out in reference (66) they perform a controlled two-qubit operation where the Hamiltonian (Equation 3.1) includes rapid single-qubit rotations, defined as $J_{12} << J_1, J_2$. Likewise, in Figure 22, we plot the MAPE of the input parameters as function of the number of measurements considering $J_1, J_2 \in [1, 3]$, $J_{12} \in [0.01, 0.03]$, and $B_1 = B_2 = 0$. However, we should note that very small values of J_{12} will not significantly change the values of the observables for the time interval used above. That is, for there to

be a notable change in the calculations of $\langle \sigma_x^{(1,2)}(t) \rangle$ and $\langle \sigma_y^{(1,2)}(t) \rangle$ as function of J_{12}, we must look again at the cosine arguments of Equation 3.5. Previously, using $J_{12} \in [1, 3]$ and $t \in [0.2, 2]$, we will reach the argument range $J_{12}t/2 \in [0.1, 3]$. Thus, for keeping the same argument interval using $J_{12} \in [0.01, 0.03]$, we consider shorter time intervals $t = [0.2, 2, 0.2]$, for the J_1 and J_2 parameters, and longer time intervals $T = [20, 200, 20]$ for the J_{12} parameter. In this case, the errors associated with the prediction of parameters J_1 and J_2 remained around 0.5% for all number of measurements N. The MAPE of J_{12} presented a decreasing behavior between $N = 1$ and $N = 5$, with errors of approximately 25% to 5%, respectively. And, for a number of measures greater than $N = 5$ the MAPE of J_{12} remained slightly constant.

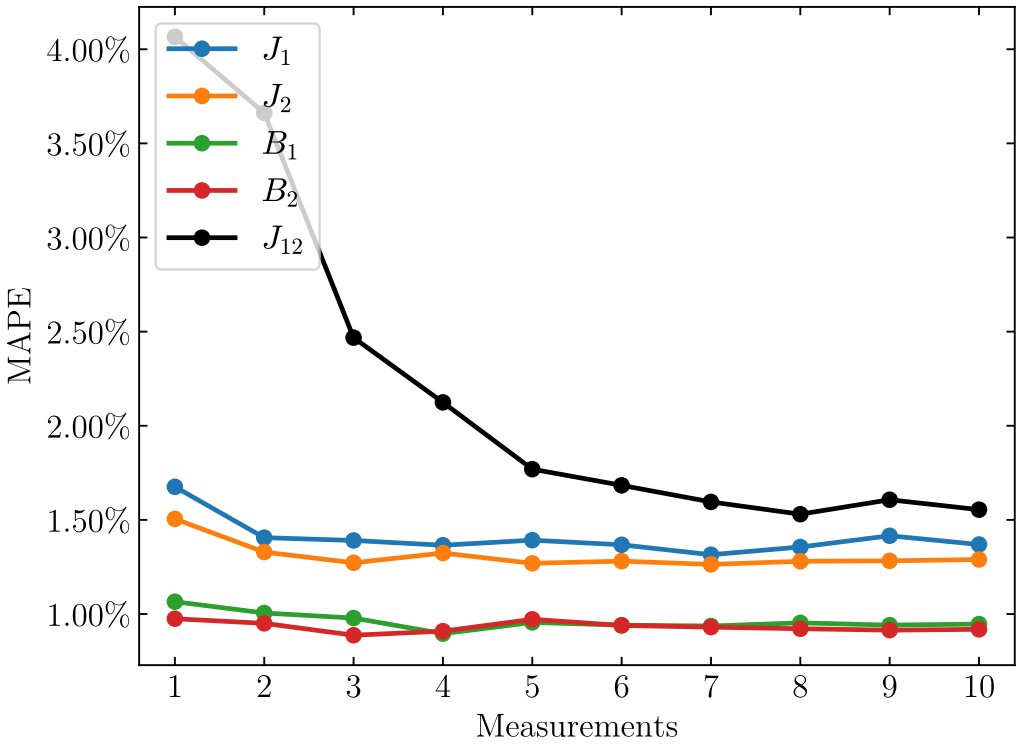

Figure 23 – MAPE for the prediction output parameters as function of the number of measurements considering random values of $J_1, J_2, B_1, B_2, J_{12} \in [1, 3]$ for the input parameters to generate the test table, $J_1, J_2, B_1, B_2, J_{12} \in [1, 3, 0.1]$ for the parameters to generate the training table, with time intervals as $t \in [0.2, 2, 0.2]$.

In Figure 23 and Figure 24 was add an external magnetic field $B_1, B_2 \neq 0$. For both cases, we consider the parameters $J_1, J_2, B_1, B_2 \in [1, 3]$ and a respective short time

interval $t = [0.2, 2, 0.2]$. In Figure 23, we plot the MAPE as function of the number of measurements with all parameters in the same range, that is, $J_{12} \in [1, 3]$ using the short time interval as well. Similar to the previous case (Figure 21) the predicted values of J_1 and J_2 present an associate error around 1.5% for all values of N, with the highest value of MAPE $\geq 1.5\%$ when only one measurement is considered. Also, the MAPE of J_{12} shows a decreasing behavior, with error values from approximately 4% for $N = 1$ to approximately 1.5% for $N = 10$. Furthermore, the prediction values of the magnetic fields B_1 and B_2 show a MAPE behavior constant. The associated error is approximately 1% for all number of measurements up to $N = 10$. In Figure 24, we analyze the case where $J_{12} \ll J_1, J_2, B_1, B_2$,

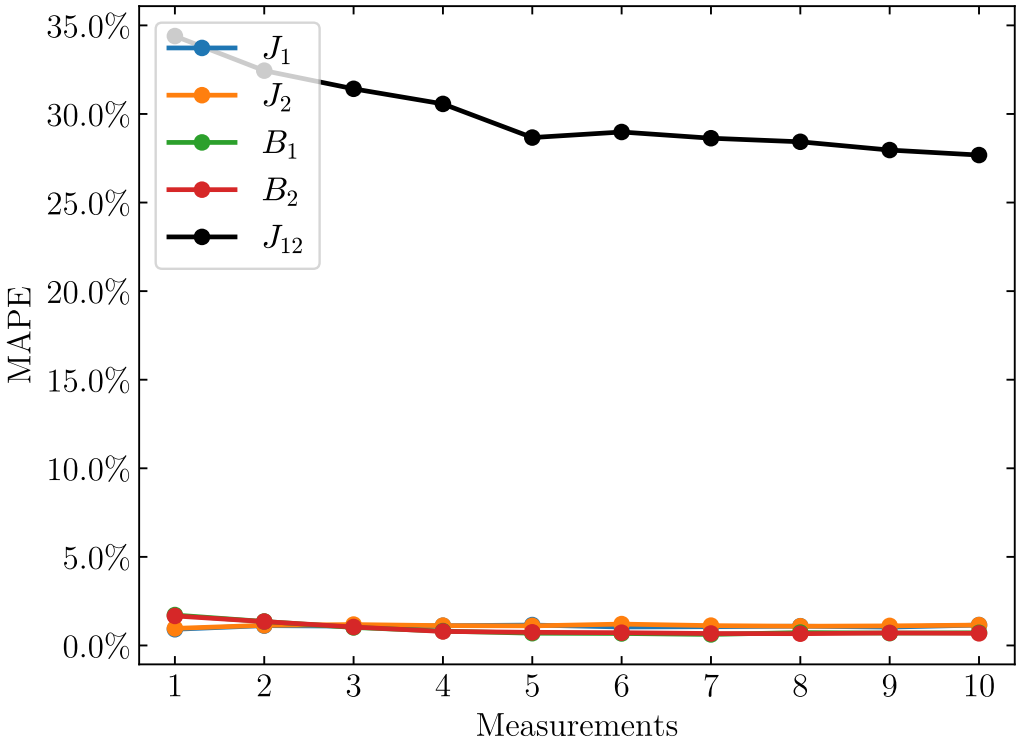

Figure 24 – MAPE for the prediction output parameters as function of the number of measurements considering random values of $J_1, J_2, B_1, B_2 \in [1, 3]$ and $J_{12} \in [0.01, 0.03]$ for the input parameters to generate the test table, $J_1, J_2, B_1, B_2 \in [1, 3, 0.1]$ and $J_{12} \in [0.01, 0.03, 0.01]$ for the parameters to generate the train table, and with short time intervals $t \in [0.2, 2, 0.2]$, and long time intervals $T \in [20, 200, 20]$.

considering $J_{12} \in [0.01, 0.03]$ with longer time intervals $T = [20, 200, 20]$. The predicted values of J_1, J_2, B_1, B_2 show good accuracy, with an error below 5%. More precisely, as emphasized in Figure 25, the MAPE of J_1 and J_2 shows a slightly increasing behavior for

the first values of N and remains approximately constant for $N \geq 3$. While the MAPE of B_1 and B_2 have a decreasing behavior, starting with an error of approximately 1.6% for $N = 1$ up to an error of approximately 0.7% for $N \geq 5$, changing to a constant behavior. Furthermore, the MAPE of J_{12} presents a slightly decreasing behavior but with higher error values than the previous ones (Figure 23). Here, the MAPE is approximately 35% for N=1 and approximately 27% for $N = 10$. Although it is possible to predict the values of J_{12} for the case $J_{12} \ll J_1, J_2$ with an accuracy of approximately 95%, the inclusion of a magnetic field makes it difficult to determine this parameter, reducing the accuracy to just below 70%, though the values of J_{12} are a hundred times smaller than the other parameters.

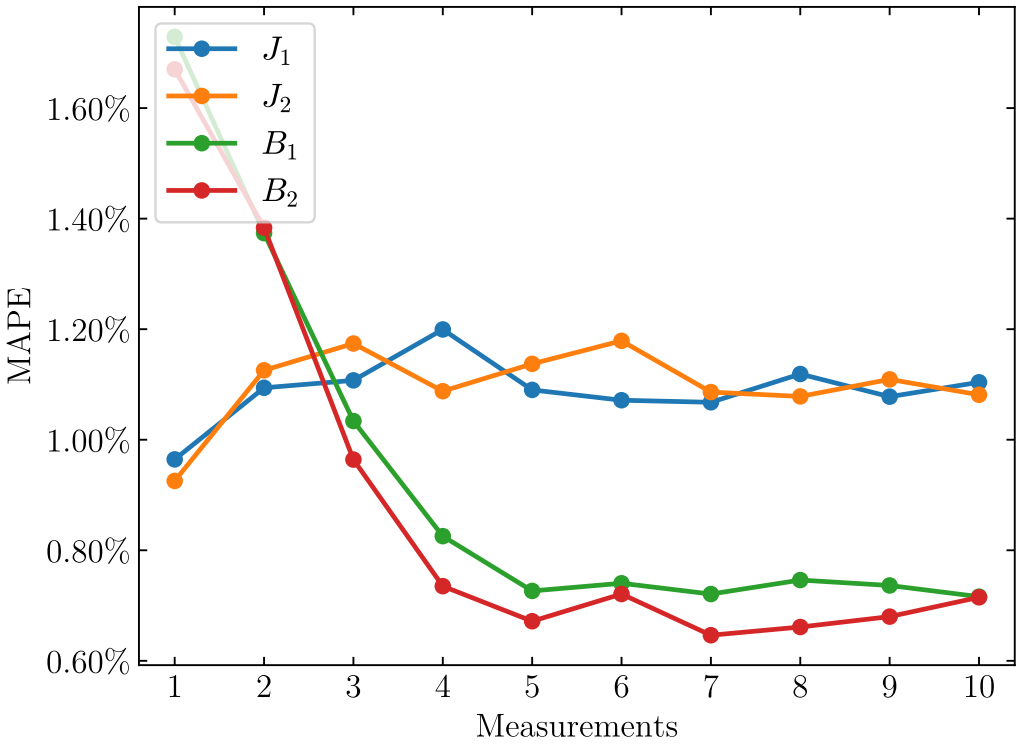

Figure 25 – MAPE for the prediction output parameters as function of the number of measurements considering random values of $J_1, J_2, B_1, B_2 \in [1, 3]$ for the input parameters to generate the test table, and with short time intervals $t \in [0.2, 2, 0.2]$.

3.5 Conclusion

In this chapter, we propose a protocol to determine the Hamiltonian parameters of a two-qubit system by means of the use of machine learning. Through this approach, we found the need to use strictly positive values for all parameters to reach a better accuracy. We studied three different cases: (i) $B_1 = B_2 = 0$ with J_1, J_2, and J_{12} in the same interval; (ii) $B_1 = B_2 = 0$ with $J_{12} \ll J_1, J_2$; (iii) $B_1, B_2 \neq 0$. For all cases it was possible to determine, with an error below 5%, the parameters J_1, J_2, B_1 and B_2 for training values in line with experimental values (66). However, the values of the interqubit interaction J_{12} presented several difficulties. In cases (i) and (ii) it was possible to identify J_{12}. Through the analytical solutions, we found that it is necessary the use of strictly positive values of J_{12} and we have to properly setup the interval and time step used. In case (iii), the presence of a magnetic field alters the determination of the values of J_{12}, more specifically, when J_{12} is much smaller than the other parameters. Despite a simplified analysis, it was possible to determine all the parameters initially propose, for up to ten measurements. Although we have not succeeded in all studied situation, we believe that this is an interesting approach and that new arrangements of values can be investigated in the future and provide a definitive determination of all physical parameters.

4 Distant interaction of quantum dot qubits

4.1 Introduction

The previous chapter presented a tool capable of determining the interqubit coupling in the Heisenberg-type Hamiltonian. Here, we model the QD qubits by a spin chain, where the charge interaction between neighbors is described by a Heisenberg Hamiltonian. In our model, the flow of information within the spin chain is carried by the SWAP gate (84), which is achieved by properly switching on and off the interaction between nearest neighbors. We assume that the interaction between qubits can be controlled by a time-dependent Gaussian pulse, whose parameters are optimized to implement the desired quantum gate. We are using a specific type of pulse, but this approach can be useful in real systems, *e.g*, if optimal control theory is employed to engineer the pulses (85, 86). When the system is free from noise, the fidelity related to the transport of quantum information in the spin chain is very robust. Very recently, effects of noise and other dissipation effects were investigated in a chain of QDs (87). They found that especially the charge noise has a great impact on the fidelity of the SWAP gate. Based on this work, we include a source of noise in each site of the spin chain via the Master equation approach to describe the decoherence throughout the quantum network. We also investigate the implementation of the CNOT gate, which is a very important two-qubit gate because it is fundamental to achieve universal quantum computing (88). The main difference between our study from related works is the investigation of the role of exchanging the order of CNOT and SWAP gates when noise is taken into account. We find that the order of the quantum gates application depends on the type of noise and the initial state. Furthermore, we probe the order of the quantum gates for a system containing four qubits and we verify that the order of different quantum gates can result in a relevant difference on the fidelity. The presented results bellow were published in Ref. (89).

4.2 Theoretical Model

4.2.1 Heisenberg spin chain model

We map the QD spin qubits in a spin chain containing N spin-1/2 particles coupled to each other by nearest-neighbor interactions, which are accordingly tuned through pulses capable of implementing quantum gates. Therefore, we have a time-dependent Hamiltonian

$$\mathcal{H}(t) = \sum_{n=1}^{N-1} H_{n,n+1}(t), \tag{4.1}$$

where the interaction between the n-th and the $(n+1)$-th particles is provided by

$$H_{n,n+1}(t) = \sum_{i,j} J_n^{i,j}(t)\sigma_n^i\sigma_{n+1}^j, \tag{4.2}$$

with

$$\begin{aligned}\sigma_n^i\sigma_{n+1}^j &= \mathbf{I}\otimes\ldots\otimes\mathbf{I}\otimes\sigma_n^i\otimes\sigma_{n+1}^j\otimes\mathbf{I}\otimes\ldots\otimes\mathbf{I}\\ &= \mathbf{I}^{\otimes n-1}\otimes\sigma^i\otimes\sigma^j\otimes\mathbf{I}^{\otimes N-n-1}\end{aligned} \tag{4.3}$$

and σ^i represents the respective Pauli operator with $i,j\in\{0,x,y,z\}$. We also intent to analyze noise effects on the performance of the quantum gates; thus, noise is included via the Lindblad quantum master equation (90)

$$\frac{\partial\rho}{\partial t} = -i[\mathcal{H},\rho] + \mathcal{D}(\rho), \tag{4.4}$$

where ρ is the density matrix and $\mathcal{D}$ is the so-called dissipator operator given by

$$\mathcal{D}(\rho) = \sum_{n,m}\left(L_{n,m}\rho L_{n,m}^\dagger - \frac{1}{2}\{L_{n,m}^\dagger L_{n,m},\rho\}\right). \tag{4.5}$$

We consider the qubits subjected to dephasing, amplitude damping, and depolarizing types of noise, where the corresponding Lindblad operators are given by: $L_{n,1} = L_n = \sqrt{\gamma}\sigma_n^z$, $L_{n,1} = L_n = \sqrt{\gamma}\sigma_n^-$, and $L_{n,m} = \sqrt{\gamma}\sigma_n^m$, for $m = x,y,z$. The decay rate γ is assumed to be constant for all qubits and $\sigma_n^k = \mathbf{I}^{\otimes n-1}\otimes\sigma^k\otimes\mathbf{I}^{\otimes N-n}$ for $k = \{x,y,z,-\}$. In the amplitude damping noise, the lowering operator is $\sigma^- = (\sigma^x - i\sigma^y)/2$, which describes the spontaneous emission process.

4.2.2 Implementation of SWAP and CNOT gates

In this section, we discuss two relevant gates for quantum computing, the SWAP and CNOT gates. The SWAP gate swaps the information between two qubits and it is useful to carry quantum information around the spin chain. On the other hand, the CNOT gate is fundamental to implement universal quantum computing. These gates are accomplished by a time-dependent coupling between nearest-neighbor in Equation 4.2, modeled by Gaussian pulses. Because these gates act only on two qubits, it is enough to search for pulses as follows

$$J_G^{i,j}(t) = A_G^{i,j} \exp\left\{-\frac{(t-\tau)^2}{W_G^{i,j}}\right\}, \tag{4.6}$$

where $A_G^{i,j}$ is the peak amplitude, $W_G^{i,j}$ is the width, τ is the center position of the pulse, and G = SWAP or CNOT.

Our first goal is to find $\mathcal{H}(t)$ for two qubits, such that the initial input state $|\psi_{in}\rangle$ evolves to the desired final output state $|\psi_{out}\rangle$. The time evolution results in $|\psi_{out}\rangle = U(t_0, T)|\psi_{in}\rangle$, where $U(t_0, T)$ is the unitary time evolution operator and t_0 (T) is the initial (final) evolution time. Moreover, the final output state must correspond to a desired state $|\psi_d\rangle = G|\psi_{in}\rangle$, where G is the quantum gate. To probe the equivalence between the evolved state $\rho_{out} = |\psi_{out}\rangle\langle\psi_{out}|$ and the desired state $\rho_d = |\psi_d\rangle\langle\psi_d|$, we employ the quantum fidelity

$$F(\rho_{out}, \rho_d) = \left(\mathrm{Tr}\sqrt{\sqrt{\rho_{out}}\rho_d\sqrt{\rho_{out}}}\right)^2, \tag{4.7}$$

which measures the proximity of two quantum states described by ρ_{out} and ρ_d. For a two-qubit system with an initial state as $|\psi_{in}\rangle = |q_1\rangle|q_2\rangle$, the SWAP gate acts in the following way

$$\mathrm{SWAP}\left(|q_1\rangle|q_2\rangle\right) = |q_2\rangle|q_1\rangle, \tag{4.8}$$

where $|q_1\rangle$ and $|q_2\rangle$ are arbitrary states. For two qubits, we find by inspection that the Hamiltonian able to implement the SWAP gate is

$$H_{\mathrm{SWAP}}(t) = J_{\mathrm{SWAP}}(t)\left(\sigma^x\sigma^x + \sigma^y\sigma^y + \sigma^z\sigma^z\right), \tag{4.9}$$

with the time-dependent pulse

$$J_{\mathrm{SWAP}}(t) = A_{\mathrm{SWAP}} \exp\left\{-\frac{(t-\tau)^2}{W_{\mathrm{SWAP}}}\right\}. \tag{4.10}$$

Similarly, the CNOT gate for the initial state $|\psi_{in}\rangle = |q_1\rangle|q_2\rangle$ acts as

$$\mathrm{CNOT}\left(|q_1\rangle|q_2\rangle\right) = |q_1\rangle|\tilde{q}_2\rangle, \tag{4.11}$$

where $|q_1\rangle$ is the control qubit and $|q_2\rangle$ is the target qubit. The CNOT gate flips the target qubit if and only if the control qubit is $|1\rangle$. By inspection, we find the Hamiltonian able to implement the CNOT gate, which is given by

$$\begin{aligned} H_{\mathrm{CNOT}}(t) = {} & J^1_{\mathrm{CNOT}}(t)\left(\mathbf{I}\sigma^x + \sigma^z\mathbf{I}\right) \\ & + J^2_{\mathrm{CNOT}}(t)\left(\sigma^z\sigma^x\right), \end{aligned} \tag{4.12}$$

with pulses,

$$J^k_{\mathrm{CNOT}}(t) = A^k_{\mathrm{CNOT}} \exp\left\{-\frac{(t-\tau)^2}{W^k_{\mathrm{CNOT}}}\right\}; \quad k = 1, 2. \tag{4.13}$$

The CNOT Hamiltonian in Equation 4.12 can be rewritten in a more familiar form, by rotating the first qubit in π around the $y-$direction, using the rotation operator

$$R_y(\theta) = e^{-i\frac{\theta}{2}\sigma_y} \tag{4.14}$$

Thus, the rotated initial state becomes $|\widetilde{\psi}_{in}\rangle = R_y(\pi)|q_1\rangle|q_2\rangle = \left(R_y(\pi)\otimes\mathbf{I}\right)|\psi_{in}\rangle$ and the rotated Hamiltonian is

$$\begin{aligned} \widetilde{H}_{\mathrm{CNOT}}(t) = {} & J^1_{\mathrm{CNOT}}(t)\left(\mathbf{I}\sigma^x - \sigma^x\mathbf{I}\right) \\ & + J^2_{\mathrm{CNOT}}(t)\sigma^x\sigma^x, \end{aligned} \tag{4.15}$$

The terms of both Hamiltonian's that appear in Equation 4.9 and Equation 4.12 were found by inspection of the mathematical structure of the gates and a ansatz. Since the SWAP and the CNOT gates are represented by hermitian matrices, it is possible to expand both gates in terms of the Pauli matrices. The basic idea is to assume that the Hamiltoninan (Equation 4.2) will have the same non-null elements to reach the respectively gate at the end of the temporal evolution.

4.3 Numerical Results

To numerically solve the time evolution Equation 4.4, we first need to define some parameters. We adopt the time scale τ_0, which coincides with the duration time of a single pulse, if not mentioned otherwise. In this case, the center position of the pulse is $\tau = \tau_0/2$ in Equation 4.10 and Equation 4.13. All other variables can be written in terms of $\omega_0 = 1/\tau_0$ and/or $\hbar$. Both SWAP and CNOT gates for a two-qubit system were found utilizing numerical optimization of the parameters related to the Gaussian pulses and the time evolution operator considering the unitary evolution, *i*.e., removing the dissipator term in Equation 4.4. We search for parameters that maximize the fidelity (Equation 4.7) between the desired state resulting from the action of the gate $G =$ SWAP or CNOT and the time-evolved state considering the set of initial states $\{|\psi_1\rangle = |00\rangle, |\psi_2\rangle = |01\rangle, |\psi_3\rangle = |10\rangle, |\psi_4\rangle = |11\rangle, |\psi_5\rangle\}$, where $|\psi_5\rangle = (|\psi_1\rangle + |\psi_2\rangle + |\psi_3\rangle + |\psi_4\rangle)/2$, which accounts for avoiding undesirable phase errors (85, 91, 92). Because the Hamiltonian of Equation 4.1 is time-dependent, we numerically employ a time discretization with step Δt to perform the time evolution through the following approximation

$$U(t, t + \Delta t) \approx \exp\{-iH(t + \Delta t)\Delta t\}, \tag{4.16}$$

which is successively applied from the initial time $t = 0$ up to the final time $t = T$. Through the Hamiltonians defined in Equation 4.9 and Equation 4.12, it is possible to find parameters for amplitudes and pulse widths described in Equation 4.10 and Equation 4.13, such that the evolution operator corresponds to the quantum gates, this is, $U(0, T)|\psi_{in}\rangle \to G|\psi_{in}\rangle$. The parameters numerically found are shown in Table 1 and the obtained fidelity exceeds 99.9999% at the final time, when noise is absent.

In Figure 26, we plot the fidelity $F(\rho_{out}(t), \rho_d)$ for the SWAP gate as a function of time using the density matrix $\rho_{out}(t)$ that is the solution of Equation 4.4 in the absence of noise for $\mathcal{H} = H_{\text{SWAP}}(t)$ and the density matrix ρ_d is given by the desired SWAP quantum gate according to Equation 4.8, by considering three different initial states of the first qubit $|q_1\rangle = |0\rangle$, $|q_1\rangle = |1\rangle$, and $|q_1\rangle = |+\rangle = (|0\rangle + |1\rangle)/\sqrt{2}$, and keeping fixed the second qubit as $|q_2\rangle = |0\rangle$. By using the optimized parameters found for the Gaussian pulse,

which is shown as a grey dashed curve in Figure 26, it is possible to see that for all three initial input states the final fidelity approaches one with an error of $10^{-4}\%$ at the final time. Moreover, the blue solid curve in Figure 26 shows the time evolution of the initial state $|10\rangle$ that must reach the state $|01\rangle$ at the end of the pulse evolution; therefore, the fidelity is 0 for $t = 0$, it oscillates when the Gaussian pulse is different from zero, and it reaches a value very close to 1 after the Gaussian pulse approaches zero. On the other hand, the initial state $|00\rangle$ is an eigenstate of the time-independent part of $H_{\mathrm{SWAP}}(t)$, thus the fidelity is always one throughout the whole time evolution as shown by the orange solid curve in Figure 26. The initial state $|+0\rangle$ must reaches $|0+\rangle$ at the end of the time evolution, thus the fidelity shown by the green solid curve in Figure 26 is initially 1/2, it oscillates when the pulse is different from zero, and it reaches a value very close to 1 when the pulse approaches zero. Similarly, in Figure 27, we plot the fidelity for the CNOT gate and the respective Gaussian pulses (grey dashed curves) as a function of time. Using the same states employed in the SWAP case, $|10\rangle$, $|00\rangle$, and $|+0\rangle$. The fidelity for these initial states starts at 0, 1, and 1/2, respectively. At the final time of evolution, the fidelity for all initial states exceeds 0.999999. It is possible to observe the variation of the fidelity as a function of time when the Gaussian pulses are different from zero as shown by the blue, orange, and green solid curves in Figure 27.

A_{SWAP}	9.36309696 $\hbar\omega_0$
W_{SWAP}	0.020165 τ_0^2
A^1_{CNOT}	9.33360747 $\hbar\omega_0$
W^1_{CNOT}	0.02029270 τ_0^2
A^2_{CNOT}	3.11530553 $\hbar\omega_0$
W^2_{CNOT}	0.02023955 τ_0^2

Table 1 – Amplitude and width values for the pulses of SWAP and CNOT gates.

4.3.1 Noise effects

This section aims at understanding the effects of noise during the time evolution of the Gaussian pulses that implement the quantum gates. By numerically solving Equation 4.4, it is possible to calculate the fidelity at the final time for different decay rates. We also probe these effects by analyzing the final time dependence of the fidelity. To do so, we

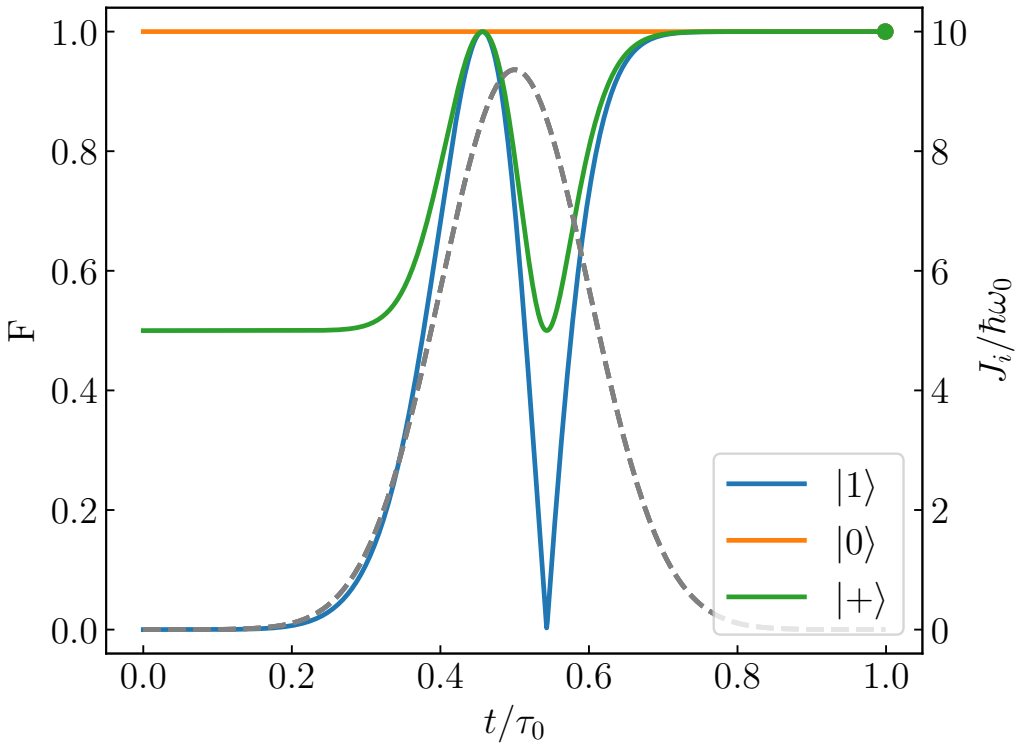

Figure 26 – Fidelity $F(\rho_{out}(t), \rho_d)$ as a function of time t/τ_0 (left axis), where $\rho_{out}(t)$ is the solution of Equation 4.4 without considering noise and ρ_d is the desired density matrix obtained from Equation 4.8. We consider the first qubit $|q_1\rangle = |1\rangle$ (blue solid curve), $|0\rangle$ (orange solid curve), and $|+\rangle$ (green solid curve) and the second qubit fixed as $|q_2\rangle = |0\rangle$. The Gaussian pulse J_{SWAP} as a function of time t/τ_0 is also shown (gray dashed curve).

must resize the single pulse duration, center, and amplitude such that the fidelity would give one in the absence of noise at the final time. Thus, the parameters in Table 1 must be replaced by $A \to A/\alpha$ and $W \to W\alpha^2$, where the single pulse duration is $T = \alpha\tau_0$ and the center position is $\tau = \alpha\tau_0/2$. In Figure 28, we plot the fidelity F for different final times, considering the dephasing noise, which is described by the Lindblad operator $L_n = \sqrt{\gamma}\sigma_n^z$. Also, we consider the implementation of SWAP and CNOT gates on the initial state $|q_1\rangle|q_2\rangle = |+\rangle|0\rangle$, whose fidelity is given by solid and dashed curves, respectively. When the final time is $T = \tau_0$, the fidelity for the SWAP (CNOT) decays to 0.99987 (0.9996), 0.9987 (0.996), and 0.987 (0.967) for $\gamma\tau_0 = 0.001$, 0.001, and 0.1, respectively. As expected, the fidelity also decreases as the pulse duration increases. For $\gamma\tau_0 = 0.1$, the fidelity converges to approximately $F = 0.6$ ($F = 0.5$) for the SWAP (CNOT) gate in the limit of long final time. This behavior is related to the reaching of the stationary states for both gates.

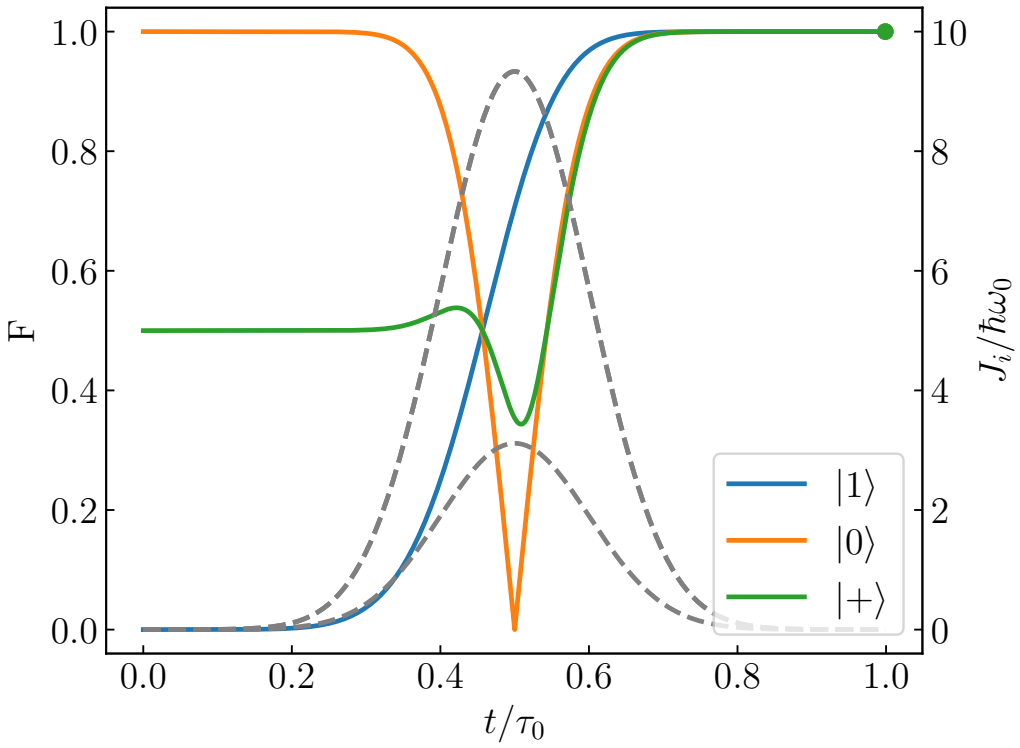

Figure 27 – Fidelity $F(\rho_{out}(t), \rho_d)$ as a function of time t/τ_0 (left axis), where $\rho_{out}(t)$ is the solution of Equation 4.4 without considering noise and ρ_d is the desired density matrix obtained from Equation 4.11. We consider the first qubit $|q_1\rangle = |1\rangle$ (blue solid curve), $|0\rangle$ (orange solid curve), and $|+\rangle$ (green solid curve) and the second qubit fixed as $|q_2\rangle = |0\rangle$. Gaussian pulses J^1_{CNOT} (higher amplitude) and J^2_{CNOT} as a function of time t/τ_0 (gray dashed curves).

Similarly, in Figure 29 we plot the fidelity F as a function of the final time T/τ_0, but now for the amplitude damping noise, where the Lindblad operator is $L_n = \sqrt{\gamma}\sigma_n^-$, considering the same initial state $|q_1\rangle|q_2\rangle = |+\rangle|0\rangle$ employed above. The fidelity decays as the final time increases, however the SWAP gate experiences higher robustness when compared to the CNOT gate. For example, the fidelity converges to approximately $F = 0.7$ for the SWAP gate, while it goes to zero for the CNOT gate when $T = 100\tau_0$ and $\gamma\tau_0 = 0.1$.

4.3.2 N-qubit system

Here, we explore the connection between different qubits through a sequence of gates that transports the quantum information across the chain. The general state for the N-qubit system can be written as $|\psi\rangle = |q_1\rangle|q_2\rangle \ldots |q_{N-1}\rangle|q_N\rangle$. We use the first two qubits $|q_1\rangle|q_2\rangle$ as the input state and all other qubits $|q_3\rangle \ldots |q_{N-2}\rangle$ as auxiliary qubits. Therefore,

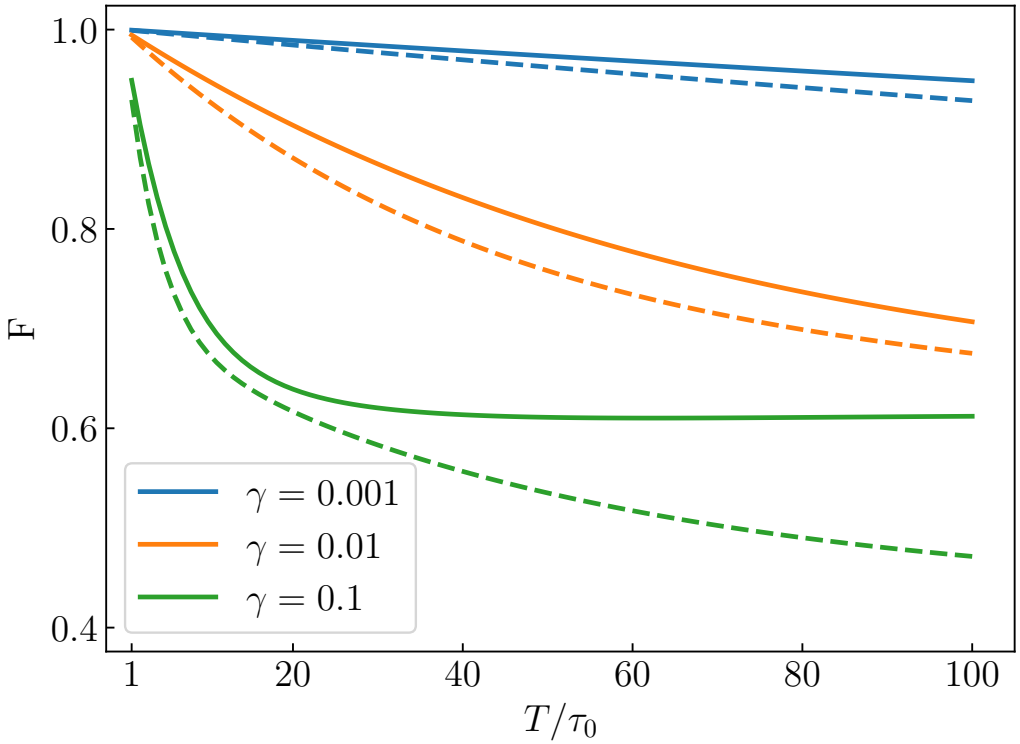

Figure 28 – Fidelity $F(\rho_{out}(t), \rho_d)$ as a function of final time T/τ_0, where $\rho_{out}(t)$ is the solution of Equation 4.4 and ρ_d is the desired density matrix obtained either from Equation 4.8 or Equation 4.11. Also, we consider different decay rates $\gamma\tau_0 = 0.001$, 0.01, and 0.1 for the dephasing error. The solid curves correspond to the SWAP gate and the dashed curves correspond to the CNOT gate. The input state is $|q_1\rangle = |+\rangle$ and $|q_2\rangle = |0\rangle$ for both quantum gates.

the two-qubit gate implementation will result in an output state that will be at the end of the chain $|q_{N-1}\rangle|q_N\rangle$. When the dynamics is unitary, we can write $|\phi_{in}\rangle$ as the input state and $|\phi_{out}\rangle$ as the output state, which are explicitly given by

$$|\psi_{in}\rangle = |\phi_{in}\rangle|\phi_0^{N-2}\rangle, \tag{4.17}$$

and

$$|\psi_{out}\rangle = |\phi_0^{N-2}\rangle|\phi_{out}\rangle, \tag{4.18}$$

where $|\phi_0^{N-2}\rangle = |0\rangle|0\rangle \ldots |0\rangle|0\rangle$. First, we spatially arrange the qubits in a 1D spin chain, which is a possible design of QDs (93). A two-qubit gate is implemented over the state $|\phi_{in}\rangle = |q_1\rangle|q_2\rangle$, followed by a sequence of SWAP gates that propagates the information from one side to the other of the 1D chain of qubits. To perform this sequence of gates, we use the final time for each pulse as $T = \tau_0$ and the center of the n-th pulse obeys the

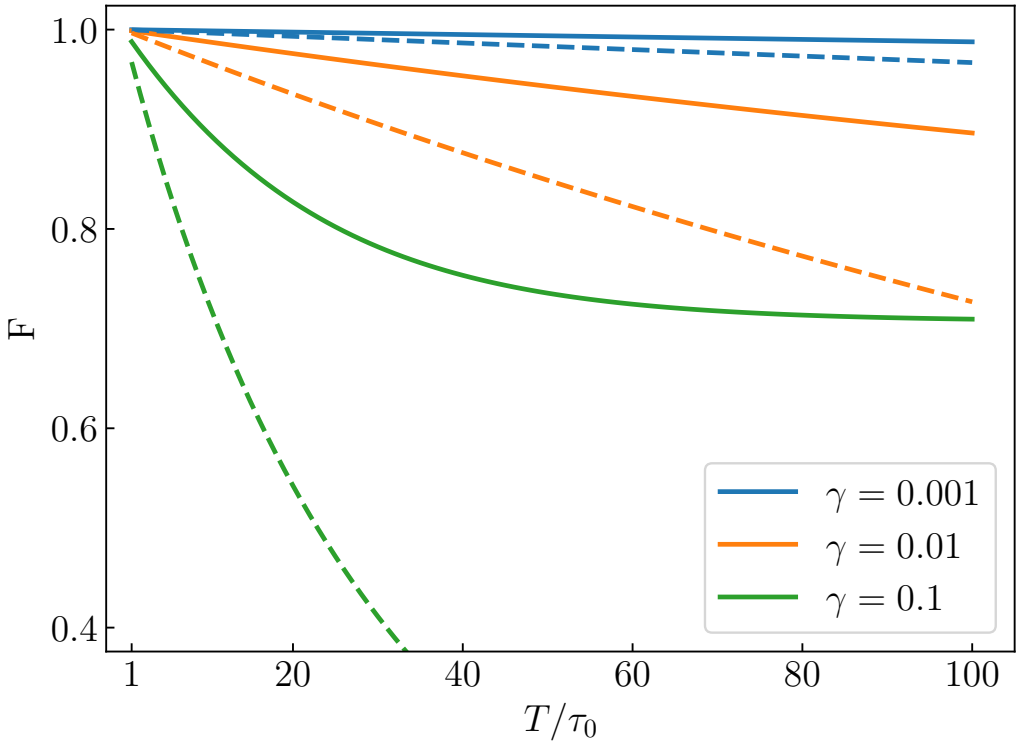

Figure 29 – Fidelity $F(\rho_{out}(t), \rho_d)$ as a function of final time T/τ_0, where $\rho_{out}(t)$ is the solution of Equation 4.4 and ρ_d is the desired density matrix obtained either from Equation 4.8 or Equation 4.11. Also, we consider different decay rates $\gamma\tau_0 = 0.001$, 0.01, and 0.1 for the amplitude-damping error. The input state is $|q_1\rangle = |+\rangle$ and $|q_2\rangle = |0\rangle$ for both quantum gates.

following relation: $\tau_n/\tau_0 = n - 1/2$. To exemplify this arrangement of qubits, we consider three qubits in a 1D spin chain, as represented by the top panel of Figure 30. In this situation, a CNOT gate is implemented between qubits $|q_1\rangle$ and $|q_2\rangle$ at the final time τ_1 and this information is propagated forward by using a SWAP gate between qubits $|q_2\rangle$ and $|q_3\rangle$, which occurs at the final time τ_2, as depicted in the bottom panel of Figure 30. Finally, a SWAP gate between qubits $|q_1\rangle$ and $|q_2\rangle$ at the final time τ_3, yields the two-qubit output state mapped onto qubits $|\phi_{out}\rangle = |q_2\rangle|q_3\rangle$. If one more qubit is added to the three-qubit system, as depicted in Figure 31, it is necessary to include two more SWAP gates between the pairs of qubits $|q_3\rangle$, $|q_4\rangle$ and $|q_2\rangle$, $|q_3\rangle$ to propagate the information to the end of the chain. In conclusion, for N qubits arranged in a 1D spin chain, $2(N-2)$ SWAP gates are needed to forward the information from an initial state to the output state $|\phi_{out}\rangle = |q_{N-1}\rangle|q_N\rangle$, when the dynamics is unitary. Of course, when noise is taken into account, Equation 4.17 and Equation 4.18 must be replaced by the respective density

matrix for N-qubits ρ_{in}^{N} and ρ_{out}^{N}. In this case, the fidelity is evaluated by tracing out all auxiliary qubits, thus $\rho_{out} = \mathrm{Tr}_{[1,\ldots,N-2]}\{\rho_{out}^{N}\}$ in Equation 4.7. In Figure 32, we plot the

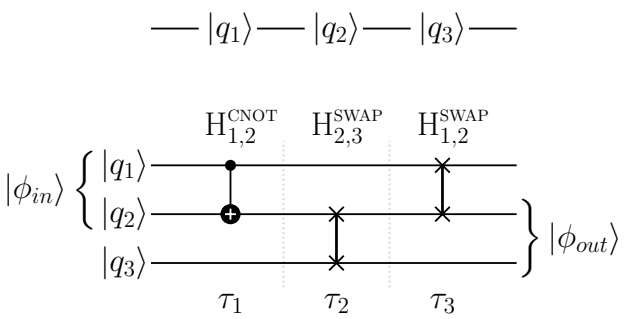

Figure 30 – (top panel) Three qubits are arranged in a 1D spin chain. (bottom panel) Quantum circuit where a CNOT gate is applied to the initial two qubits, $|\phi_{in}\rangle = |q_1\rangle|q_2\rangle$, which occurs at the final time τ_1, followed by two SWAP gates applied in the qubits $|q_2\rangle$ and $|q_3\rangle$ at the final time τ_2 and qubits $|q_1\rangle$ and $|q_2\rangle$ at the final time τ_3. The output state is encoded in the two last qubits of the 1D chain $|\phi_{out}\rangle = |q_2\rangle|q_3\rangle$.

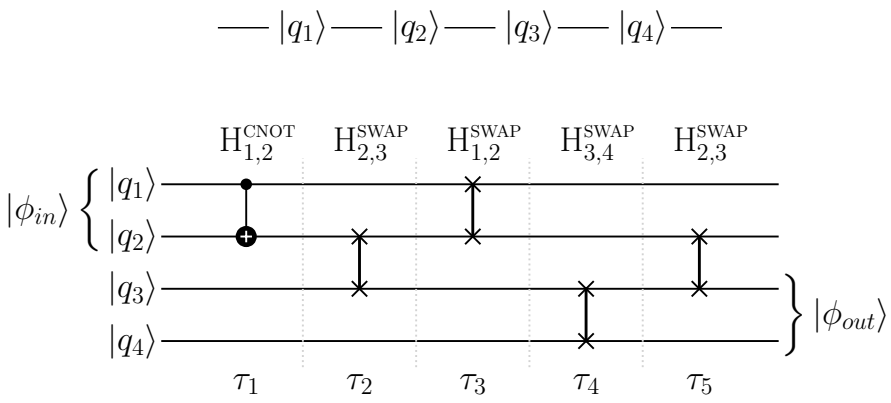

Figure 31 – (top panel) Four qubits are arranged in a 1D spin chain. (bottom panel) Quantum circuit where a CNOT gate is applied to the initial two qubits, $|\phi_{in}\rangle = |q_1\rangle|q_2\rangle$, followed by SWAP gates that shuttle the quantum information to the last two qubits in the chain, resulting in the output state $|\phi_{out}\rangle = |q_3\rangle|q_4\rangle$. In this case, the k-th pulse occurs at the final time τ_k, where $k = 1, \ldots, 5$.

fidelity F as a function of the number of qubits N for different decay rates considering the dephasing noise. The qubits are arranged in a 1D spin chain (see Figure 30) and the initial state is $|q_1\rangle = |+\rangle$ and $|q_i\rangle = |0\rangle$ for $1 < i \leq N$. We also analyze the cases where a CNOT gate comes first and it is followed by $2(N-2)$ SWAP gates and the opposite order, *i.* e., $2(N-2)$ SWAP gates followed by a CNOT gate. For both cases, the total

time T is proportional to the number of gates and consequently to the number of qubits. When the dynamics is unitary, the fidelity always approaches one (results not shown here). On the other hand, the fidelity decreases with the increasing of the number of qubits for $\gamma\tau_0 = 0.001$, as shown in Figure 32. As expected, the fidelity decay is stronger for $\gamma\tau_0 = 0.01$ and $\gamma\tau_0 = 0.1$. Moreover, the fidelity is different if the application of a CNOT gate occurs at the beginning (solid curves) or at the end (dashed curves) of the N-qubits 1D chain. This result is interesting because it shows that order of gates plays an important role when the information is transmitted along the chain when noise is present. One hypothesis for this behavior would be because entanglement is created at the beginning of the chain and we have more difficulty maintaining it throughout the chain propagation.

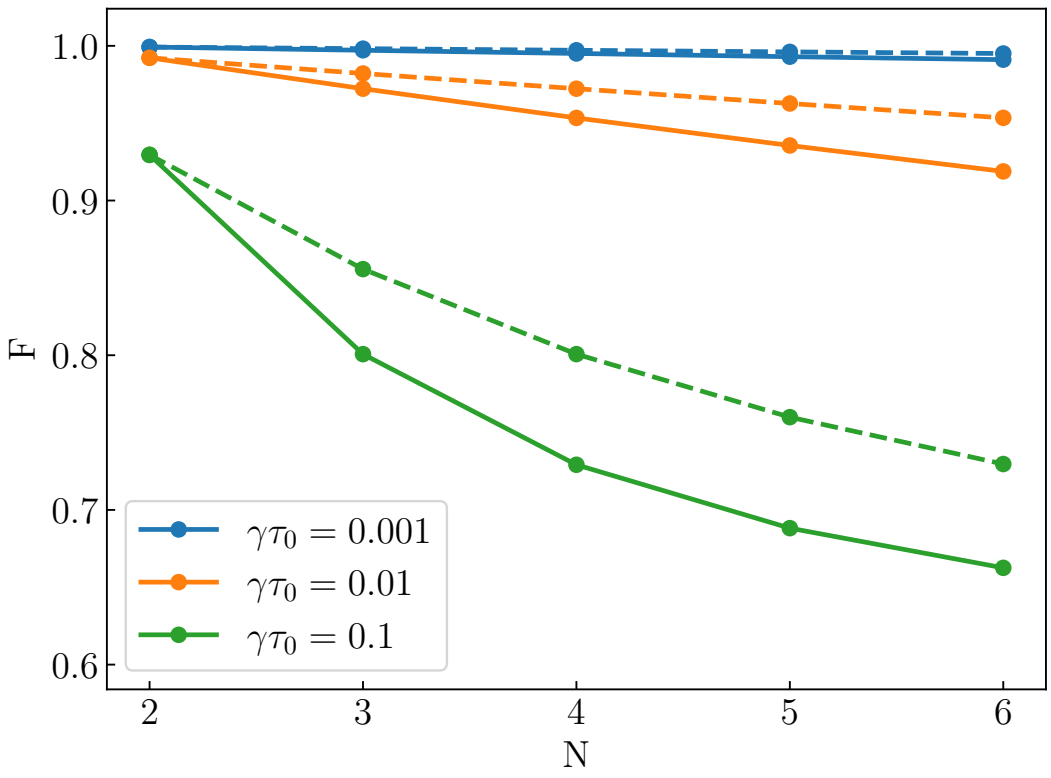

Figure 32 – Fidelity $F(\ \mathrm{Tr}_{[1,\ldots,N-2]}\{\rho_{out}(t)\}, \rho_d)$ as a function of the number of qubits N, where $\rho_{out}(t)$ is the solution of Equation 4.4 and ρ_d is the desired density matrix obtained from Equation 4.11. Also, we consider different decay rates $\gamma\tau_0 = 0.001$, 0.01, and 0.1 for the dephasing error. The solid curves correspond to an initial CNOT gate followed by $2(N-2)$ SWAP gates and the dashed curves correspond to $2(N-2)$ SWAP gates followed by a final CNOT gate considering the qubits arranged in a 1D spin chain. The input state is given by $|q_1\rangle = |+\rangle$ with all other qubits $|q_i\rangle = |0\rangle$ for $1 < i \leq N$.

For N even, the N-qubit system can also be spatially arranged in a 2D square spin chain of qubits. For example, considering four qubits as depicted in Figure 33, we have the input state $|\phi_{in}\rangle = |q_1\rangle|q_2\rangle$, about which a CNOT gate is applied at the final time τ_1. Two SWAP gates are applied between qubits $|q_2\rangle$ and $|q_4\rangle$ at time τ_2 and between qubits $|q_1\rangle$ and $|q_3\rangle$ at time τ_3. Because these SWAP gates occur between different qubits, they can be simultaneously implemented; thus, we can have $\tau_3 = \tau_2$. The two-qubit output is provided by $|\phi_{out}\rangle = |q_3\rangle|q_4\rangle$. For a general case of a 2D square spin chain of N qubits, $N/2$ SWAP gates are needed to forward the information to $|\phi_{out}\rangle = |q_{N-1}\rangle|q_N\rangle$. Therefore, the 2D square spin chain configuration of qubits requires a smaller number of gates to propagate the information and consequently a smaller total time. In Figure 34, we plot the fidelity F

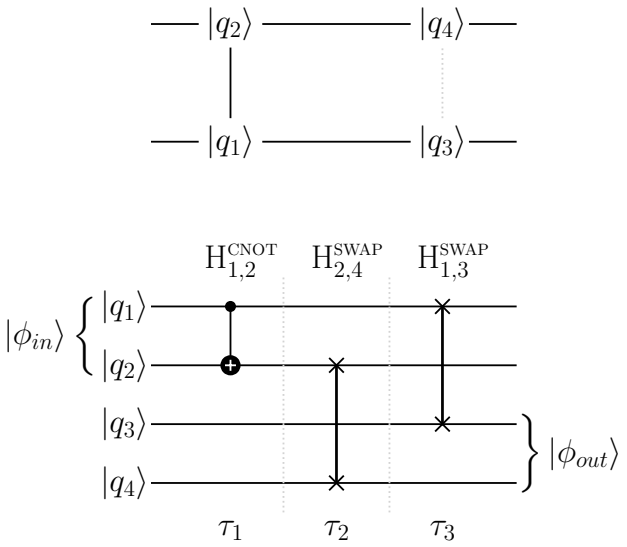

Figure 33 – (top panel) Four qubits are arranged in a 2D square spin chain. (bottom panel) The quantum circuit where a CNOT gate is applied between the qubits $|q_1\rangle$ and $|q_2\rangle$ in time τ_1, followed by a SWAP gate applied between the qubits $|q_3\rangle$ and $|q_4\rangle$ in the final time τ_2. The last SWAP gate is applied between qubits $|q_1\rangle$ and $|q_3\rangle$ in the final time τ_3.

as a function of the number of qubits N for different decay rates and the dephasing noise. The qubits are arranged in the 2D square spin chain and the initial state is also $|q_1\rangle = |+\rangle$ and $|q_i\rangle = |0\rangle$ for $1 < i \leq N$. Likewise, we consider the situation where a CNOT gate is followed by $N/2$ SWAP gates (solid curves) and vice-versa (dashed curves). Because the SWAP gates are independent in pairs, we can set the time evolution for each pair of pulses

respecting the following relation $\tau_{k+1} = \tau_k$. Therefore, the total time for propagating the information through the SWAP gates is proportional to $N/2$. Because of this fact, the fidelity for propagating the quantum information over 12 qubits is equivalent to only 6 qubits in a 1D spin chain system as one can see by comparing the results in Figure 32 and Figure 34. This result demonstrates that the 2D arrangement is preferable to transport the CNOT gate over more qubits. Similarly, in Figure 35, we plot the fidelity as a function

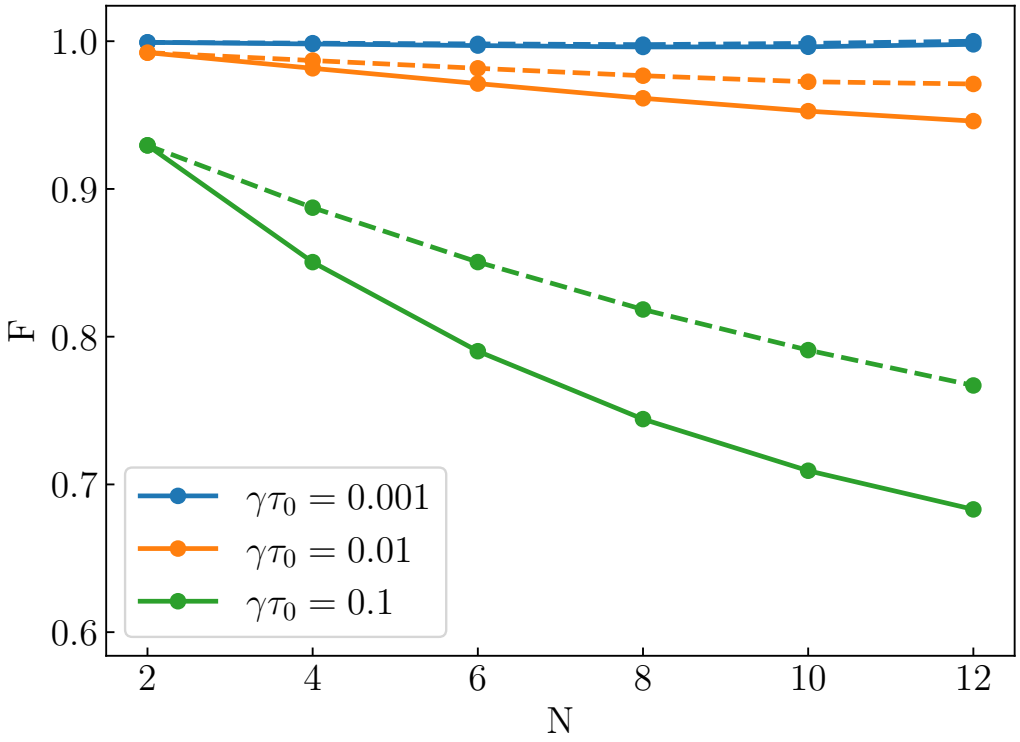

Figure 34 – Fidelity $F(\ \mathrm{Tr}_{[1,\ldots,N-2]}\{\rho_{out}(t)\}, \rho_d)$ as a function of the number of qubits N, where $\rho_{out}(t)$ is the solution of Equation 4.4 and ρ_d is the desired density matrix obtained from Equation 4.11. Also, we consider different decay rates $\gamma\tau_0 = 0.001$, 0.01, and 0.1 for the dephasing error. The solid curves correspond to an initial CNOT gate followed by $N/2$ SWAP gates and the dashed curves correspond to $N/2$ SWAP gates followed by a final CNOT gate, considering a 2D square spin chain of qubits. The input state is given by $|q_1\rangle = |+\rangle$ with all other qubits $|q_i\rangle = |0\rangle$ for $1 < i \leq N$.

of the number of qubits using the 2D square spin chain for the amplitude damping noise and the same initial state, *i.* e. , $|q_1\rangle = |+\rangle$ and $|q_i\rangle = |0\rangle$ for $1 < i \leq N$. For small values of the decay rate, $\gamma\tau_0 = 0.001$ and 0.01, the fidelity is more robust against noise and the fidelity diminishes less than 5% for $N = 12$. For $\gamma\tau_0 = 0.1$, the fidelity presents a linear behavior and the lowest value is approximately $F = 0.76$. By comparing the results shown

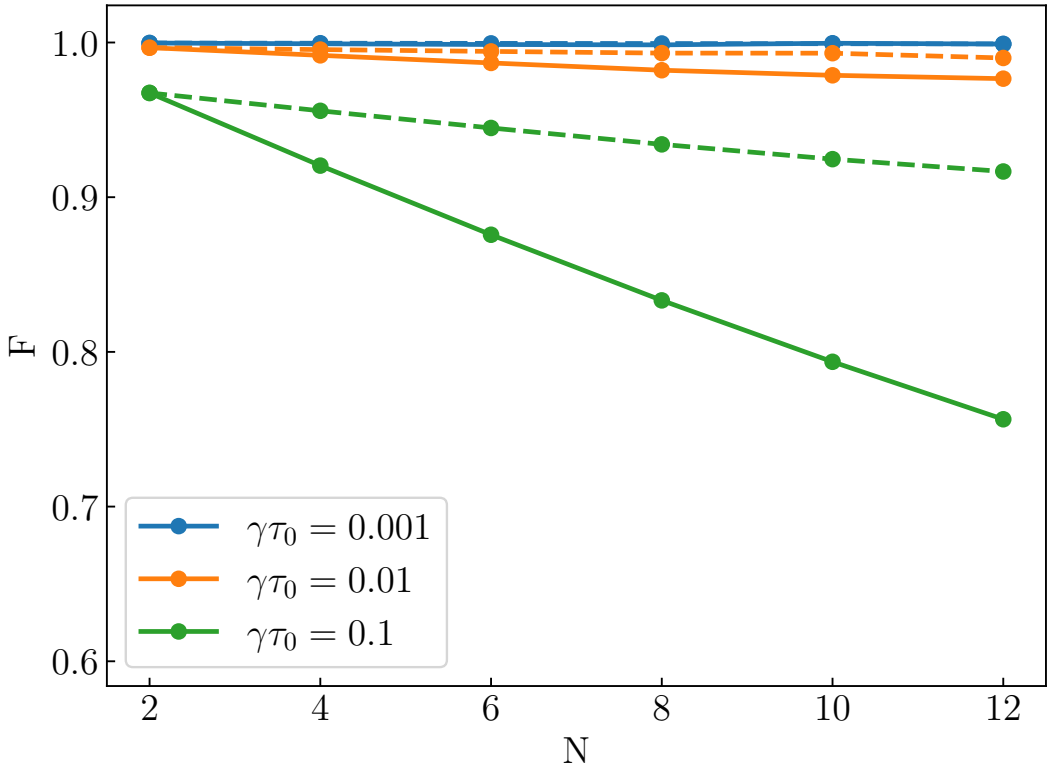

Figure 35 – Fidelity F as a function of the number of qubits N for different decay rates $\gamma\tau_0 = 0.001$, 0.01 and 0.1, considering the amplitude-damping error. The solid curves correspond to an initial CNOT gate followed by $N/2$ SWAP gates and the dashed curves correspond to $N/2$ SWAP gates followed by a final CNOT gate, considering a 2D square spin chain of qubits. The input state is given by $|q_1\rangle = |+\rangle$ with all other qubits $|q_i\rangle = |0\rangle$ for $1 < i \leq N$.

in Figure 34 and Figure 35, we verify that the fidelity is higher when the CNOT gate is applied at the final of the chain for both types of errors.

4.3.3 Initial states

In this section, we intend to explore the initial state influence on the fidelity when the order of quantum gates is distinct and noise is taken into account. To accomplish such a task, we choose the initial input state as $|\phi_{in}(\theta,\varphi)\rangle = |+\rangle|q_2(\theta,\varphi)\rangle$, where

$$|q_2(\theta,\varphi)\rangle = \cos(\theta/2)|0\rangle + e^{i\varphi}\sin(\theta/2)|1\rangle, \tag{4.19}$$

with $\theta \in [0,\pi]$ and $\varphi \in [0,2\pi)$. To be able to evaluate the fidelity for several initial states, we choose a 2D square spin chain composed of four qubits, as depicted in Figure 33. Furthermore, we calculate the difference in the fidelity evaluated for a CNOT gate followed

by two SWAP gates and vice-versa; thus, $\Delta F = F_{\text{1CNOT–2SWAP}} - F_{\text{2SWAP–1CNOT}}$. In Figure 36 we plot ΔF as a function of θ and φ in a colormap for decay rate $\gamma\tau_0 = 0.1$ considering the amplitude-damping noise. One can see that the fidelity variation ΔF is predominantly less than zero, which implies that the 2SWAP-1CNOT order provides higher fidelity than the one obtained for the 1CNOT-2SWAP order. The solid white curve indicates the angles where $\Delta F = 0$, which can be approximated by the following relation $\theta(\varphi) \approx a\cos(2\varphi) + b$. In Figure 37, we plot ΔF as a function of θ and φ, considering the dephasing noise. One

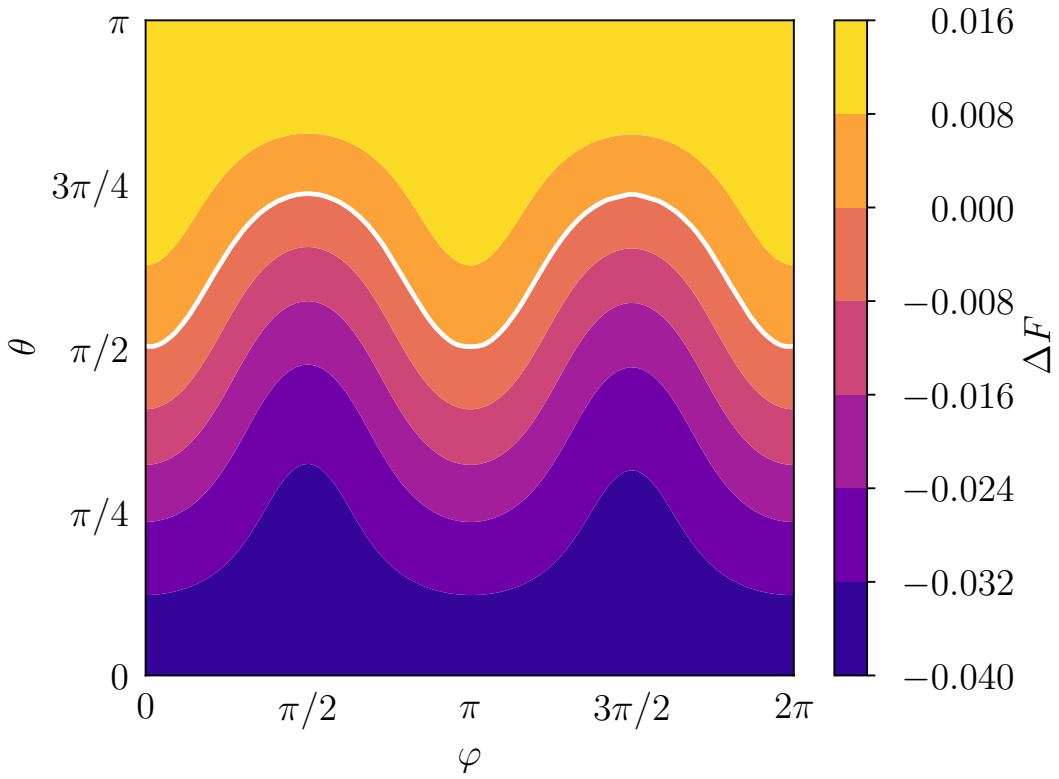

Figure 36 – Fidelity difference considering a CNOT followed by two SWAP gates and vice-versa as a function of θ and φ, which are related to the initial state $|\phi_{in}(\theta,\varphi)\rangle = |+\rangle|q_2(\theta,\varphi)\rangle$ for decay rate $\gamma\tau_0 = 0.1$ and the amplitude-damping error. In this case, four qubits are spatially arranged in a 2D square spin chain. The white line represents the values where $\Delta F = 0$.

can see in Figure 37 that the fidelity variation depends only on θ. Also, the solid white curves indicate where $\Delta F = 0$ and define a small region between approximately $\theta = \pi/2$ and $3\pi/5$ where the value of the difference ΔF is positive. For the dephasing noise, we verify that the order 2SWAP-1CNOT provides a higher fidelity for the majority of initial states when compared to the order 1CNOT-2SWAP. In Figure 38 we plot the fidelity variation ΔF as a function of θ and φ, considering the depolarizing noise. Here ΔF is less

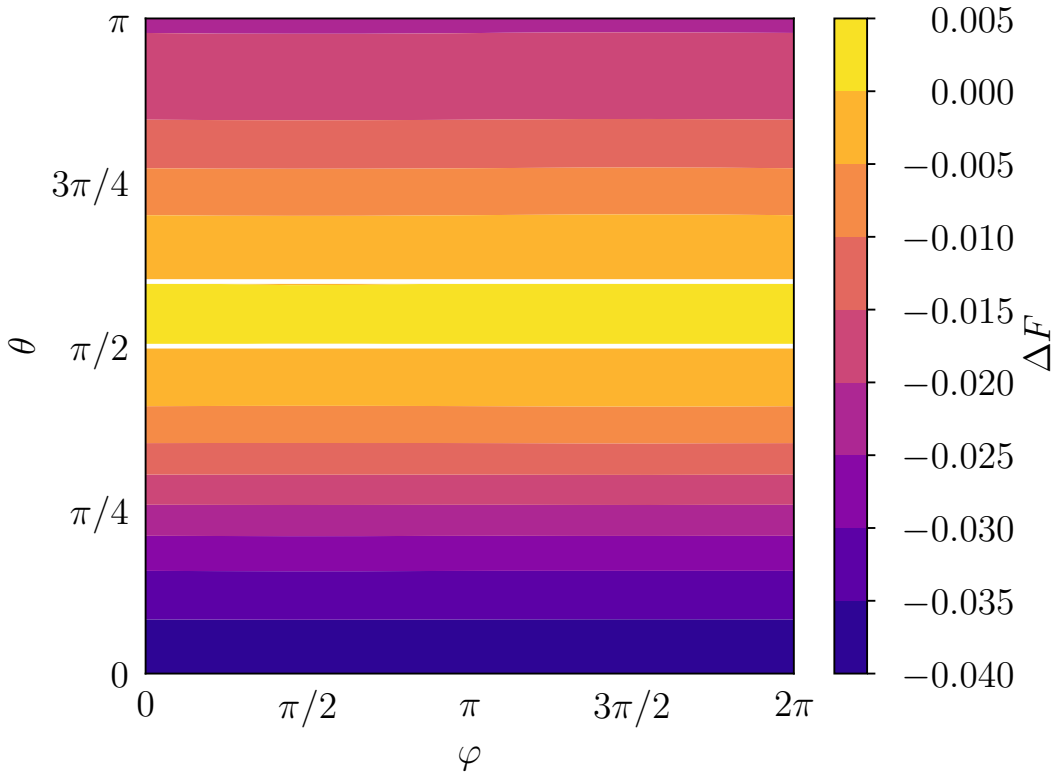

Figure 37 – Fidelity difference considering a CNOT followed by two SWAP gates and vice-versa as a function of θ and φ, which are related to the initial state $|\phi_{in}(\theta,\varphi)\rangle = |+\rangle|q_2(\theta,\varphi)\rangle$ for decay rate $\gamma\tau_0 = 0.1$ and the dephasing error. In this case, four qubits are spatially arranged in a 2D square spin chain. The white line represents the values where $\Delta F = 0$.

or equal to zero for all values of θ and ϕ with a decay rate of $\gamma\tau_0 = 0.1$. For this type of noise, the order 2SWAP-1CNOT always provides a higher fidelity when compared to the order 1CNOT-2SWAP.

4.4 Conclusion

We propose a scheme to connect long distance QD qubits by using a spin chain with nearest-neighbors interaction considering a Heisenberg type Hamiltonian with time dependent pulses. We employ this approach to obtain the SWAP and the CNOT gates, although other gates could be tested. When the system is free from decoherence, we achieve a fidelity of 0.999999 for both type of gates. We also consider the most important types of noise, dephasing and amplitude-damping, by using the master equation approach. Moreover, we propose two different spatial arrangements for the physical qubits, the 1D

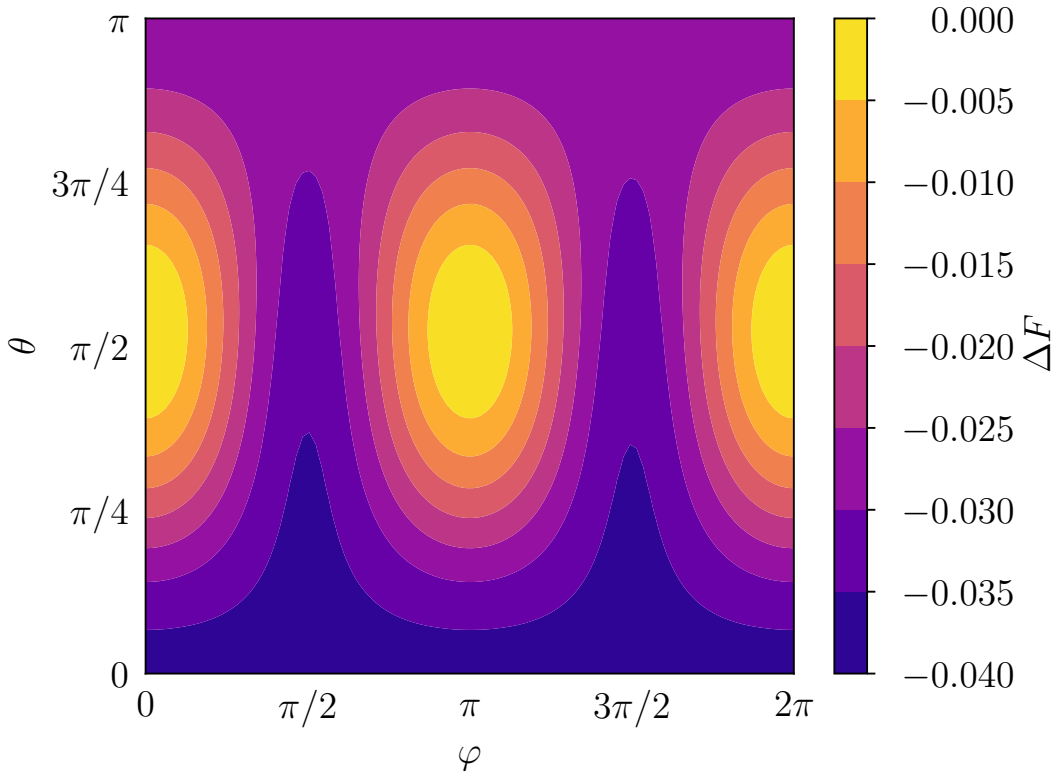

Figure 38 – Fidelity difference considering a CNOT followed by two SWAP gates and vice-versa as a function of θ and φ, which are related to the initial state $|\phi_{in}(\theta,\varphi)\rangle = |+\rangle|q_2(\theta,\varphi)\rangle$ for decay rate $\gamma\tau_0 = 0.1$ for depolarizing error. In this case, four qubits are spatially arrange in a 2D square spin chain.

chain and the 2D square chain. The 2D chain provides a better performance than the 1D chain, because we can apply pairs of gates at the same time. Furthermore, we investigate the role of the order of gates implementation when decoherence is taken into account, thus, we simulate the action of a CNOT gate followed by a sequence of SWAP gates that transport the quantum information and vice-versa. We found that the order of application of these gates is relevant and depends on the initial state of the system. This difference of order of gates can be very large when the system is composed of a large number of qubits, which is the case in a quantum computer.

5 Conclusion

This thesis presents three distinct chapters related to quantum physics, addressing different aspects of quantum computing and quantum systems. In the chapter 2, we propose a theoretical model that explains the reentrant behavior of conductance in quasi-one-dimensional systems, even in the absence of external magnetic fields. We show that this behavior is caused by a resonant reflection, which can occur if two necessary conditions are met: the existence of an attractive potential and the coupling between different scattering channels. Also, we show that the Rashba spin-orbit coupling or the structural deformation in the quasi-one-dimensional systems are sufficient for observing the reentrant feature because these two mechanisms provide the necessary conditions to observe a resonant reflection.

In chapter 3, we propose a protocol using tools of machine learning to determine the parameters of a two qubit QD Hamiltonian. By training a neural network to predict parameters of the Hamiltonian using theoretical values calculated from measurements of observables at different time values, we developed models that can be used to predict the interqubit coupling. This method can significantly reduce the experimental time and provide accurate results for the Hamiltonian parameters of a double quantum dot system. Although a restricted range of values was used, the study developed in this thesis allows to guide future investigations that can explore different parameter configurations. Lastly, this chapter aimed at learning ML techniques and applying them to physical systems. We believe that this tool can be useful in the future for studying physics, such as the case studied in a recent paper (94).

In chapter 4, we propose a scheme for connecting long-distance quantum dot qubits using nearest-neighbor interactions. When dissipative effects are not taken into account, we achieve high-fidelity SWAP and CNOT gates. Moreover, we propose two different spatial arrangements for the physical qubits: the 1D chain and the 2D square chain and we demonstrate that the 2D chain provides a better performance than the 1D chain because

it allows pairs of gates to be applied simultaneously. Moreover, we also investigate the impact of noise on the system's performance, considering the most important types of noise, namely dephasing and amplitude-damping. We demonstrate that the order of the gate implementation is significant when the system is subjected to decoherence, particularly in the case of a large number of qubits. These findings have implications for the development of quantum computers and highlight the importance of considering noise and the order of gate implementation when designing quantum algorithms.

Overall, this thesis contributes to the understanding of quantum systems related to platforms for quantum computing, thus providing a foundation for future research in this field. The findings of all chapters can be applied to the development of quantum technologies, including quantum computing and quantum communication.

Bibliography

1 HEEDT, S. et al. Signatures of interaction-induced helical gaps in nanowire quantum point contacts. *Nature physics*, Nature Publishing Group, v. 13, n. 6, p. 563–567, 2017. Quoted 10 times on 6, 20, 21, 22, 24, 26, 40, 48, 50, and 53 pages.

2 HOLEVO, A. S. Bounds for the quantity of information transmitted by a quantum communication channel. *Problemy Peredachi Informatsii*, Russian Academy of Sciences, Branch of Informatics, Computer Equipment and ..., v. 9, n. 3, p. 3–11, 1973. Quoted on page 17.

3 POPLAVSKIĭ, R. Thermodynamic models of information processes. *Soviet Physics Uspekhi*, IOP Publishing, v. 18, n. 3, p. 222, 1975. Quoted on page 17.

4 FEYNMAN, R. P. Simulating physics with computers. In: *Feynman and computation*. [S.l.]: CRC Press, 2018. p. 133–153. Quoted on page 17.

5 SHOR, P. W. Algorithms for quantum computation: discrete logarithms and factoring. In: IEEE. *Proceedings 35th annual symposium on foundations of computer science*. [S.l.], 1994. p. 124–134. Quoted on page 17.

6 GROVER, L. K. A fast quantum mechanical algorithm for database search. In: *Proceedings of the twenty-eighth annual ACM symposium on Theory of computing*. [S.l.: s.n.], 1996. p. 212–219. Quoted on page 17.

7 WU, Y. et al. Strong quantum computational advantage using a superconducting quantum processor. *Physical review letters*, APS, v. 127, n. 18, p. 180501, 2021. Quoted on page 17.

8 STERN, A.; LINDNER, N. H. Topological quantum computation—from basic concepts to first experiments. *Science*, v. 339, n. 6124, p. 1179–1184, 2013. Disponível em: <https://www.science.org/doi/abs/10.1126/science.1231473>. Quoted on page 18.

9 MAJER, J. et al. Coupling superconducting qubits via a cavity bus. *Nature*, v. 449, n. 7161, p. 443–447, Sep 2007. ISSN 1476-4687. Disponível em: <https://doi.org/10.1038/nature06184>. Quoted on page 18.

10 DEVORET, M. H.; WALLRAFF, A.; MARTINIS, J. M. *Superconducting Qubits: A Short Review*. 2004. Quoted on page 18.

11 BLATT, R.; WINELAND, D. Entangled states of trapped atomic ions. *Nature*, v. 453, n. 7198, p. 1008–1015, Jun 2008. ISSN 1476-4687. Disponível em: <https://doi.org/10.1038/nature07125>. Quoted on page 18.

12 KNILL, E.; LAFLAMME, R.; MILBURN, G. J. A scheme for efficient quantum computation with linear optics. *Nature*, v. 409, n. 6816, p. 46–52, Jan 2001. ISSN 1476-4687. Disponível em: <https://doi.org/10.1038/35051009>. Quoted on page 18.

13 LOSS, D.; DIVINCENZO, D. P. Quantum computation with quantum dots. *Phys. Rev. A*, American Physical Society, v. 57, p. 120–126, Jan 1998. Disponível em:

<https://link.aps.org/doi/10.1103/PhysRevA.57.120>. Quoted 2 times on 18 and 20 pages.

14 JIA, Z. et al. Superconducting and silicon-based semiconductor quantum computers: A review. *IEEE Nanotechnology Magazine*, IEEE, 2022. Quoted on page 18.

15 NIKANDISH, R. et al. Semiconductor quantum computing: Toward a cmos quantum computer on chip. *IEEE Nanotechnology Magazine*, IEEE, v. 15, n. 6, p. 8–20, 2021. Quoted on page 18.

16 VELDHORST, M. et al. A two-qubit logic gate in silicon. *Nature*, Nature Publishing Group UK London, v. 526, n. 7573, p. 410–414, 2015. Quoted on page 18.

17 VELDHORST, M. et al. An addressable quantum dot qubit with fault-tolerant control-fidelity. *Nature nanotechnology*, Nature Publishing Group UK London, v. 9, n. 12, p. 981–985, 2014. Quoted on page 18.

18 HE, M.; SUN, H.; HE, Q. L. Topological insulator: Spintronics and quantum computations. *Frontiers of Physics*, Springer, v. 14, p. 1–16, 2019. Quoted on page 18.

19 QI, X.-L.; ZHANG, S.-C. Topological insulators and superconductors. *Reviews of Modern Physics*, APS, v. 83, n. 4, p. 1057, 2011. Quoted 2 times on 18 and 19 pages.

20 ZHANG, T. et al. Experimental demonstration of topological surface states protected by time-reversal symmetry. *Physical Review Letters*, APS, v. 103, n. 26, p. 266803, 2009. Quoted 2 times on 18 and 19 pages.

21 KIM, S. et al. Robust protection from backscattering in the topological insulator bi 1.5 sb 0.5 te 1.7 se 1.3. *Physical Review Letters*, APS, v. 112, n. 13, p. 136802, 2014. Quoted on page 18.

22 PETTA, J. R. et al. Coherent manipulation of coupled electron spins in semiconductor quantum dots. *Science*, American Association for the Advancement of Science, v. 309, n. 5744, p. 2180–2184, 2005. Quoted on page 18.

23 TANG, J.; WANG, K. L. Electrical spin injection and transport in semiconductor nanowires: challenges, progress and perspectives. *Nanoscale*, Royal Society of Chemistry, v. 7, n. 10, p. 4325–4337, 2015. Quoted on page 18.

24 SCHÄPERS, T. Semiconductor spintronics. In: *Semiconductor Spintronics*. [S.l.]: de Gruyter, 2016. Quoted on page 18.

25 SZE, S. M.; LI, Y.; NG, K. K. *Physics of semiconductor devices*. [S.l.]: John wiley & sons, 2021. Quoted 2 times on 18 and 19 pages.

26 MI, Z.; CHANG, Y.-L. Iii-v compound semiconductor nanostructures on silicon: Epitaxial growth, properties, and applications in light emitting diodes and lasers. *Journal of Nanophotonics*, SPIE, v. 3, n. 1, p. 031602, 2009. Quoted on page 18.

27 MORALES, A. M.; LIEBER, C. M. A laser ablation method for the synthesis of crystalline semiconductor nanowires. *Science*, American Association for the Advancement of Science, v. 279, n. 5348, p. 208–211, 1998. Quoted on page 18.

28 BERNEVIG, B. A. Topological insulators and topological superconductors. In: *Topological Insulators and Topological Superconductors*. [S.l.]: Princeton university press, 2013. Quoted on page 19.

29 SARMA, S. D.; FREEDMAN, M.; NAYAK, C. Majorana zero modes and topological quantum computation. *npj Quantum Information*, Nature Publishing Group, v. 1, n. 1, p. 1–13, 2015. Quoted on page 19.

30 MAJORANA, E. Teoria simmetrica dell'elettrone e del positrone. *Il Nuovo Cimento (1924-1942)*, Springer, v. 14, n. 4, p. 171–184, 1937. Quoted on page 19.

31 BEENAKKER, C. Search for majorana fermions in superconductors. *Annu. Rev. Condens. Matter Phys.*, Annual Reviews, v. 4, n. 1, p. 113–136, 2013. Quoted on page 19.

32 SATO, M.; FUJIMOTO, S. Majorana fermions and topology in superconductors. *Journal of the Physical Society of Japan*, The Physical Society of Japan, v. 85, n. 7, p. 072001, 2016. Quoted on page 19.

33 SATO, M.; ANDO, Y. Topological superconductors: a review. *Reports on Progress in Physics*, IOP Publishing, v. 80, n. 7, p. 076501, 2017. Quoted on page 19.

34 SENTHIL, T.; FISHER, M. P. Quasiparticle localization in superconductors with spin-orbit scattering. *Physical Review B*, APS, v. 61, n. 14, p. 9690, 2000. Quoted on page 19.

35 MOORE, G.; READ, N. Nonabelions in the fractional quantum hall effect. *Nuclear Physics B*, Elsevier, v. 360, n. 2-3, p. 362–396, 1991. Quoted on page 19.

36 IVANOV, D. A. Non-abelian statistics of half-quantum vortices in p-wave superconductors. *Physical review letters*, APS, v. 86, n. 2, p. 268, 2001. Quoted 2 times on 19 and 20 pages.

37 SHTENGEL, K. Non-abelian anyons: New particles for less than a billion? *Physics*, APS, v. 3, p. 93, 2010. Quoted on page 19.

38 VOLOVIK, G. Fermion zero modes on vortices in chiral superconductors. *Journal of Experimental and Theoretical Physics Letters*, Springer, v. 70, p. 609–614, 1999. Quoted on page 20.

39 READ, N.; GREEN, D. Paired states of fermions in two dimensions with breaking of parity and time-reversal symmetries and the fractional quantum hall effect. *Physical Review B*, APS, v. 61, n. 15, p. 10267, 2000. Quoted on page 20.

40 FU, L.; KANE, C. L. Superconducting proximity effect and majorana fermions at the surface of a topological insulator. *Physical review letters*, APS, v. 100, n. 9, p. 096407, 2008. Quoted on page 20.

41 OREG, Y.; REFAEL, G.; OPPEN, F. V. Helical liquids and majorana bound states in quantum wires. *Physical review letters*, APS, v. 105, n. 17, p. 177002, 2010. Quoted on page 20.

42 SAU, J. D. et al. Generic new platform for topological quantum computation using semiconductor heterostructures. *Physical review letters*, APS, v. 104, n. 4, p. 040502, 2010. Quoted on page 20.

43 LUTCHYN, R. M.; SAU, J. D.; SARMA, S. D. Majorana fermions and a topological phase transition in semiconductor-superconductor heterostructures. *Physical review letters*, APS, v. 105, n. 7, p. 077001, 2010. Quoted on page 20.

44 SAU, J. D. et al. Non-abelian quantum order in spin-orbit-coupled semiconductors: Search for topological majorana particles in solid-state systems. *Physical Review B*, APS, v. 82, n. 21, p. 214509, 2010. Quoted on page 20.

45 STANESCU, T. D.; LUTCHYN, R. M.; SARMA, S. D. Majorana fermions in semiconductor nanowires. *Physical Review B*, APS, v. 84, n. 14, p. 144522, 2011. Quoted on page 20.

46 ALICEA, J. et al. Non-abelian statistics and topological quantum information processing in 1d wire networks. *Nature Physics*, Nature Publishing Group, v. 7, n. 5, p. 412–417, 2011. Quoted on page 20.

47 OREG, Y.; REFAEL, G.; OPPEN, F. von. Helical liquids and majorana bound states in quantum wires. *Phys. Rev. Lett.*, American Physical Society, v. 105, p. 177002, Oct 2010. Disponível em: <https://link.aps.org/doi/10.1103/PhysRevLett.105.177002>. Quoted on page 20.

48 LUTCHYN, R. M.; SAU, J. D.; SARMA, S. D. Majorana fermions and a topological phase transition in semiconductor-superconductor heterostructures. *Phys. Rev. Lett.*, American Physical Society, v. 105, p. 077001, Aug 2010. Disponível em: <https://link.aps.org/doi/10.1103/PhysRevLett.105.077001>. Quoted on page 20.

49 KAMMHUBER, J. et al. Conductance through a helical state in an indium antimonide nanowire. *Nature communications*, Nature Publishing Group, v. 8, n. 1, p. 1–6, 2017. Quoted on page 20.

50 WEPEREN, I. van et al. Quantized conductance in an insb nanowire. *Nano letters*, ACS Publications, v. 13, n. 2, p. 387–391, 2013. Quoted on page 20.

51 SUN, J. et al. Helical hole state in multiple conduction modes in ge/si core/shell nanowire. *Nano letters*, ACS Publications, v. 18, n. 10, p. 6144–6149, 2018. Quoted 2 times on 20 and 24 pages.

52 VDOVIN, E. et al. Imaging the electron wave function in self-assembled quantum dots. *Science*, American Association for the Advancement of Science, v. 290, n. 5489, p. 122–124, 2000. Quoted on page 20.

53 BURKARD, G.; LOSS, D.; DIVINCENZO, D. P. Coupled quantum dots as quantum gates. *Phys. Rev. B*, American Physical Society, v. 59, p. 2070–2078, Jan 1999. Disponível em: <https://link.aps.org/doi/10.1103/PhysRevB.59.2070>. Quoted on page 20.

54 ARQUER, F. P. García de et al. Semiconductor quantum dots: Technological progress and future challenges. *Science*, American Association for the Advancement of Science, v. 373, n. 6555, p. eaaz8541, 2021. Quoted on page 20.

55 EZZELL, N. et al. Dynamical decoupling for superconducting qubits: a performance survey. *arXiv preprint arXiv:2207.03670*, 2022. Quoted on page 21.

56 LANGE, G. D. et al. Universal dynamical decoupling of a single solid-state spin from a spin bath. *Science*, American Association for the Advancement of Science, v. 330, n. 6000, p. 60–63, 2010. Quoted on page 21.

57 ROFFE, J. Quantum error correction: an introductory guide. *Contemporary Physics*, Taylor & Francis, v. 60, n. 3, p. 226–245, 2019. Quoted on page 21.

58 HAHN, E. L. Spin echoes. *Phys. Rev.*, American Physical Society, v. 80, p. 580–594, Nov 1950. Disponível em: <https://link.aps.org/doi/10.1103/PhysRev.80.580>. Quoted on page 21.

59 PROSEN, T.; SELIGMAN, T. H. Decoherence of spin echoes. *Journal of Physics A: Mathematical and General*, IOP Publishing, v. 35, n. 22, p. 4707, 2002. Quoted on page 21.

60 TOSI, G. et al. Silicon quantum processor with robust long-distance qubit couplings. *Nature Communications*, v. 8, n. 1, p. 450, Sep 2017. ISSN 2041-1723. Disponível em: <https://doi.org/10.1038/s41467-017-00378-x>. Quoted on page 21.

61 NEWMAN, W. D. et al. Observation of long-range dipole-dipole interactions in hyperbolic metamaterials. *Science advances*, American Association for the Advancement of Science, v. 4, n. 10, p. eaar5278, 2018. Quoted on page 21.

62 LOO, A. F. V. et al. Photon-mediated interactions between distant artificial atoms. *Science*, American Association for the Advancement of Science, v. 342, n. 6165, p. 1494–1496, 2013. Quoted on page 21.

63 ARREGUI, F. J. *Sensors based on nanostructured materials*. [S.l.]: Springer, 2009. v. 10. Quoted on page 21.

64 BHATTACHARYA, P.; MI, Z. Quantum-dot optoelectronic devices. *Proceedings of the IEEE*, IEEE, v. 95, n. 9, p. 1723–1740, 2007. Quoted on page 21.

65 BOZZIO, M. et al. Enhancing quantum cryptography with quantum dot single-photon sources. *npj Quantum Information*, Nature Publishing Group UK London, v. 8, n. 1, p. 104, 2022. Quoted on page 21.

66 SHULMAN, M. D. et al. Demonstration of entanglement of electrostatically coupled singlet-triplet qubits. *science*, American Association for the Advancement of Science, v. 336, n. 6078, p. 202–205, 2012. Quoted 4 times on 23, 54, 61, and 65 pages.

67 STřEDA, P.; ŠEBA, P. Antisymmetric spin filtering in one-dimensional electron systems with uniform spin-orbit coupling. *Phys. Rev. Lett.*, American Physical Society, v. 90, p. 256601, Jun 2003. Disponível em: <https://link.aps.org/doi/10.1103/PhysRevLett.90.256601>. Quoted on page 24.

68 PEDDER, C. J. et al. Dynamic response functions and helical gaps in interacting rashba nanowires with and without magnetic fields. *Phys. Rev. B*, American Physical Society, v. 94, p. 245414, Dec 2016. Disponível em: <https://link.aps.org/doi/10.1103/PhysRevB.94.245414>. Quoted on page 24.

69 KHRAPAI, V. S.; NAGAEV, K. E. Spin-orbit coupling and resonances in the conductance of quantum wires. *Phys. Rev. B*, American Physical Society, v. 98, p. 121401, Sep 2018. Disponível em: <https://link.aps.org/doi/10.1103/PhysRevB.98.121401>. Quoted on page 24.

70 SALDAÑA, J. C. E. et al. Split-channel ballistic transport in an insb nanowire. *Nano Letters*, ACS Publications, v. 18, n. 4, p. 2282–2287, 2018. Quoted on page 24.

71 BARDARSON, J. H. et al. Coherent electronic transport in a multimode quantum channel with gaussian-type scatterers. *Phys. Rev. B*, American Physical Society, v. 70, p. 245308, Dec 2004. Disponível em: <https://link.aps.org/doi/10.1103/PhysRevB.70.245308>. Quoted on page 24.

72 SÁNCHEZ, D.; SERRA, L. m. c. Fano-rashba effect in a quantum wire. *Phys. Rev. B*, American Physical Society, v. 74, p. 153313, Oct 2006. Disponível em: <https://link.aps.org/doi/10.1103/PhysRevB.74.153313>. Quoted 2 times on 24 and 28 pages.

73 GURVITZ, S. A.; LEVINSON, Y. B. Resonant reflection and transmission in a conducting channel with a single impurity. *Phys. Rev. B*, American Physical Society, v. 47, p. 10578–10587, Apr 1993. Disponível em: <https://link.aps.org/doi/10.1103/PhysRevB.47.10578>. Quoted 2 times on 24 and 29 pages.

74 WINKLER, R. *Spin-Orbit Coupling Effects in Two-Dimensional Electron and Hole Systems*. Berlin: Springer Tracts in Modern Physics Springer, 2003. Quoted on page 25.

75 CUNHA, I. et al. Multichannel scattering mechanism behind the reentrant conductance feature in nanowires subject to strong spin-orbit coupling. *Physical Review B*, APS, v. 102, n. 19, p. 195423, 2020. Quoted on page 25.

76 CUNHA, I.; VILLEGAS-LELOVSKY, L.; CASTELANO, L. K. Influence of deformations on the reentrant conductance feature in semiconducting nanowires. *Physics Letters A*, Elsevier, v. 426, p. 127879, 2022. Quoted on page 25.

77 MOROZ, A. V.; BARNES, C. H. W. Effect of the spin-orbit interaction on the band structure and conductance of quasi-one-dimensional systems. *Phys. Rev. B*, American Physical Society, v. 60, p. 14272–14285, Nov 1999. Disponível em: <https://link.aps.org/doi/10.1103/PhysRevB.60.14272>. Quoted on page 26.

78 WINKLER, R. *Spin-orbit coupling effects in two-dimensional electron and hole systems*. [S.l.]: Springer, 2003. v. 191. Quoted on page 27.

79 XIAO, Y.-C.; WANG, R.-X.; YANG, R.-S. Exact solutions of the extended spin field-effect transistor. *Superlattices and Microstructures*, v. 73, p. 322 – 329, 2014. ISSN 0749-6036. Disponível em: <http://www.sciencedirect.com/science/article/pii/S0749603614001943>. Quoted on page 35.

80 RAINIS, D.; LOSS, D. Conductance behavior in nanowires with spin-orbit interaction: A numerical study. *Phys. Rev. B*, American Physical Society, v. 90, p. 235415, Dec 2014. Disponível em: <https://link.aps.org/doi/10.1103/PhysRevB.90.235415>. Quoted 3 times on 35, 37, and 50 pages.

81 GURVITZ, S.; LEVINSON, Y. Resonant reflection and transmission in a conducting channel with a single impurity. *PHYSICAL REVIEW B*, v. 47, n. 16, p. 10578–10587, APR 15 1993. ISSN 0163-1829. Quoted 4 times on 44, 46, 51, and 99 pages.

82 SANCHEZ, D.; SERRA, L. Fano-rashba effect in a quantum wire. *PHYSICAL REVIEW B*, v. 74, n. 15, OCT 2006. ISSN 1098-0121. Quoted 2 times on 47 and 99 pages.

83 KAMMHUBER, J. et al. Conductance through a helical state in an indium antimonide nanowire. *NATURE COMMUNICATIONS*, v. 8, SEP 7 2017. ISSN 2041-1723. Quoted on page 53.

84 SIGILLITO, A. J. et al. Coherent transfer of quantum information in a silicon double quantum dot using resonant swap gates. *npj Quantum Information*, v. 5, n. 1, p. 110, Nov 2019. ISSN 2056-6387. Disponível em: <https://doi.org/10.1038/s41534-019-0225-0>. Quoted on page 66.

85 CASTELANO, L. K. et al. Optimal control of universal quantum gates in a double quantum dot. *Phys. Rev. B*, American Physical Society, v. 97, p. 235301, Jun 2018. Disponível em: <https://link.aps.org/doi/10.1103/PhysRevB.97.235301>. Quoted 2 times on 66 and 70 pages.

86 HANSEN, I. et al. Pulse engineering of a global field for robust and universal quantum computation. *Phys. Rev. A*, American Physical Society, v. 104, p. 062415, Dec 2021. Disponível em: <https://link.aps.org/doi/10.1103/PhysRevA.104.062415>. Quoted on page 66.

87 FOULK, N. L.; THROCKMORTON, R. E.; SARMA, S. D. Dissipation and gate timing errors in swap operations of qubits. *Phys. Rev. B*, American Physical Society, v. 105, p. 155411, Apr 2022. Disponível em: <https://link.aps.org/doi/10.1103/PhysRevB.105.155411>. Quoted on page 66.

88 A., C. I. L. N. M. *Quantum Computation and Quantum Information*. 10th. ed. [S.l.]: Cambridge University Press, 2011. Quoted on page 66.

89 CUNHA, I.; CASTELANO, L. K. Influence of errors on the transport of quantum information through distant quantum dot spin qubits. *Physics Letters A*, Elsevier, v. 454, p. 128499, 2022. Quoted on page 66.

90 MANZANO, D. A short introduction to the lindblad master equation. *Aip Advances*, AIP Publishing LLC, v. 10, n. 2, p. 025106, 2020. Quoted on page 67.

91 PALAO, J. P.; KOSLOFF, R. Optimal control theory for unitary transformations. *Phys. Rev. A*, American Physical Society, v. 68, p. 062308, Dec 2003. Disponível em: <https://link.aps.org/doi/10.1103/PhysRevA.68.062308>. Quoted on page 70.

92 TESCH, C. M.; VIVIE-RIEDLE, R. de. Vibrational molecular quantum computing: Basis set independence and theoretical realization of the deutsch–jozsa algorithm. *The Journal of Chemical Physics*, v. 121, n. 24, p. 12158–12168, 2004. Disponível em: <https://aip.scitation.org/doi/abs/10.1063/1.1818131>. Quoted on page 70.

93 JONES, C. et al. Logical qubit in a linear array of semiconductor quantum dots. *Phys. Rev. X*, American Physical Society, v. 8, p. 021058, Jun 2018. Disponível em: <https://link.aps.org/doi/10.1103/PhysRevX.8.021058>. Quoted on page 74.

94 LINK, M. et al. Machine learning the phase diagram of a strongly interacting fermi gas. *Physical Review Letters*, APS, v. 130, n. 20, p. 203401, 2023. Quoted on page 84.

APPENDIX A – Transport Calculations

A.1 Rashba Coupling

In this section we will determine the matrix elements for Hamiltoninan Rashba SOC with the harmonic oscliator as the confining potential. Therefore, for the initial Hamiltonian

$$H = \left(\frac{\boldsymbol{p}^2}{2m^*} + V_c(x,y) + V(x,y,z)\right)\mathbf{I} + H^{SO} \tag{A.1}$$

where

$$V_c(x,y) = \frac{m^*\omega_x^2 x^2}{2} + \frac{m^*\omega_y^2 y^2}{2} \tag{A.2a}$$

$$V(x,y,z) = \frac{m^*(\omega(z)^2 - \omega_x^2}{2}\left(x^2+y^2\right) \tag{A.2b}$$

we have

$$H = \left(\frac{\boldsymbol{p}^2}{2m^*} + \frac{m^*\omega_x^2 x^2}{2} + \frac{m^*\omega_y^2 y^2}{2}\right)\mathbf{I} + H^{SOC} \tag{A.3}$$

By implement the Rashba SOC as

$$H^{SOC} = \alpha(z)\frac{p_y}{\hbar}\sigma_z - \{\alpha(z), \frac{p_z}{\hbar}\}\sigma_y \tag{A.4}$$

the matrix elements can be expressed as

$$\begin{aligned}[H^{n,m}_{n',m'}]^{SO} &= \langle n,m|\alpha(z)\frac{p_y}{\hbar}\sigma_z - \{\alpha(z), \frac{p_z}{\hbar}\}\sigma_y|n',m'\rangle \\ &= \langle n,m|\alpha(z)\frac{p_y}{\hbar}\sigma_z|n',m'\rangle - \langle n,m|\{\alpha(z), \frac{p_z}{\hbar}\}\sigma_y|n',m'\rangle\end{aligned} \tag{A.5}$$

or simply

$$[H^{n,m}_{n',m'}]^{SO} = A^{n,m}_{n',m'} + B^{n,m}_{n',m'} \tag{A.6}$$

For the first element,

$$A^{n,m}_{n',m'} = \frac{\alpha(z)}{\hbar}\langle n,m|\ p_y\sigma_z\ |n',m'\rangle \tag{A.7}$$

we use the momentum representation

$$p_q = \frac{\sqrt{2m^*\hbar\omega_q}}{2i}\left(a_q - a_q^\dagger\right) \tag{A.8}$$

therefore,

$$A^{n,m}_{n',m'} = \alpha(z)\frac{\sqrt{2m^*\hbar\omega_y}}{2i\hbar}\langle n,m|\ \left(a_y - a_y^\dagger\right)\sigma_z\ |n',m'\rangle \tag{A.9}$$

$$A^{n,m}_{n',m'} = \alpha(z)\frac{\sqrt{2m^*\hbar\omega_y}}{2i\hbar}\left[\sqrt{m'}\delta_{m,m'-1} - \sqrt{m'+1}\delta_{m,m'+1}\right]\sigma_z\delta_{n,n'} \tag{A.10}$$

The second element,

$$B^{n,m}_{n',m'} = -\langle n,m|\{\alpha(z),\frac{p_z}{\hbar}\}\sigma_y|n',m'\rangle \tag{A.11}$$

can be simplified using the wave vector $k_q = p_q/\hbar$, and therefore

$$B^{n,m}_{n',m'} = -\alpha(z)k_z\sigma_y\delta_{n,n'}\delta_{m,m'}. \tag{A.12}$$

Finally, we can use the canonical basis for each Pauli matrices,

$$\sigma_x = \delta_{s,-s'} \tag{A.13a}$$

$$\sigma_y = is'\delta_{s,-s'} \tag{A.13b}$$

$$\sigma_z = s'\delta_{s,s'} \tag{A.13c}$$

to reach

$$a^{n,m}_{n',m'} = A^{n,m}_{n',m'}/\hbar\omega_x = \frac{\tilde{\alpha}(z)}{2i}\sqrt{\frac{2\omega_y}{\omega_x}}\left[\sqrt{m'}\delta_{m,m'-1} - \sqrt{m'+1}\delta_{m,m'+1}\right]\sigma_z\delta_{n,n'}, \tag{A.14}$$

and

$$b^{n,m}_{n',m'} = B^{n,m}_{n',m'}/\hbar\omega_x = -\tilde{\alpha}(z)\tilde{k}_z\sigma_y\delta_{n,n'}\delta_{m,m'}, \tag{A.15}$$

for

$$\tilde{\alpha}(z) = \frac{\alpha(z)}{\hbar\omega_0 r_0} \tag{A.16}$$

where, $r_0 = \sqrt{\hbar/m^*\omega_0}$ and $\tilde{k}_z = r_x k_z$.

A.2 Boundary Conditions with SOC

In this section, we will determine the boundary conditions when Rashba SOC is taken into account in a finite region of the NW. First of all, lets define position-dependent coefficient α as follows:

$$\alpha(z) = \alpha_0 F(z,L) \tag{A.17}$$

where $F(z,L) = (\Theta(z+L) - \Theta(z-L))$ and $\Theta(z)$ is the Heaviside function. The symmetrized Hamiltonian for the z-direction can be written as

$$H = \mathbf{I}\frac{p_z^2}{2m} + \frac{\sigma_z}{2}(\alpha(z)p_z + p_z\alpha(z)) \tag{A.18}$$

Re-write in the effective unit, we have

$$\bar{H} = -\mathbf{I}\frac{d^2}{d\bar{z}^2} - i\bar{\alpha}_0\sigma_z\left(F(\bar{z},\bar{L})\frac{d}{d\bar{z}} + \frac{d}{d\bar{z}}F(\bar{z},\bar{L})\right) \tag{A.19}$$

The boundary conditions for the wave-function is simply given by the continuity of the wave-function at interfaces:

$$\Psi_I(-\bar{L}) = \Psi_{II}(-\bar{L}) \tag{A.20a}$$

$$\Psi_{III}(\bar{L}) = \Psi_{II}(\bar{L}) \tag{A.20b}$$

To determine the boundary conditions for the derivative of the wave-function, we must do the following procedure

$$\lim_{\epsilon\to 0}\int_{-\bar{L}-\varepsilon}^{-\bar{L}+\varepsilon}\left[\bar{H} - \bar{E}\right]\Psi(\bar{z})d\bar{z} = 0 \tag{A.21a}$$

$$\lim_{\epsilon\to 0}\int_{\bar{L}-\varepsilon}^{\bar{L}+\varepsilon}\left[\bar{H} - \bar{E}\right]\Psi(\bar{z})d\bar{z} = 0 \tag{A.21b}$$

which gives

$$\lim_{\epsilon\to 0}\int_{-\bar{L}-\varepsilon}^{-\bar{L}+\varepsilon}\left[-\mathbf{I}\frac{d^2}{d\bar{z}^2} - i\bar{\alpha}_0\sigma_z\left(F(\bar{z},\bar{L})\frac{d}{d\bar{z}} + \frac{d}{d\bar{z}}F(\bar{z},\bar{L})\right) - \bar{E}\right]\Psi(\bar{z})d\bar{z} = 0 \tag{A.22a}$$

$$\lim_{\epsilon\to 0}\int_{\bar{L}-\varepsilon}^{\bar{L}+\varepsilon}\left[-\mathbf{I}\frac{d^2}{d\bar{z}^2} - i\bar{\alpha}_0\sigma_z\left(F(\bar{z},\bar{L})\frac{d}{d\bar{z}} + \frac{d}{d\bar{z}}F(\bar{z},\bar{L})\right) - \bar{E}\right]\Psi(\bar{z})d\bar{z} = 0 \tag{A.22b}$$

The integrals that must be performed can be divided into two integrals, as follows

$$I_1 = \int \frac{d^2}{d\bar{z}^2}\Psi(\bar{z})d\bar{z} \tag{A.23a}$$

$$I_2 = \int F(\bar{z},\bar{L})\frac{d}{d\bar{z}}\Psi(\bar{z}) + \frac{d}{d\bar{z}}\left(F(\bar{z},\bar{L})\Psi(\bar{z})\right)d\bar{z} \tag{A.23b}$$

These integrals are evaluated straightforward

$$I_1 = \frac{d\Psi(\bar{z})}{d\bar{z}} \tag{A.24a}$$

$$I_2 = 2F(\bar{z},\bar{L})\Psi(\bar{z}) - \int \frac{dF(\bar{z},\bar{L})}{d\bar{z}}\Psi(\bar{z})d\bar{z} \tag{A.24b}$$

Using the derivative of $F(\bar{z}, \bar{L})$,

$$\frac{dF(\bar{z}, \bar{L})}{d\bar{z}} = \delta(\bar{z} + \bar{L}) - \delta(\bar{z} - \bar{L}) \tag{A.25}$$

where $\delta(z)$ is the Dirac delta function; we can substitute the results of Equation A.24 into Equation A.22 achieving

$$\lim_{\epsilon \to 0} \left[-\mathbf{I} \frac{d\Psi(\bar{z})}{d\bar{z}} \Big|_{-\bar{L}-\varepsilon}^{-\bar{L}+\varepsilon} - 2i\bar{\alpha}_0 \sigma_z F(\bar{z}, \bar{L}) \Psi(\bar{z}) \Big|_{-\bar{L}-\varepsilon}^{-\bar{L}+\varepsilon} - i\bar{\alpha}_0 \sigma_z \int_{-\bar{L}-\varepsilon}^{-\bar{L}+\varepsilon} \frac{dF(\bar{z}, \bar{L})}{d\bar{z}} \Psi(\bar{z}) d\bar{z} \right] = 0 \tag{A.26a}$$

$$\lim_{\epsilon \to 0} \left[-\mathbf{I} \frac{d\Psi(\bar{z})}{d\bar{z}} \Big|_{\bar{L}-\varepsilon}^{\bar{L}+\varepsilon} - 2i\bar{\alpha}_0 \sigma_z F(\bar{z}, \bar{L}) \Psi(\bar{z}) \Big|_{\bar{L}-\varepsilon}^{\bar{L}+\varepsilon} - i\bar{\alpha}_0 \sigma_z \int_{\bar{L}-\varepsilon}^{\bar{L}+\varepsilon} \frac{dF(\bar{z}, \bar{L})}{d\bar{z}} \Psi(\bar{z}) d\bar{z} \right] = 0 \tag{A.26b}$$

Finally, by taking the limit of $\varepsilon \to 0$, we reach the difference of the derivatives as

$$-\mathbf{I} \left(\frac{d\Psi_{II}(\bar{z})}{d\bar{z}} \Big|_{-\bar{L}} - \frac{d\Psi_{I}(\bar{z})}{d\bar{z}} \Big|_{-\bar{L}} \right) - i\bar{\alpha}_0 \sigma_z \Psi_{II}(\bar{z}) \Big|_{-\bar{L}} = 0 \tag{A.27a}$$

$$-\mathbf{I} \left(\frac{d\Psi_{III}(\bar{z})}{d\bar{z}} \Big|_{\bar{L}} - \frac{d\Psi_{II}(\bar{z})}{d\bar{z}} \Big|_{\bar{L}} \right) + i\bar{\alpha}_0 \sigma_z \Psi_{II}(\bar{z}) \Big|_{\bar{L}} = 0 \tag{A.27b}$$

APPENDIX B – Further exploration on structural deformation

To further explore our method, we consider some extra cases to understand the dependence of the dips in the conductance as a function of different parameters. First, we vary the length of the region II within the range $L \in [0.2, 9.4]r_0$ with step $\Delta L = 0.2r_0$, assuming $\alpha/\alpha_0 = 0.4$, $E_Z = 0.2\varepsilon_0$, and the cone-shape deformation with $\Delta r_0/r_0 = 0.04$, whose results for the conductance are shown in Figure 39. As already discussed, the

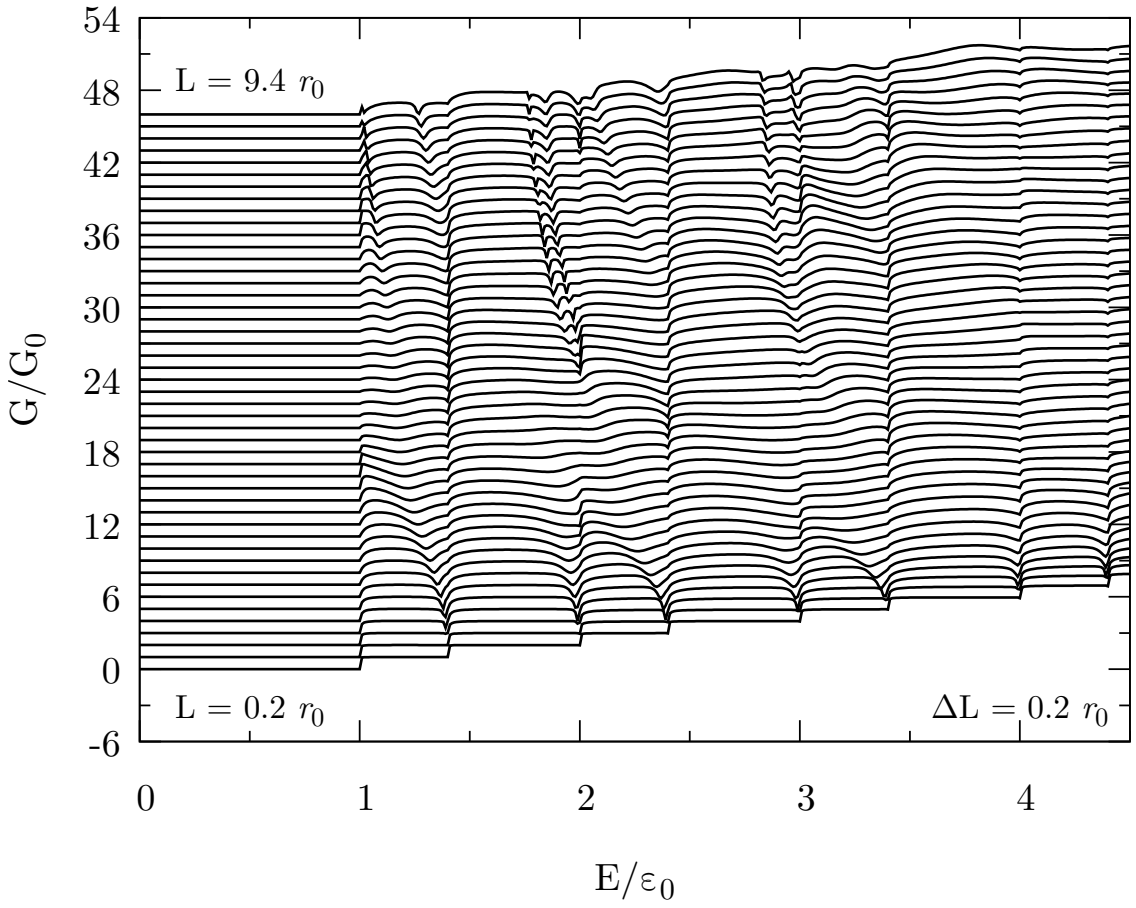

Figure 39 – Normalized conductance as a function of the normalized Fermi energy for different length $L = 0.2r_0$ to $9.4r_0$ with step $\Delta L = 0.2r_0$, considering $\Delta r_1(z)$ for the radius variation function with $\Delta r_0 = 0.04r_0$, the Rashba constant $\alpha = 0.4\alpha_0$, and Zeeman energy $E_Z/\varepsilon_0 = 0.2$. The curves are offset for clarity.

Rashba SOC works as an attractive potential (82), specifically as a quantum well with depth $V_0 = -m\alpha^2/\hbar^2$ and length L. When $L \leq 0.6r_0$ and $\alpha = 0.4\alpha_0$ there is no dip in the conductance because there is no quasibound state within this quantum well. According to the approximate two-channel model described in Ref. (81), the dip in the conductance occurs when an attractive potential induces the formation of a quasi-bound state.

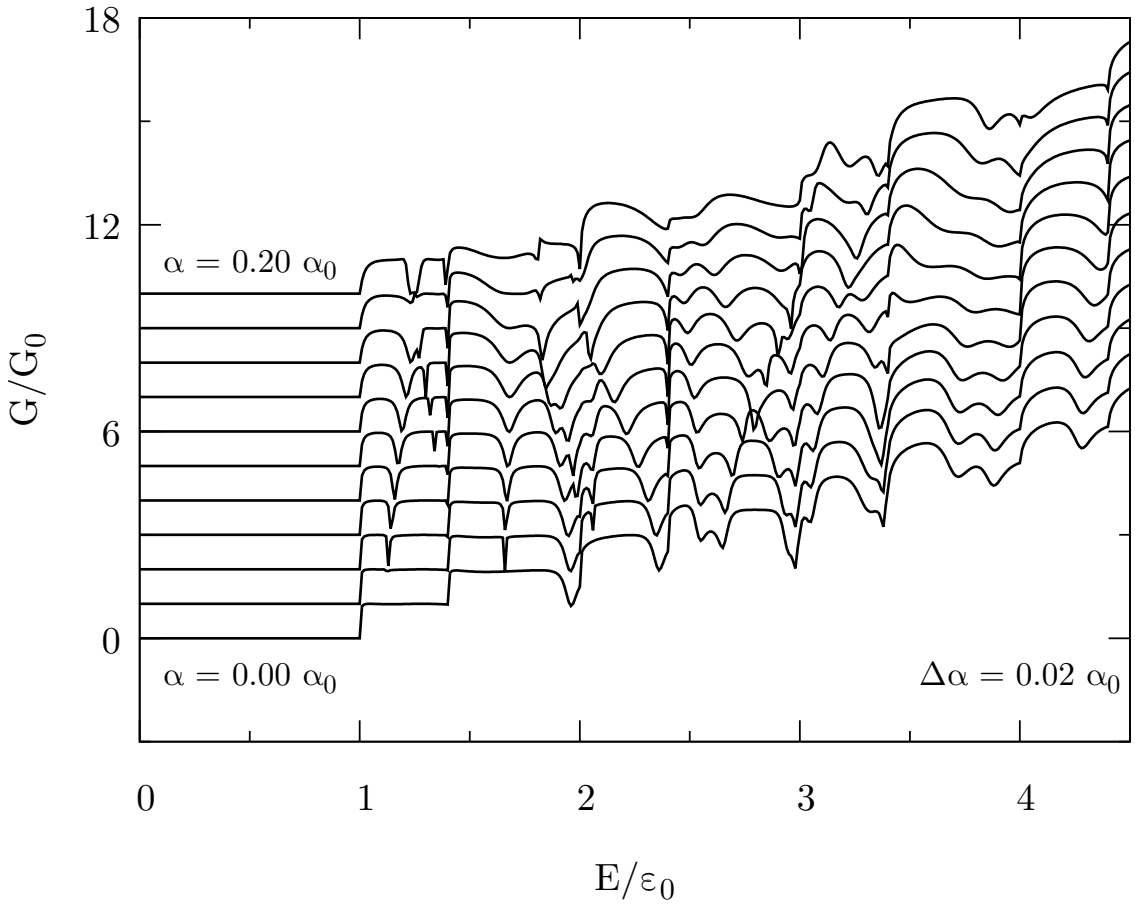

Figure 40 – Normalized conductance as a function of the normalized Fermi energy for different Rashba constant $\alpha/\alpha_0 = 0.0$ to 0.2 with step $\Delta\alpha = 0.02$, considering $\Delta r_1(z)$ for the radius variation function with $\Delta r_0/r_0 = 0.3$, length $L/r_0 = 8.0$, and Zeeman energy $E_Z/\varepsilon_0 = 0.2$. The curves are offset for clarity.

In Figure 39 there is only one dip in the plateaus for $0.6r_0 < L \lessapprox 4.8r_0$, which shifts towards smaller energies in a quadratic way as a function of the length L, which is qualitatively in accordance to the behavior of eigenenergies in a quantum well that represent the position of the quasibound states. For $L > 4.8r_0$, we start to observe two dips within the same plateau, which indicates the presence of two quasibound states within

the same range of energy where the plateau takes place.

In order to deeper explore effects of the Rashba SOC, we vary $\alpha = 0.0 \rightarrow 0.2\alpha_0$ with step $\Delta\alpha = 0.02\alpha_0$ assuming $L > 8r_0$, $E_Z = 0.2\varepsilon_0$, and the cone-shape deformation with $\Delta r_0/r_0 = 0.3$. Such results are plotted in Figure 40, which shows that there is no dip in the first plateau for $\alpha \leq 0.02\alpha_0$. Yet, dips appear for $\alpha > 0.02\alpha_0$ resulting only from the Rashba SOC. Within others plateaus, dips coming from the radius expansion already appear for $\alpha = 0$ and these dips interfere with dips descendant from Rashba SOC.

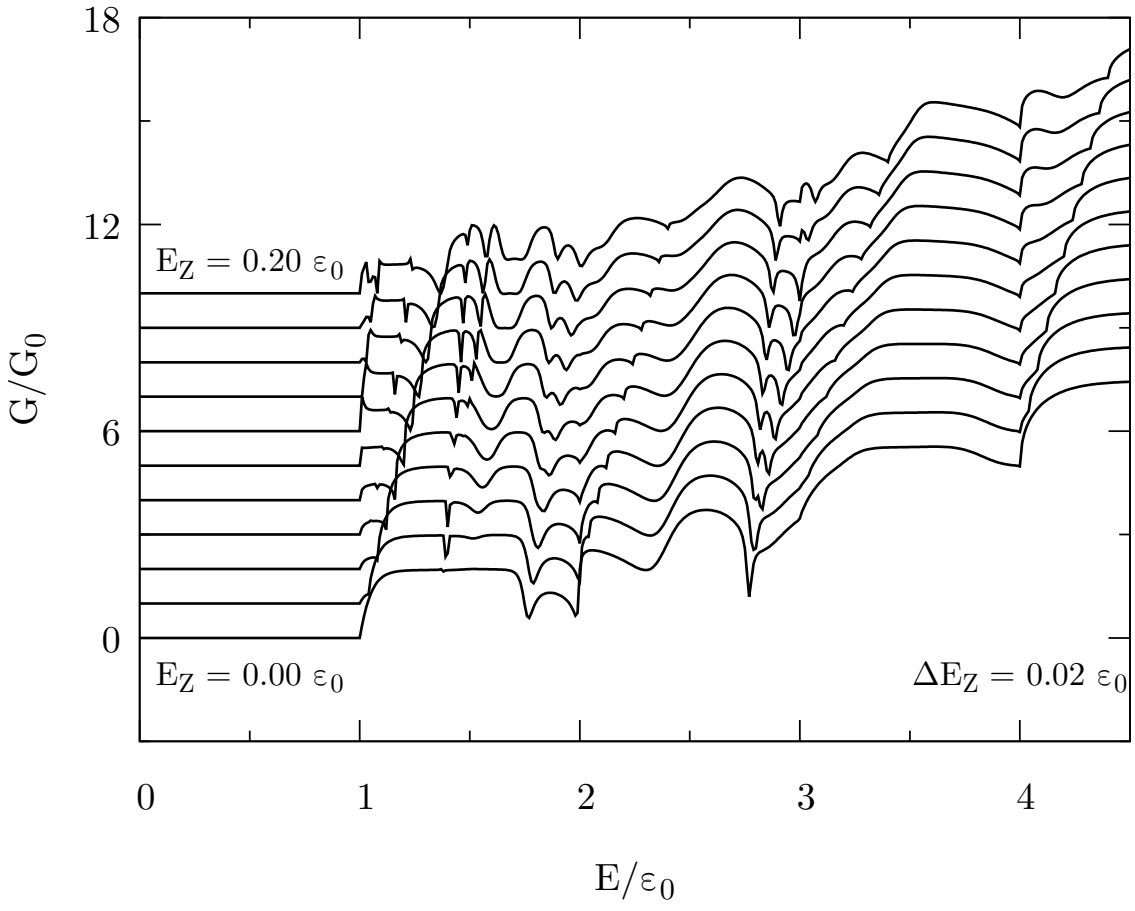

Figure 41 – Normalized conductance as a function of the normalized Fermi energy for different Zeeman energy $E_Z/\varepsilon_0 = 0.0$ to 0.2 with step $\Delta E_Z/\varepsilon_0 = 0.02$, considering $\Delta r_2(z)$ for the radius variation function with $\Delta r_0/r_0 = 0.3$, the Rashba constant $\alpha/\alpha_0 = 0.2$, and length $L/r_0 = 8.0$. The curves are offset for clarity.

Finally, we probe the conductance for different magnetic fields, considering $L > 8r_0$, $E_Z = 0 \rightarrow 0.2\varepsilon_0$ with step $\Delta E_z = 0.02\varepsilon_0$, the square-shape deformation with $\Delta r_0/r_0 = 0.3$,

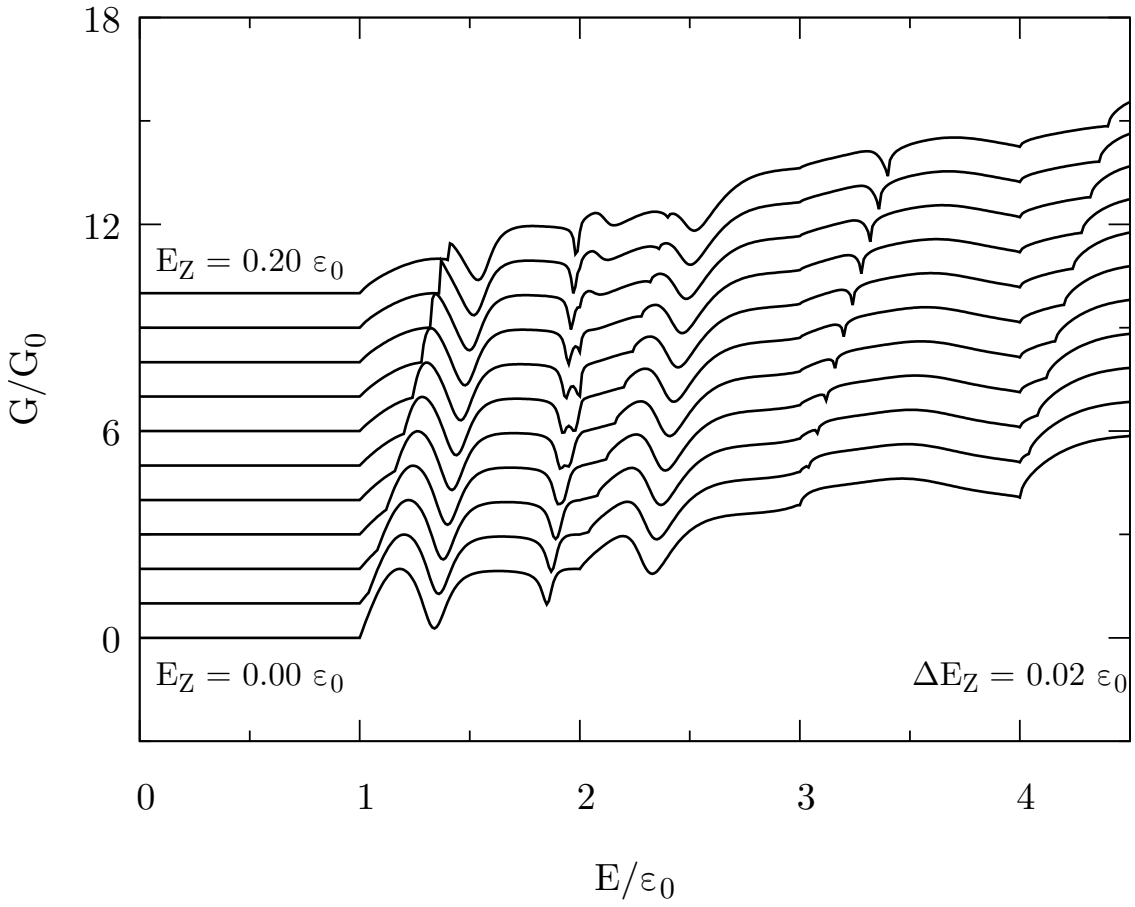

Figure 42 – Normalized conductance as a function of the normalized Fermi energy for different Zeeman energy $E_Z/\varepsilon_0 = 0.0$ to 0.2 with step $\Delta E_Z/\varepsilon_0 = 0.02$, considering $\Delta r_2(z)$ for the radius variation function with $\Delta r_0/r_0 = 0.3$, the Rashba constant $\alpha/\alpha_0 = 0.8$, and length $L/r_0 = 8.0$. The curves are offset for clarity.

and for two different values of Rashba constant $\alpha = 0.2\alpha_0$ and $\alpha = 0.8\alpha_0$. When the Rashba SOC energy $E_R = m^*\alpha^2/2\hbar^2$ is smaller than the Zeeman energy, the conductance is more affected by the magnetic field and more dips appear when E_Z is increased, as shown in Figure 41. On the other hand, Figure 42 shows that dips are not very affected by the magnetic field because in this case the Rashba SOC dominates over the external magnetic field.